

VRIJE  
UNIVERSITEIT  
BRUSSEL

<sup>1</sup> **A search for flavour changing neutral currents  
2 involving a top quark and a Z boson, using the  
3 data collected by the CMS collaboration at a  
4 centre-of-mass energy of 13 TeV**

<sup>5</sup> Isis Van Parijs

<sup>6</sup> Proefschrift ingediend met het oog op het behalen van de academische graad  
<sup>7</sup> Doctor in de Wetenschappen.

Published in Faculteit Wetenschappen & Bio-ingenieurswetenschappen  
Vrije Universiteit Brussel  
At 10 November 2017.

<sup>8</sup>

Responsible Contact: Isis Van Parijs  
Intitute for High Energy Physics  
Promotor: Prof. Jorgen D'Hondt

9      First Referee:                            Prof. Dr. J. D'Hondt  
            Date of Hand-in:                        10 November 2017  
            Date of Defense:                        10 December 2017

# Contents

---

11	<b>1 Theoretical basis</b>	1
12	1.1 Elementary particles and forces . . . . .	1
13	1.2 Standard Model Lagrangian, connecting fields with particles . . . . .	2
14	1.3 Flavours in the SM . . . . .	5
15	1.4 The top quark in the SM . . . . .	6
16	1.5 Effective field theories . . . . .	10
17	1.6 Motivation for new physics . . . . .	14
18	1.7 An effective approach beyond the SM: FCNC involving a top quark . . . . .	15
19	1.8 Experimental constraints on top-FCNC . . . . .	18
20	<b>2 Experimental set-up</b>	23
21	2.1 The Large Hadron Collider . . . . .	23
22	2.2 The Compact Muon Solenoid . . . . .	27
23	2.2.1 CMS coordinate system . . . . .	27
24	2.2.2 Towards the heart of CMS . . . . .	28
25	2.2.3 Data acquisition . . . . .	37
26	2.2.4 Phase 1 upgrades . . . . .	37
27	2.2.5 CMS computing model . . . . .	39
28	<b>3 Analysis techniques</b>	41
29	3.1 Hadron collisions at high energies . . . . .	41
30	3.2 Event generation . . . . .	44
31	3.2.1 Fundamentals of simulating a proton collision . . . . .	44
32	3.2.2 Programs for event generation . . . . .	44
33	3.2.3 Generating FCNC top-Z interactions . . . . .	46
34	3.2.4 Generating SM background events . . . . .	48
35	3.3 Multivariate analysis techniques: Boosted Decision Trees . . . . .	50
36	3.4 Statistical methodology . . . . .	52
37	<b>4 Event reconstruction and identification</b>	55
38	4.1 Object Reconstruction . . . . .	55
39	4.1.1 Charged particle tracks . . . . .	57
40	4.1.2 Following the Muon's Footsteps . . . . .	57
41	4.1.3 The path of the Electron . . . . .	57

42	4.1.4 Primary Vertex Reconstruction . . . . .	58
43	4.1.5 Calorimeter clusters . . . . .	58
44	4.2 Particle flow identification . . . . .	59
45	4.3 Pileup mitigation and luminosity measurement . . . . .	59
46	4.4 Physics object reconstruction and identification . . . . .	60
47	4.4.1 Muons . . . . .	60
48	4.4.2 Electrons . . . . .	62
49	4.4.3 Jets . . . . .	63
50	4.4.4 Jets from b fragmentation . . . . .	66
51	4.4.5 Missing transverse energy . . . . .	69
52	4.5 Summary of corrections . . . . .	69
53	<b>5 Event selection and categorisation</b>	<b>71</b>
54	5.1 Baseline event selection and filters . . . . .	71
55	5.1.1 Event cleaning . . . . .	74
56	5.1.2 Estimation of the trigger efficiency . . . . .	76
57	5.1.3 Corrections . . . . .	77
58	5.2 Analysis Strategy . . . . .	82
59	5.3 Data driven NPL background simulation . . . . .	82
60	5.4 Regions and channels . . . . .	83
61	5.4.1 WZ control region . . . . .	85
62	5.4.2 TTCR and STCR . . . . .	86
63	5.4.3 TTSR and STSR . . . . .	87
64	<b>6 The search for FCNC involving a top quark and a Z boson</b>	<b>89</b>
65	6.1 Construction of template distributions . . . . .	89
66	6.2 Systematic uncertainties . . . . .	89
67	6.3 Limit setting procedure . . . . .	89
68	6.4 Result and discussion . . . . .	89
69	<b>7 Denouement of the top-Z FCNC hunt at 13 TeV</b>	<b>91</b>
70	<b>Appendices</b>	<b>91</b>
71	<b>A Trigger scale factors</b>	<b>93</b>
72	<b>B Dilepton controlplots</b>	<b>105</b>
73	<b>C Statistical independent regions</b>	<b>107</b>
74	<b>Bibliography</b>	<b>109</b>

# Theoretical basis

# 1

---

76 The Standard Model (SM) [1] is a name given in the 1970s to a theory describing the fun-  
 77 damental particles and their interactions. This quantum field theory describes the particles  
 78 and their interactions as fields and has successfully incorporated three of the four fundamental  
 79 forces in the universe. In [Section 1.1](#), the particle content of the SM is summarised, while  
 80 [Section 1.2](#) describes the SM Lagrangian and its symmetries. In [Section 1.3](#), the flavour content  
 81 of the SM is highlighted, and [Section 1.4](#) focusses on the top quark in the SM.

82 The successful theory of the SM has some shortcomings which are discussed in [Section 1.6](#)  
 83 and lead to searches for a more general theory. One of such is using an effective field theory  
 84 (EFT) approach [2] to search for new physics in a model independent way. In [Section 1.7](#) an  
 85 EFT model focussing on flavour changing neutral currents (FCNC) involving a top quark is  
 86 presented. Its current experimental constraints are given in [Section 1.8](#).

## 87 1.1 Elementary particles and forces

88 The interactions in nature can be described by four forces, the strong force, the electromagnetic  
 89 (EM) force, the weak force and the gravitational force. These interactions happen via particles  
 90 with an integer spin known as bosons. The strong interaction is mediated by eight gluons  $g$ ,  
 91 while the electromagnetic force is mediated by photons  $\gamma$ , and the weak force by  $Z$  and  $W^\pm$   
 92 bosons. In [Table 1.1](#), the forces and their characteristics are shown. The gravitational force is  
 93 the only force not included in the SM and can be neglected for energies lower than the Planck  
 scale ( $1.22 \times 10^{19}$  GeV).

**Table 1.1:** The four forces of nature and their characteristics.

	Range	Mediator
Strong force	$10^{-15}$ m	8 gluons
Electromagnetic force	$\infty$	photon
Weak force	$10^{-18}$ m	$W^\pm$ , Zbosons
Gravitational force	$\infty$	unknown

The fermions are the particles that make up the visible matter in the universe. They carry half integer spin and can be subdivided into leptons and quarks, where leptons do not interact strongly. Each fermion has a corresponding anti-fermion which has the same mass and is oppositely charged. The electron  $e$  is the first elementary particle discovered [3] and belongs to the first generation of leptons together with the electron neutrino  $\nu_e$ . The second generation comprises the muon  $\mu$  and muon neutrino  $\nu_\mu$ , whereas the third generation consists of the tau  $\tau$  and tau neutrino  $\nu_\tau$ . The neutrinos are neutral particles, while the other leptons have charge  $\pm q_e$  with  $q_e$  representing the elementary charge of  $1.602 \times 10^{-19}$  C. The masses of charged leptons differ by four orders of magnitude between the first and third generations. In the SM the neutrinos are assumed to be massless, nonetheless it is experimentally established that neutrinos do have a tiny non-zero mass [4, 5]. In Table 1.2, the leptons and their properties in the SM are summarised.

**Table 1.2:** The properties of the leptons in the three generations of the SM [6], where  $q_e$  represents the elementary charge.

Generation	Particle	Mass	Charge
First	$e^-$	0.511 MeV	$-q_e$
	$\nu_e$	$\approx 0$	0
Second	$\mu^-$	106 MeV	$-q_e$
	$\nu_\mu$	$\approx 0$	0
Third	$\tau^-$	1 777 MeV	$-q_e$
	$\nu_\tau$	$\approx 0$	0

106

The quarks can also be divided into three generations. Unlike the leptons, they carry colour charge and can interact via the strong interaction. The top quark, discovered in 1995 at the Tevatron [7, 8], is the heaviest SM particle with a mass<sup>1</sup> measured to be  $173.34 \pm 0.27(\text{stat}) \pm 0.71(\text{syst})$  GeV [9]. The quarks and their properties are summarised in Table 1.3. In nature, only colour neutral objects can exist. This has as consequence that quarks are bound through gluons into mesons (quark+anti-quark) and baryons (three quarks). These mesons and baryons are mostly short-lived and unstable particles that rapidly decay through  $W^\pm$  and  $Z$  bosons. The only known stable baryon is the proton, made up of two up quarks and one down quark.

The scalar boson, commonly known as the Higgs boson, is the last piece of the SM discovered in 2012 [10, 11]. It is responsible for the masses of the  $W^\pm$  and Z boson, and that of the fermions.

## 118 1.2 Standard Model Lagrangian, connecting fields with particles

The SM is a quantum field theory and thus describes the dynamics and kinematics of particles and forces by a Lagrangian  $\mathcal{L}$ . The theory is based on the  $SU(3)_C \times SU(2)_L \times U(1)_Y$  gauge symmetry, where  $SU(2)_L \times U(1)_Y$  describes the electroweak interaction and  $SU(3)_C$  the strong

---

<sup>1</sup>In this thesis all masses and energies are expressed in natural units, where the speed of light and  $\hbar$  are taken to be equal to one.

**Table 1.3:** The properties of the quarks in the three generations of the SM [6], where  $q_e$  represents the elementary charge.

	Generation	Particle	Mass	Charge
First	up u	$2.2^{+0.6}_{-0.4}$ MeV	$\frac{2}{3} q_e$	
	down d	$4.7^{+0.5}_{-0.4}$ MeV	$\frac{-1}{3} q_e$	
Second	charm c	$1.28 \pm 0.03$ GeV	$\frac{2}{3} q_e$	
	strange s	$96^{+8}_{-4}$ MeV	$\frac{-1}{3} q_e$	
Third	top t	$173.1 \pm 0.6$ GeV	$\frac{2}{3} q_e$	
	bottom b	$4.18^{+0.04}_{-0.03}$ GeV	$\frac{-1}{3} q_e$	

interaction. The indices refer to colour C, the left chiral nature of the  $SU(2)_L$  coupling L, and the weak hypercharge Y. Its Lagrangian is constructed such that contains symmetries representing physics conservation laws such as conservation of energy, momentum and angular momentum. The symmetries under local gauge transformations are sustained by demanding gauge invariance<sup>2</sup>.

The  $U(1)_Y$  group has one generator Y with an associated gauge field  $B_\mu$ . The three gauge fields  $W_\mu^1$ ,  $W_\mu^2$ , and  $W_\mu^3$ , are associated to  $SU(2)_L$  with three generators that can be written as half of the Pauli matrices:

$$T_1 = \frac{1}{2} \begin{pmatrix} 0 & 1 \\ 1 & 0 \end{pmatrix}, \quad T_2 = \frac{1}{2} \begin{pmatrix} 0 & -i \\ i & 0 \end{pmatrix}, \quad \text{and} \quad T_3 = \frac{1}{2} \begin{pmatrix} 1 & 0 \\ 0 & -1 \end{pmatrix}. \quad (1.1)$$

The generators  $T^a$  satisfy the Lie algebra:

$$[T_a, T_b] = i\epsilon_{abc} T^c \text{ and } [T_a, Y] = 0, \quad (1.2)$$

where  $\epsilon_{abc}$  is an antisymmetric tensor. The gauge fields of  $SU(2)_L$  only couple to left-handed fermions as required by the observed parity violating nature of the weak force. The  $SU(3)_C$  group represents quantum chromodynamics (QCD). It has eight generators corresponding to eight gluon fields  $G_\mu^{1\dots 8}$ . Unlike  $SU(2)_L \times U(1)_Y$ ,  $SU(3)_C$  is not chiral.

Under  $SU(3)_C$  quarks are colour triplets while leptons are colour singlets. This implies that the quarks carry a colour index ranging between one and three, whereas leptons do not take part in strong interactions. Based on the chirality, the quarks and leptons are organized in doublets or singlets. Each generation  $i$  of fermions consists of left-handed doublets and right-handed singlets:

$$l_{L,i} = \begin{pmatrix} e_{L,i} \\ \nu_{L,i} \end{pmatrix}, \quad e_{R,i}, \quad q_{L,i} = \begin{pmatrix} u_{L,i} \\ d_{L,i} \end{pmatrix}, \quad u_{R,i}, \quad \text{and} \quad d_{R,i} \quad (1.3)$$

The SM Lagrangian can be decomposed as a sum of four terms

$$\mathcal{L}_{SM} = \mathcal{L}_{gauge} + \mathcal{L}_f + \mathcal{L}_{Yuk} + \mathcal{L}_\phi, \quad (1.4)$$

<sup>2</sup>Different field configurations of unobservable fields can result in identical quantities. Transformations between such configurations are called gauge transformation and the absence of change in the measurable quantities is a characteristic called gauge invariance.

that are related to the gauge, fermion, Yukawa and scalar sectors. The gauge Lagrangian regroups the gauge fields of all three symmetry groups, and the fermionic part consists of kinetic energy terms for quarks and leptons. The interaction between fermions and the scalar doublet  $\phi$  gives rise to fermion masses and is described by the Yukawa Lagrangian. The scalar part of the Lagrangian is composed of a kinematic and potential component related to the scalar boson.

For the electroweak theory, two coupling constants are introduced, namely  $g'$  for  $U(1)_Y$  and  $g$  for  $SU(2)_L$ . The physically observable gauge bosons of this theory are the photon field  $A_\mu$ , the Z boson field  $Z_\mu^0$ , and the W boson fields  $W_\mu^\pm$ . These are a superposition of the four gauge fields of  $SU(2)_L \times U(1)_Y$ :

$$A_\mu = \sin\theta_W W_\mu^3 + \cos\theta_W B_\mu, \quad Z_\mu^0 = \cos\theta_W W_\mu^3 - \sin\theta_W B_\mu, \quad \text{and} \quad W_\mu^\pm = \sqrt{\frac{1}{2}} (W_\mu^1 \mp iW_\mu^2), \quad (1.5)$$

where  $\theta_W$  represents the weak mixing angle defined as  $\tan \theta_W = \frac{g'}{g}$ .

The coupling constant representing the strength of the QCD interactions is denoted as  $g_s$ . In QCD there is asymptotic freedom whereby the strong coupling constant becomes weaker as the energy with which the interaction between strongly interacting particles is probed increases, and stronger as the distance between the particles increases. A consequence of this is known as colour confinement, the quarks and gluons can not exist on their own and are not observed individually. They are bound in colour neutral states called hadrons, this process is known as hadronisation.

#### 144 Electroweak symmetry breaking

In  $\mathcal{L}_{\text{gauge}}$  and  $\mathcal{L}_f$  are no mass terms for fermions present because only singlets under  $SU(3)_C \times SU(2)_L \times U(1)_Y$  can acquire a mass with an interaction of the type  $m^2 \phi^\dagger \phi$  without breaking the gauge invariance. In order to accommodate mass terms for fermions and gauge fields, electroweak symmetry breaking, leading to  $\mathcal{L}_\phi$  is introduced.

The scalar doublet is introduced in the SM as

$$\phi = \frac{1}{\sqrt{2}} \begin{pmatrix} \varphi_1 + i\varphi_2 \\ \varphi_3 + i\varphi_4 \end{pmatrix}. \quad (1.6)$$

Its field potential is of the form

$$V(\phi) = \mu^2 \phi^\dagger \phi + \lambda (\phi^\dagger \phi)^2, \quad (1.7)$$

with  $\mu^2 < 0$  and  $\lambda$  a positive integer. This choice of parameters gives the potential a "Mexican hat" shape. It has an infinite set of minima (ground states) and by expanding the field around an arbitrary choice of ground state, the electroweak symmetry is broken (EW):

$$\phi = \begin{pmatrix} 0 \\ \frac{v}{\sqrt{2}} \end{pmatrix} + \hat{\phi}, \quad (1.8)$$

where  $v$  is the vacuum expectation value (vev), measured to be around 245 GeV and corresponds to  $\sqrt{\frac{-\mu}{\lambda}}$ . The scalar doublet's four degrees of freedom are reduced to three degrees of freedom

that couple to the gauge fields and fix the  $W^+$ ,  $W^-$  and Zbosons. The remaining fourth degree of freedom has given rise to a physically observable particle, called the Brout-Englert-Higgs (BEH) boson. This spontaneous symmetry breaking leaves the gauge invariance intact and gives masses to the  $W^\pm$  and Zbosons as:

$$m_W = \frac{1}{2}v|g| \quad \text{and} \quad m_Z = \frac{1}{2}v\sqrt{g'^2 + g^2}. \quad (1.9)$$

- 149 The Brout-Englert-Higgs field couples universally to fermions with a strength proportional to  
150 their masses, and to gauge bosons with a strength proportional to the square of their masses.

### 151 1.3 Flavours in the SM

Flavour changing charged currents are introduced in 1963 by Nicola Cabibbo [12]. Via interactions with a W boson the flavour of the quarks is changed. At the time of the postulation only up, down, and strange quarks were known and the charged weak current was described as a coupling between the up quark and  $d_{\text{weak}}$ , where  $d_{\text{weak}}$  is a linear combination of the down and strange quarks,  $d_{\text{weak}} = \cos\theta_c d + \sin\theta_c s$ . This linear combination is a direct consequence of the chosen rotation

$$\begin{pmatrix} d_{\text{weak}} \\ s_{\text{weak}} \end{pmatrix} = \begin{pmatrix} \cos\theta_c & \sin\theta_c \\ -\sin\theta_c & \cos\theta_c \end{pmatrix} \begin{pmatrix} d \\ s \end{pmatrix} = \mathcal{R} \begin{pmatrix} d \\ s \end{pmatrix}, \quad (1.10)$$

where the rotation angle  $\theta_c$  is known as the Cabibbo angle. This provides a definition for the charged weak current between u and d quarks,

$$J_\mu = \bar{u}\gamma_\mu(1 + \gamma_5)d_{\text{weak}}. \quad (1.11)$$

A consequence of Cabibbo's approach is that the  $s_{\text{weak}}$  is left uncoupled, leading to Glashow, Iliopoulos and Maiani (GIM) [13–15] to require the existence of a fourth quark with charge  $\frac{2}{3}q_e$ . This quark, known as the charm quark, couples to  $s_{\text{weak}}$  and a new definition of the charged weak current is modified to

$$J_\mu = (\bar{u} \quad \bar{c}) \gamma_\mu (1 + \gamma_5) \mathcal{R} \begin{pmatrix} d \\ s \end{pmatrix} = \bar{U} \gamma_\mu (1 + \gamma_5) \mathcal{R} D. \quad (1.12)$$

The neutral weak current is defined as

$$J_3 = \bar{U} \gamma_\mu (1 + \gamma_5) [\mathcal{R}, \mathcal{R}^\dagger] D, \quad (1.13)$$

- 152 and is diagonal in flavour space. This has as consequence that no flavour changing neutral  
153 currents occur at tree-level interactions [1].

Kobayashi and Maskawa generalised the Cabibbo rotation matrix to accommodate a third generation of quarks. The result is a  $3 \times 3$  unitary matrix known as the CKM matrix, responsible for the mixing of weak interaction states of down-type quarks:

$$\begin{pmatrix} d_{\text{weak}} \\ s_{\text{weak}} \\ b_{\text{weak}} \end{pmatrix} = \begin{pmatrix} V_{ud} & V_{us} & V_{ub} \\ V_{cd} & V_{cs} & V_{cb} \\ V_{td} & V_{ts} & V_{tb} \end{pmatrix} \begin{pmatrix} d \\ s \\ b \end{pmatrix} = \mathcal{V}_{\text{CKM}} \begin{pmatrix} d \\ s \\ b \end{pmatrix}, \quad (1.14)$$

where  $\mathcal{V}_{\text{CKM}}$  is unitary ( $\mathcal{V}_{\text{CKM}}^\dagger \mathcal{V}_{\text{CKM}} = \mathbb{1}$ ). A general  $3 \times 3$  unitary matrix depends on three real angles and six phases. For the CKM matrix, the freedom to redefine the phases of the quark eigenstates can remove five of the phases, leaving a single physical phase known as the Kobayashi-Maskawa phase. This phase is responsible for the charge parity violation in the SM [16]. Each element  $V_{ij}$  of  $\mathcal{V}_{\text{CKM}}$  represents the transition probability of a quark  $i$  going to a quark  $j$ , and is experimentally determined to be [6]

$$\mathcal{V}_{\text{CKM}} = \begin{pmatrix} 0.97425 \pm 0.00022 & 0.2253 \pm 0.0008 & (4.13 \pm 0.49) \times 10^{-3} \\ 0.225 \pm 0.008 & 0.986 \pm 0.016 & (41.1 \pm 1.3) \times 10^{-3} \\ (8.4 \pm 0.6) \times 10^{-3} & (40.0 \pm 2.7) \times 10^{-3} & 1.021 \pm 0.032 \end{pmatrix}. \quad (1.15)$$

154 From Equation 1.15 follows that top quarks predominantly decay via charged weak currents  
 155 to bottom quarks, with a probability consistent with unity. In the SM, FCNC can only occur via  
 156 higher loop interactions which are highly suppressed. The expected transition probabilities for  
 157 a top quark decaying via a FCNC interaction in the SM are given in Table 1.4, where it is clear  
 158 that the FCNC top quark interactions of the SM is still beyond the reach of the sensitivity of  
 current experiments.

**Table 1.4:** The predicted branching ratios  $\mathcal{B}$  for FCNC decays involving the top quark in the SM [17].

Process	$\mathcal{B}$ in the SM	Process	$\mathcal{B}$ in the SM
$t \rightarrow uZ$	$8 \times 10^{-17}$	$t \rightarrow cZ$	$1 \times 10^{-14}$
$t \rightarrow u\gamma$	$4 \times 10^{-16}$	$t \rightarrow c\gamma$	$5 \times 10^{-14}$
$t \rightarrow ug$	$4 \times 10^{-14}$	$t \rightarrow cg$	$5 \times 10^{-12}$
$t \rightarrow uH$	$2 \times 10^{-17}$	$t \rightarrow cH$	$3 \times 10^{-15}$

159

## 160 1.4 The top quark in the SM

Discovered in 1995 by the CDF and D0 collaborations at the Tevatron with proton-antiproton data [18, 19], the top quark plays an important role in studying high energy physics. Its Yukawa interaction is given by

$$\mathcal{L}_{\text{top-Yukawa}} = -\frac{\lambda_t v}{\sqrt{2}} \bar{t}_L t_R - \frac{\lambda_t}{\sqrt{2}} H \bar{t}_L t_R + \text{h.c.}, \quad (1.16)$$

yielding a Yukawa coupling of [6]

$$\lambda_t = \frac{\sqrt{2} m_t}{v} = 0.991 \pm 0.003. \quad (1.17)$$

161 This Yukawa coupling is very large compared to the other Yukawa couplings in the SM ( $\mathcal{O}(10^{-2})$ ),  
 162 leading to the belief that the top quark may have an important role in understanding the  
 163 mechanism of electroweak symmetry breaking. On top of this, the very short lifetime of the top  
 164 quark makes it an excellent candidate to study the properties of a bare quark. Its high mass,  
 165 almost 40 times higher than the mass of the closest fermion in mass, leads to a large coupling

166 with the Higgs boson and makes the top quark an interesting candidate to investigate how  
 167 particles acquire mass.

168 The CKM matrix element  $V_{tb}$ , given in [Equation 1.15](#), is experimentally found to be much  
 169 larger than  $V_{ts}$ ,  $V_{td}$ , and close to unity. The top quark decays through electroweak interactions  
 170 since the W boson mass is smaller than the top quark mass and the W boson can be on shell. A  
 171 consequence of this is that the top quark has a very short lifetime of only  $1/\Gamma_t \approx 5 \cdot 10^{-25}$  s [6]  
 172 leading to the fact that the formation of bound states involving top quarks are not allowed.  
 173 This lifetime is even shorter than the typical hadronisation timescale of  $1/\Lambda_{QCD} \approx 10^{-23}$  s,  
 174 prohibiting gluons to radiate from the top quark and keeping its spin coherent. Since the  
 175 electroweak interactions have a vector-axial vector (V-A) coupling structure<sup>3</sup>, the top quark  
 176 spin orientation can be derived from the angular distributions of its decay products. This makes  
 177 it possible to study the polarisation of top quarks from the angular distributions in various  
 178 processes.

179 The massiveness of the top quark leads to the fact that a large amount of energy is needed to  
 180 create one. This is only the case for high energy collisions such as those happening in the Earth's  
 181 upper atmosphere when cosmic rays collide with particles in air, or by particle accelerators.  
 182 The production of top quarks happens in two ways: single via the electroweak interaction or in  
 183 pairs via the strong interaction. At hadron colliders, the dominant production mechanism is top  
 184 quark production via gluon ( $gg \rightarrow t\bar{t}$ ) or quark fusion ( $q\bar{q} \rightarrow t\bar{t}$ ). In [Figure 1.1](#), the different top  
 185 quark pair production mechanisms are shown. The production channel of gluon fusion is the  
 186 main contributor to the top quark pair cross section at the LHC compared to quark fusion at the  
 187 Tevatron. The  $gg \rightarrow t\bar{t}$  process contributes 80-90% to the total top quark pair cross section in  
 188 the LHC centre-of-mass energy regime of 7-14 TeV [6]. In [Table 1.5](#) the predicted top quark  
 189 pair production cross sections are given for the LHC and the Tevatron, while in [Figure 1.2](#), a  
 190 summary plot of the LHC and Tevatron top quark pair cross section measurements as a function  
 of the centre-of-mass energy can be found.

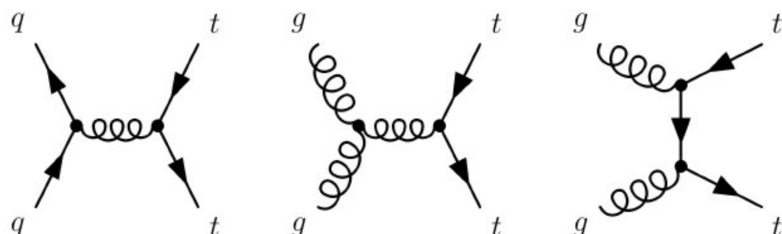


**Figure 1.1:** Leading order diagrams of the top quark pair production. Gluon fusion (right and middle) are the dominant processes at the LHC, while quark fusion (left) is the dominant one at the Tevatron.

191

192 The singly produced top quarks are produced via the electroweak interaction. These production  
 193 mechanisms are subdivided at leading order into three main channels based on the virtuality  
 194 ( $Q^2 = -p_\mu p^\mu$ ) of the exchanged W boson. In [Figure 1.3](#), the corresponding Feynman diagrams  
 195 are shown. The single top quark production cross sections, given in [Table 1.6](#), are smaller than

<sup>3</sup>In the SM a vector - axial vector coupling structure ( $\gamma^\mu - \gamma^\mu \gamma^5$ ) is predicted that only permits left-handed fermions or right-handed anti fermions to interact with a spin-1 particle.

**Table 1.5:** Predictions on the top quark pair production cross sections at next-to-next-to-leading order with next-to-next-to-leading log soft gluon resummation per centre-of-mass energy [6]. The first uncertainty is from scale dependence, while the second uncertainty originates from parton density functions.

Experiment	Top quark mass	Centre-of-mass energy	Cross section (pb)
Tevatron	$m_t = 173.3$ GeV	$\sqrt{s} = 1.96$ TeV	$\sigma_{t\bar{t}} = 7.16^{+0.11+0.17}_{-0.20-0.12}$
LHC	$m_t = 173.2$ GeV	$\sqrt{s} = 7$ TeV	$\sigma_{t\bar{t}} = 173.6^{+4.5+8.9}_{-5.9-8.9}$
LHC	$m_t = 173.2$ GeV	$\sqrt{s} = 8$ TeV	$\sigma_{t\bar{t}} = 247.7^{+6.3+11.5}_{-8.5-11.5}$
LHC	$m_t = 173.2$ GeV	$\sqrt{s} = 13$ TeV	$\sigma_{t\bar{t}} = 816.0^{+19.4+34.4}_{-28.6-34.4}$

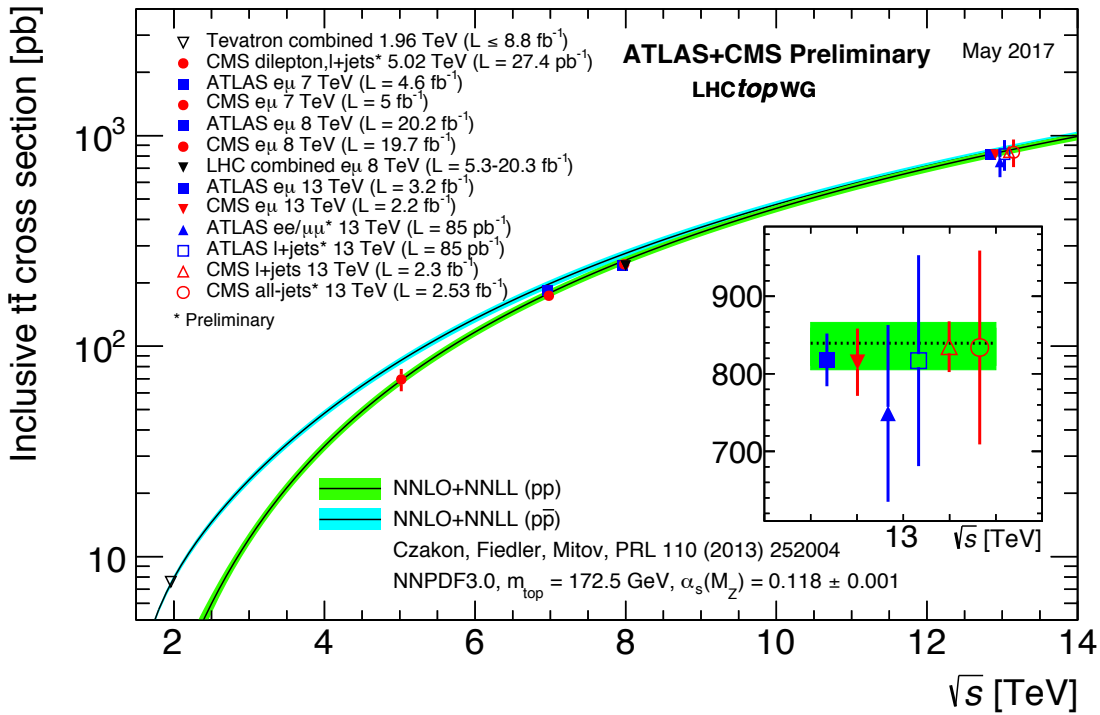


**Figure 1.2:** Summary of the LHC and the Tevatron measurements of the top quark pair production cross section as function of the centre-of-mass energy compared with the next-to-next-to-leading order QCD calculation. The theory bands are the uncertainties due to renormalization and factorisation scales, parton density functions and the strong coupling. The mass of the top quark is assumed to be 172.5 GeV. Measurements for the same centre-of-mass energy are slightly off-set for clarity. Figure taken from [20].

196 the top quark pair production cross sections since the electroweak coupling strength is smaller  
 197 than the strong coupling strength. In addition, for the single top quark production, there is the  
 198 need of sea quarks ( $b, \bar{q}$ ) in the initial states for which the parton density functions increase  
 less steeply at low momentum fractions compared to the gluon parton density functions.

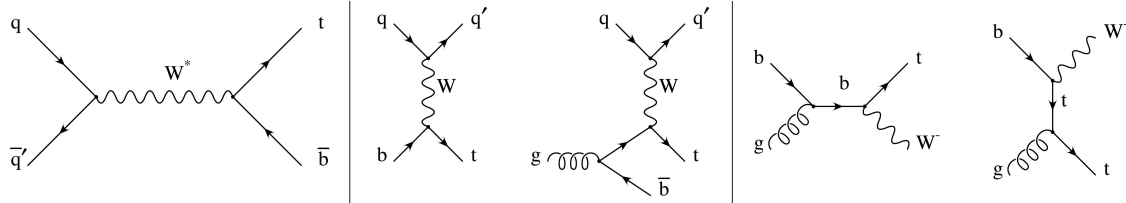


**Figure 1.3:** Leading order Feynman diagrams of the electroweak production of single top quarks in the  $s$ -channel (left),  $t$ -channel (middle), and for the  $tW$  associated production. Figure taken from [21].

199

200 The production via the  $t$ -channel has a virtuality of the  $W$  boson  $Q^2 > 0$ , making it space-like.  
 201 It is produced via the scattering of the  $W$  boson of a bottom quark coming from a proton  
 202 or from gluon splitting ( $g \rightarrow b\bar{b}$ ). It has the highest single top quark cross section in proton  
 203 collisions and the top quark production is roughly twice as large than the antitop quark. This is  
 204 a consequence of the up-down valence quark composition of the proton. This feature makes  
 205 the  $t$ -channel sensitive to the parton density functions of the proton. The  $s$ -channel is the  
 206 production mechanism with the smallest cross section. Here the  $W$  boson is time-like ( $Q^2 < 0$ )  
 207 which requires the  $W$  boson to have a large virtuality to produce the heavier top quark. It is  
 208 produced from two quarks belonging to the same isodoublet (e.g.  $u\bar{d}$ ) and subsequently decays  
 209 to  $t\bar{b}$ . This process get enhanced by many beyond the Standard Model scenarios via the addition  
 210 of new heavy particles such as  $W'$ . The  $tW$ -channel has a top quark produced in association  
 211 with a  $W$  boson produced on shell  $Q^2 = -m_W^2$ . This mode is negligible at the Tevatron, but of  
 212 relevant size at the LHC. The  $tW$ -channel is sensitive to new physics affecting the  $Wtb$  vertex.  
 213 The single top quark production cross section measurements by the CMS collaboration can be  
 214 found in Figure 1.4.

**Table 1.6:** Predictions on the single top quark production cross sections at next-to-leading order per centre-of-mass energy [6]. The uncertainties from scale dependence and from parton density functions are combined in quadrature or given separately (scale + PDF). For the  $t$ -channel the relative proportions to  $t$  and  $\bar{t}$  are 65% and 35%. For the  $s$ -channel this is respectively 69% and 31%. The  $tW$ -channel has an equal proportion of top and antitop quarks. For Tevatron, the top quark mass is assumed to be 173.3 GeV, while the LHC predictions use  $m_t = 172.5$  GeV [6, 22].

Collider	Centre-of-mass energy	Cross section $\sigma_{t+\bar{t}}$ (pb)		
		$t$ -channel	$s$ -channel	$tW$ -channel
Tevatron	$\sqrt{s} = 1.96$ TeV	$2.06^{+0.13}_{-0.13}$	$1.03^{+0.05}_{-0.05}$	-
LHC	$\sqrt{s} = 7$ TeV	$63.89^{+2.91}_{-2.52}$	$4.29^{+0.19}_{-0.17}$	$15.74^{+0.40+1.10}_{-0.40-1.14}$
LHC	$\sqrt{s} = 8$ TeV	$84.69^{+3.76}_{-3.23}$	$5.24^{+0.22}_{-0.20}$	$22.37^{+0.60+1.40}_{-0.60-1.40}$
LHC	$\sqrt{s} = 13$ TeV	$216.99^{+9.04}_{-7.71}$	$10.32^{+0.40}_{-0.36}$	$71.7^{+1.80+3.40}_{-1.80-3.40}$

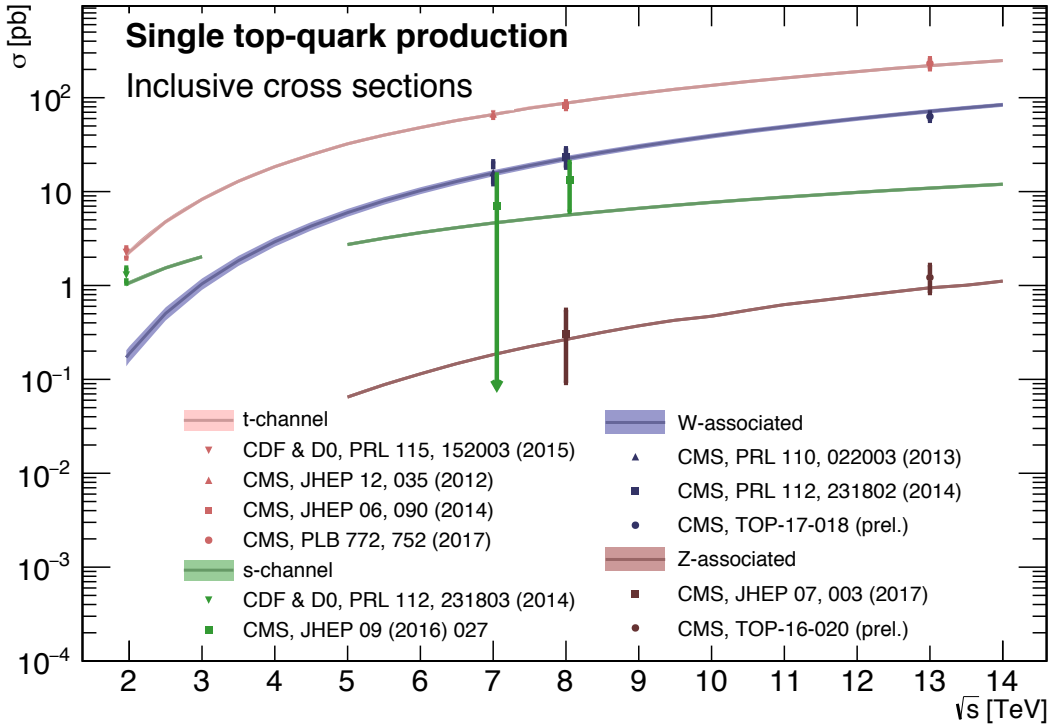


**Figure 1.4:** Summary of the measurements of the single top quark production cross section as function of the centre-of-mass energy. Figure taken from [23].

## 215 1.5 Effective field theories

216 Problems can be simplified if one looks at the relevant scale of the process that one want to  
 217 investigate, for example the chemical properties of an hydrogen atom can be described without  
 218 any knowledge of quark interactions inside the proton. In this case, the proton can be considered  
 219 the elementary object (indivisible) due to the fact that the binding energy of the constituents is  
 220 much bigger than the energy of the electron in orbit around the proton. Effective field theories  
 221 are based on this kind of separation of different energy scales in a system [24]. Effective field  
 222 theories can be used for theories where the perturbative expansion cannot be trusted, e.g. QCD  
 223 at low energy, or as bottom up approach to look for new physics in a model independent way.  
 224 The latter is the way effective field theory will be used throughout this thesis.

The main idea behind effective field theory is easily explained via the example of the Fermi theory. Fermi explained in 1933 [25] the  $\beta$ -decay as a product of currents:

$$\mathcal{L}_{\text{EFT}}^{\text{Fermi}} = -\frac{G_F}{\sqrt{2}} J^\mu J_\mu^\dagger, \quad (1.18)$$

where  $G_F$  is the Fermi coupling constant, measured to be  $G_F \approx 1.17 \times 10^{-5} \text{ GeV}^{-2}$ . The current  $J_\mu$  can written as the sum of an hadronic  $J_\mu^h$  and leptonic  $J_\mu^l$  current, where for simplicity only

the leptonic current will be used further.

$$J_\mu^l = \sum_l \bar{\nu}_l \gamma_\mu (1 - \gamma_5) l. \quad (1.19)$$

225 Historically, charged currents were flavour universal and the later discovered parity violation of  
 226 the weak interaction led to the V-A structure. After this the  $SU(2)_L$  symmetry was postulated  
 227 and the existence of neutral currents was predicted. The effective Lagrangian used then (given  
 228 in [Equation 1.18](#)), could nowadays be build starting from  $SU(2)_L$  symmetries only.

The muon decay can be computed from two different starting points. The effective Fermi Lagrangian provides the decay width of the muon into an electron and two neutrinos

$$\Gamma(\mu \rightarrow e \bar{\nu}_e \nu_\mu) \approx \frac{1}{96\pi^3} \frac{m_\mu^2}{\Lambda_F^4}, \quad (1.20)$$

where  $\Lambda_F$  is the energy scale defined as

$$\frac{G_F}{\sqrt{2}} = \frac{1}{\Lambda_F^2}. \quad (1.21)$$

From muon decay measurements, the value of  $\Lambda_F$  is determined to be  $\Lambda_F \approx 348\text{GeV}$  [[24](#)]. From the SM Lagrangian, one could also calculate the muon decay. Considering that the momenta involved are small compared to the W boson mass, the propagator's denominator can be expanded as [[1](#)]

$$\frac{1}{p^2 - m_W^2} = -\frac{1}{m_W^2} - \frac{p^2}{m_W^4} + \dots \quad (1.22)$$

Looking at the first term, and identifying

$$\frac{g^2}{8m_W} = \frac{1}{\Lambda_F^2}, \quad (1.23)$$

229 one sees that this corresponds with [Equation 1.20](#), thus the effective Lagrangian in [Equation](#)  
 230 [1.18](#) is the first term of the expansion in  $\frac{1}{m_W^2}$  applied on the full Lagrangian.

231 An effective theory is thus a Taylor expansion in the ratio of two scales and the only remnants  
 232 of the full theory at low energies are the symmetries and the values of the coupling constants.  
 233 If the expansion parameter is small, one can truncate the series leading to the Lagrangian  
 234 containing a finite number of free coefficients, making predictions possible. The error on these  
 235 predictions are then of the order as the truncated piece.

The SM can be seen as an effective theory applicable up to energies not exceeding a scale  $\Lambda$ . Therefore, remnants should still be valid and the theory above that scale should have a gauge group containing  $SU(3)_C \times SU(2)_L \times U(1)_Y$  and all the SM degrees of freedom, as well as reduce to the SM at lower energies. The general SM Lagrangian becomes then

$$\mathcal{L}_{\text{SM+EFT}} = \mathcal{L}_{\text{SM}}^{(4)} + \frac{1}{\Lambda} \sum_k C_k^{(5)} Q_k^{(5)} + \frac{1}{\Lambda^2} \sum_k C_k^{(6)} Q_k^{(6)} + \mathcal{O}\left(\frac{1}{\Lambda^3}\right), \quad (1.24)$$

236 where  $Q_k^{(n)}$  are dimension- $n$  operators (currents) and  $C_k^{(n)}$  the corresponding dimensionless  
237 coupling constants, so-called Wilson coefficients. The Wilson coefficients are determined by the  
238 underlying high energy theory.

239 In the Warsaw basis [26], a set of independent operators of dimension 5 and 6 are built out  
240 of the SM fields and are consistent with the SM gauge symmetries and is fully derived in Ref.  
241 [26]. In general the various measurements show a good agreement with the SM predictions  
242 and by lack of deviations from the SM, limits on the anomalous couplings can be derived. The  
243 estimated coupling strengths per operator contributing to single top quark production obtained  
244 from various measurements at the LHC and Tevatron are shown in Figure 1.5 for which the  
245 conventions are discussed in Ref. [27]. These results are consistent with the SM expectation for  
246 which those operators vanish.

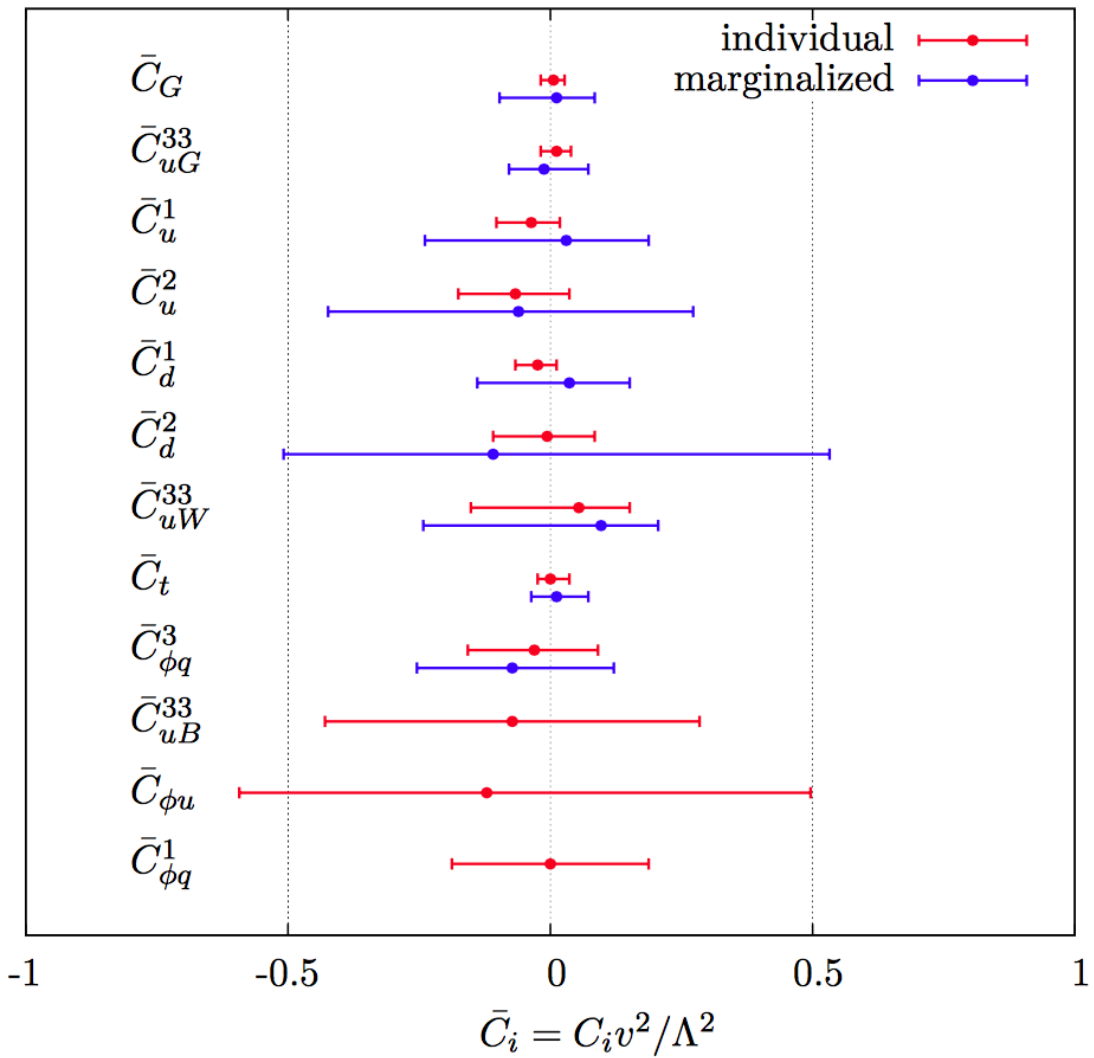


**Figure 1.5:** Global fit results of top quark effective field theory to experimental data including all constrained operators at dimension six. For the operators, the Warsaw basis of [26] is used. The bounds are set on the Wilson coefficients of various operators contributing to top quark production and decay in two cases (red) all other coefficients set to zero, or (blue) all other coefficients marginalized over. Figure taken from [28].

## 247 1.6 Motivation for new physics

248 Many high energy experiments confirm the success of the SM. In particular the scalar boson,  
 249 the cornerstone of the SM, has consecrated the theory. Unfortunately there are also strong  
 250 indications that the SM ought to be a lower energy expression of a more global theory. The  
 251 existence of physics beyond the SM (BSM) [29] is strongly motivated. These motivations are  
 252 based on direct evidence from observation such as the existence of neutrino masses, the existence  
 253 of dark matter and dark energy, or the matter-antimatter asymmetry, and also from theoretical  
 254 problems such as the hierarchy problem, the coupling unification or the large numbers of free  
 255 parameters in the SM.

256 In the SM, the neutrinos are assumed to be massless, while experiments with solar, atmospheric,  
 257 reactor and accelerator neutrinos have established that neutrinos can oscillate and change flavour  
 258 during flight [4, 5]. These oscillations are only possible when neutrinos have masses. The  
 259 flavour neutrinos ( $\nu_e$ ,  $\nu_\mu$ ,  $\nu_\tau$ ) are then linear expressions of the fields of at least three mass  
 260 eigenstate neutrinos  $\nu_1$ ,  $\nu_2$ , and  $\nu_3$ .

261 The ordinary or baryonic matter described by the SM describes only 5% of the mass (energy)  
 262 content of the universe. Astrophysical evidence indicated that dark matter is contributing  
 263 to approximately 27%, and dark energy to 68% of the content of the universe. From the  
 264 measurements of the temperature and polarizations anisotropies of the cosmic microwave  
 265 background by the Planck experiment [30], the density of cold non baryonic matter is determined.  
 266 Cold dark matter is assumed to be only sensitive to the weak and gravitational force, leading  
 267 to only one possible SM candidate: the neutrino. However, these are too light to account for  
 268 the vast amount of dark matter and other models are needed. Dark energy is assumed to be  
 269 responsible for the acceleration in the expansion of the universe [31].

270 At the Big Bang matter and antimatter are assumed to be produced in equal quantities.  
 271 However, it is clear that we are surrounded by matter. So where did all the antimatter go?  
 272 In 1967, Sakharov identified three mechanisms that are necessary to obtain a global matter  
 273 antimatter asymmetry [32]. These mechanisms are those of baryon and lepton number violation,  
 274 that at a given moment in time there was a thermal imbalance for the interactions in the universe,  
 275 and there is charge C and charge parity CP violation<sup>4</sup>.

276 The large number of free parameters in the SM comes from the nine fermion masses, three  
 277 CKM mixing angles and one CP violating phase, one EM coupling constant  $g'$ , one weak coupling  
 278 constant  $g$ , one strong coupling constant  $g_s$ , one QCD vacuum angle, one vacuum expectation  
 279 value, and one mass of the scalar boson. This large number of free parameters leads to the  
 280 expectation of a more elegant and profound theory beyond the SM.

281 The hierarchy problem [33] is related to the huge difference in energy between the weak  
 282 scale and the Planck scale. The vev of the Brout-Englert-Higgs field determines the weak scale  
 283 that is approximately 246 GeV. The radiative corrections to the scalar boson squared mass  $m_H^2$ ,  
 284 coming from its self couplings and couplings to fermions and gauge bosons, are quadratically

---

<sup>4</sup>The rate of a process  $i \rightarrow f$  can be different from the CP-conjugate process:  $\tilde{i} \rightarrow \tilde{f}$ . The SM includes sources of CP-violation through the residual phase of the CKM matrix. However, these could not account for the magnitude of the asymmetry observed.

285 proportional to the ultraviolet momentum cut-off  $\Lambda_{\text{UV}}$ . This cut-off is at least equal to the energy  
 286 to which the SM is valid without the need of new physics. For the SM to be valid up to the  
 287 Planck mass, the correction to  $m_H^2$  becomes thirty orders of magnitude larger than  $m_H^2$ . This  
 288 implies that an extraordinary cancellation of terms should happen. This is also known as the  
 289 naturalness problem of the H boson mass.

The correction to the squared mass of the scalar boson coming from a fermion  $f$ , coupling to the scalar field  $\phi$  with a coupling  $\lambda_f$  is given by

$$\Delta m_H^2 = -\frac{|\lambda_f|^2}{8\pi^2} \Lambda_{\text{UV}}^2, \quad (1.25)$$

while the correction to the mass from a scalar particle  $S$  with a mass  $m_S$ , coupling to the scalar field with a Lagrangian term  $-\lambda_S |\phi|^2 |S|^2$  is

$$\Delta m_H^2 = \frac{|\lambda_S|^2}{16\pi^2} \left( \Lambda_{\text{UV}}^2 - 2m_S^2 \ln \left( \frac{\Lambda_{\text{UV}}}{m_S} \right) + \dots \right). \quad (1.26)$$

290 As one can see the correction term to  $m_H^2$  is much larger than  $m_H^2$  itself. By introducing BSM  
 291 physics models that introduce new scalar particles at the TeV scale that couple to the scalar  
 292 boson one can cancel the  $\Lambda_{\text{UV}}^2$  divergence and avoid this fine-tuning.

293 The choice of the  $SU(3)_C \times SU(2)_L \times U(1)_Y$  symmetry group itself as well as the separate  
 294 treatment of the three forces included in the SM raises concern. The intensity of the forces  
 295 show a large disparity around the electroweak scale, but have comparable strengths at higher  
 296 energies. The electromagnetic and weak forces are unified in a electroweak interaction, but the  
 297 strong coupling constant does not encounter the other coupling constants at high energies. In  
 298 order to reach a grand unification, the running of couplings can be modified by the addition of  
 299 new particles in BSM models.

## 300 1.7 An effective approach beyond the SM: FCNC involving a top 301 quark

302 The closeness of the top quark mass to the electroweak scale led physicist to believe that it  
 303 is a sensitive probe for new physics. Studying its properties is therefore an important topic  
 304 of the experimental program at the LHC. Several extensions of the SM enhance the FCNC  
 305 branching ratios and can be probed at the LHC [17], from which some of them are shown in  
 306 Table 1.7. Previous searches have been performed at the Tevatron by the CDF [34] and D0 [35]  
 307 collaborations, and at the LHC by the ATLAS [36–40] and CMS [41–45] collaborations.

308 The impact of BSM models can be written in a model independent way by means of an  
 309 effective field theory valid up to an energy scale  $\Lambda$ . The leading effects are parametrized by a  
 310 set of fully gauge symmetric operators that are added to the SM Lagrangian and can be reduced  
 311 to a minimal set of operators as seen in Equation 1.24. For simplicity, the assumption is made  
 312 that new physics effects are exclusively described by dimension-6 operators, thus neglecting

**Table 1.7:** The predicted branching ratios  $\mathcal{B}$  for FCNC interactions involving the top quark in some BSM models [17]: quark singlet (QS), generic two Higgs doublet model (2HDM) and the minimal supersymmetric extensions to the SM (MSSM);

Process	QS	2HDM	MSSM	Process	QS	2HDM	MSSM
$t \rightarrow uZ$	$\leq 1.1 \times 10^{-4}$	—	$\leq 2 \times 10^{-6}$	$t \rightarrow cZ$	$\leq 1.1 \times 10^{-4}$	$\leq 10^{-7}$	$\leq 2 \times 10^{-6}$
$t \rightarrow u\gamma$	$\leq 7.5 \times 10^{-9}$	—	$\leq 2 \times 10^{-6}$	$t \rightarrow c\gamma$	$\leq 7.5 \times 10^{-9}$	$\leq 10^{-6}$	$\leq 2 \times 10^{-6}$
$t \rightarrow ug$	$\leq 1.5 \times 10^{-7}$	—	$\leq 8 \times 10^{-5}$	$t \rightarrow cg$	$\leq 1.5 \times 10^{-7}$	$\leq 10^{-4}$	$\leq 8 \times 10^{-5}$
$t \rightarrow uH$	$\leq 4.1 \times 10^{-5}$	$\leq 5.5 \times 10^{-6}$	$\leq 10^{-5}$	$t \rightarrow cH$	$\leq 4.1 \times 10^{-5}$	$\leq 10^{-3}$	$\leq 10^{-5}$

313 neutrino physics. In the fully gauge symmetric case, the EFT Lagrangian is then given by

$$\mathcal{L}_{\text{SM+EFT}} = \mathcal{L}_{\text{SM}} + \sum_i \frac{\bar{c}_i}{\Lambda^2} O_i + \mathcal{O}\left(\frac{1}{\Lambda^3}\right), \quad (1.27)$$

where the Wilson coefficients  $\bar{c}_i$  depend on the considered theory and on the way that new physics couples to the SM particles. Considering that  $\Lambda$  is large, contributions suppressed by powers of  $\Lambda$  greater than two are neglected. Moreover, all four fermion operators are omitted for the rest of this thesis. The Warsaw basis is adopted for the independent effective operators [26], parametrising the new physics effects relevant for the flavour changing neutral current interactions of the top quark as, all flavour indices understood,

$$\begin{aligned} \mathcal{L}_{\text{EFT}}^t = & \frac{\bar{c}_{uG}}{\Lambda^2} \Phi^\dagger \cdot [\bar{Q}_L \sigma^{\mu\nu} \mathcal{T}_a u_R] G_{\mu\nu}^a + \frac{\bar{c}_{uB}}{\Lambda^2} \Phi^\dagger \cdot [\bar{Q}_L \sigma^{\mu\nu} u_R] B_{\mu\nu} + \frac{2\bar{c}_{uW}}{\Lambda^2} \Phi^\dagger T_i \cdot [\bar{Q}_L \sigma^{\mu\nu} u_R] W_{\mu\nu}^i \\ & + i \frac{\bar{c}_{hu}}{\Lambda^2} \left[ \Phi^\dagger \overleftrightarrow{D}_\mu \Phi \right] [\bar{u}_R \gamma^\mu u_R] + i \frac{\bar{c}_{hq}^{(1)}}{\Lambda^2} \left[ \Phi^\dagger \overleftrightarrow{D}_\mu \Phi \right] [\bar{Q}_L \gamma^\mu Q_L] \\ & + i \frac{4\bar{c}_{HQ}^{(3)}}{\Lambda^2} \left[ \Phi^\dagger T_i \overleftrightarrow{D}_\mu \Phi \right] [\bar{Q}_L \gamma^\mu T^i Q_L] + \frac{\bar{c}_{uh}}{\Lambda^2} \Phi^\dagger \Phi \Phi^\dagger \cdot [\bar{Q}_L u_R] + \text{h.c.}, \end{aligned} \quad (1.28)$$

where the left handed  $SU(2)_L$  doublet of the quark fields is denoted by  $Q_L$ , the up-type right handed fields by  $u_R$ , the down-type right handed fields by  $d_R$ , the  $SU(2)_L$  doublet of the Higgs field by  $\Phi$ , the field strength tensors as

$$\begin{aligned} B_{\mu\nu} &= \partial_\mu B_\nu - \partial_\nu B_\mu, \\ W_{\mu\nu}^k &= \partial_\mu W_\nu^k - \partial_\nu W_\mu^k - g \epsilon_{ij}^k W_\mu^i W_\nu^j, \\ G_{\mu\nu} &= \partial_\mu G_\nu^a - \partial_\nu G_\mu^a + g_s f_{bc}^a G_\mu^b G_\nu^c, \end{aligned} \quad (1.29)$$

denoting the structure constant of the  $SU(3)_C$  group as  $f_{bc}^a$  and the structure constant of the  $SU(2)_L$  group as  $\epsilon_{ij}^k$ . The gauge covariant derivatives are also standard defined as

$$D_\mu \Phi = \partial_\mu \Phi - \frac{1}{2} i g' B_\mu \Phi - i g T_k W_\mu^k \Phi \quad (1.30)$$

with the conventions of Section 1.2. The representation matrices  $T$  of  $SU(2)_L$  are defined in Equation 1.1, while the representation matrices  $\mathcal{T}$  of  $SU(3)_C$  are the Gell-Mann matrices [1].

The hermitian derivative operator is defined as

$$\Phi^\dagger \overleftrightarrow{D} \Phi = \Phi^\dagger D^\mu \Phi - D_\mu \Phi^\dagger \Phi. \quad (1.31)$$

After electroweak symmetry breaking the operators induce [17, 46] both corrections to the SM couplings and new interactions at tree level such as FCNC interactions. The FCNC interactions of the top quark that are not present in the SM are given by

$$\mathcal{L}_{\text{EFT}}^t = \frac{\sqrt{2}}{2} \sum_{q=u,c} \left[ g' \frac{\kappa_{t\gamma q}}{\Lambda} A_{\mu\nu} \bar{t} \sigma^{\mu\nu} (f_{\gamma q}^L P_L + f_{\gamma q}^R P_R) q \right. \quad (1.32)$$

$$+ \frac{g}{2\cos\theta_W} \frac{\kappa_{tZq}}{\Lambda} Z_{\mu\nu} \bar{t} \sigma^{\mu\nu} (f_{Zq}^L P_L + f_{Zq}^R P_R) q \quad (1.33)$$

$$+ \frac{\sqrt{2}g}{4\cos\theta_W} \zeta_{tZq} \bar{t} \gamma^\mu (\tilde{f}_q^L P_L + \tilde{f}_q^R P_R) q Z_\mu \quad (1.34)$$

$$+ g_s \frac{\kappa_{tgq}}{\Lambda} Z_{\mu\nu} \bar{t} \sigma^{\mu\nu} (f_{gq}^L P_L + f_{gq}^R P_R) q G_\mu^a \quad (1.35)$$

$$+ \eta_{Hqt} \bar{t} (\hat{f}_q^L P_L + \hat{f}_q^R P_R) q H + \text{h.c.} \Big], \quad (1.36)$$

where the value of the FCNC couplings at scale  $\Lambda$  are represented by  $\kappa_{tZq}, \kappa_{tgq}, \kappa_{t\gamma q}, \zeta_{tZq}$ , and  $\eta_{Hqt}$ . These are assumed to be real and positive, with the unit of  $\text{GeV}^{-1}$  for  $\kappa_{txq}/\Lambda$  and no unit for  $\zeta_{xqt}$  and  $\eta_{xqt}$ . In the equation  $\sigma^{\mu\nu}$  equals to  $\frac{i}{2} [\gamma^\mu, \gamma^\nu]$ , and the left- and right-handed chirality projector operators are denoted by  $P_L$  and  $P_R$ . The electromagnetic coupling constant is denoted by  $g'$ , the strong interaction coupling is denoted as  $g_s$ , while the electroweak interaction is parametrised by the coupling constant  $g$  and the electroweak mixing angle  $\theta_W$ . The complex chiral parameters are normalized according to  $|f_{xq}^L|^2 + |f_{xq}^R|^2 = 1$ ,  $|\tilde{f}_q^L|^2 + |\tilde{f}_q^R|^2 = 1$ , and  $|\hat{f}_q^L|^2 + |\hat{f}_q^R|^2 = 1$ . In the expression for  $\mathcal{L}_{\text{EFT}}^t$ , the unitary gauge is adopted and the scalar field is expanded around its vacuum expectation value  $v$  with  $H$  being the SM scalar boson, and the field strength tensors of the photon  $A_\mu$ , the gluon field  $G_\mu^{1\dots 8}$ , and the Z boson  $Z_\mu^0$  are defined as

$$\begin{aligned} A_{\mu\nu} &= \partial_\mu A_\nu - \partial_\nu A_\mu, \\ Z_{\mu\nu} &= \partial_\mu Z_\nu - \partial_\nu Z_\mu, \text{ and} \\ G_{\mu\nu} &= \partial_\mu G_\nu^a - \partial_\nu G_\mu^a + g_s f_{bc}^a G_\mu^b G_\nu^c. \end{aligned} \quad (1.37)$$

<sup>314</sup> Note that there are two coupling constants arising in  $\mathcal{L}_{\text{EFT}}^t$ , which is a residue of electroweak  
<sup>315</sup> symmetry breaking. The massive Z boson will appear in both the  $Z_\mu^0$  field as well as the covariant  
<sup>316</sup> derivative, leading to an extra Z-vertex.

317 The relations between the Wilson coefficients in (1.28) and the coupling strengths of the  
 318 interactions in Equation 1.36 can be derived. The 14 effective operators are mapped onto 10  
 319 free parameters providing a more minimal parametrisation of the anomalous interactions of the  
 320 top quark.

$$\begin{aligned}
 \kappa_{tqg} f_{gq}^L &= \frac{\nu}{g_s \Lambda} [\bar{c}_{uG}]_{i3}^*, & \kappa_{tqg} f_{gq}^R &= \frac{\nu}{g_s \Lambda} [\bar{c}_{uG}]_{3i}, \\
 \kappa_{t\gamma q} f_{\gamma q}^L &= \frac{\nu}{g' \Lambda} [\cos\theta_W \bar{c}_{uB} - \sin\theta_W \bar{c}_{uW}]_{i3}^*, & \kappa_{t\gamma q} f_{\gamma q}^R &= \frac{\nu}{g' \Lambda} [\sin\theta_W \bar{c}_{uB} - \cos\theta_W \bar{c}_{uW}]_{3i}, \\
 \kappa_{tZq} f_{Zq}^L &= -\frac{2\cos\theta_W \nu}{g \Lambda} [\sin\theta_W \bar{c}_{uB} + \cos\theta_W \bar{c}_{uW}]_{i3}^*, & \kappa_{tZq} f_{Zq}^R &= -\frac{2\cos\theta_W \nu}{g \Lambda} [\cos\theta_W \bar{c}_{uB} + \sin\theta_W \bar{c}_{uW}]_{3i}, \\
 \zeta_{tZq} \tilde{f}_{Zq}^L &= -\frac{2\nu^2}{\Lambda^2} [(\bar{c}_{hq}^{(1)} - \bar{c}_{hq}^{(3)})_{i3} + (\bar{c}_{hq}^{(1)} - \bar{c}_{hq}^{(3)})_{3i}^*], & \zeta_{tZq} \tilde{f}_{Zq}^R &= -\frac{2\nu^2}{\Lambda^2} [(\bar{c}_{hu})_{i3} + (\bar{c}_{hu})_{3i}^*], \\
 \eta_{tHq} \hat{f}_{Hq}^L &= \frac{3\nu^2}{2\Lambda^2} [\bar{c}_{uh}]_{3i}^*, & \eta_{tHq} \hat{f}_{Hq}^R &= \frac{3\nu^2}{2\Lambda^2} [\bar{c}_{uh}]_{i3}.
 \end{aligned} \tag{1.38}$$

## 321 1.8 Experimental constraints on top-FCNC

Experiments commonly put limits on the branching ratios which allow an easier interpretation across different EFT models by use of the branching ratio

$$\mathcal{B}(t \rightarrow qX) = \frac{\delta_{txq}^2 \Gamma_{t \rightarrow qX}}{\Gamma_t}, \tag{1.39}$$

322 where  $\Gamma_{t \rightarrow qX}$  represents the FCNC decay width<sup>5</sup> for a coupling strength  $\delta_{txq}^2 = 1$ , and  $\Gamma_t$  the full  
 323 decay width of the top quark. In the SM, supposing a top quark mass of 172.5 GeV, the full  
 324 width becomes  $\Gamma_t^{\text{SM}} = 1.32$  GeV [47].

325 Searches for top-FCNC usually adopt a search strategy depending on the experimental set-up  
 326 and the FCNC interaction of interest, looking either for FCNC interactions in the production of a  
 327 single top quark or in its decay for top quark pair interactions. In Figure 1.6, these two cases  
 328 are shown for the tZq vertex.

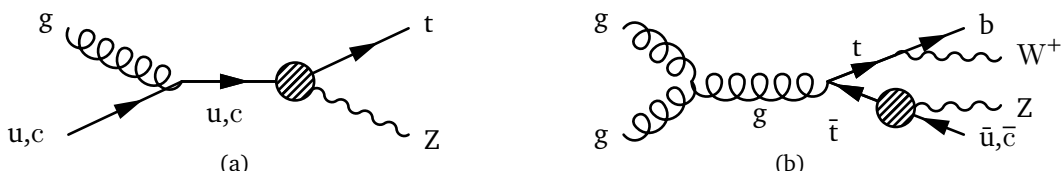


**Figure 1.6:** Feynman diagrams for the processes with a tZq FCNC interaction, where the FCNC interaction is indicated with the shaded dot. (a) Single top quark production through an FCNC interaction. (b) Top quark pair production with an FCNC induced decay.

---

<sup>5</sup>The decay width of a certain process represents the probability per unit time that a particle will decay. The total decay width, defined as the sum of all possible decay widths of a particle, is inversely proportional to its lifetime.

330 The observation of top-FCNC interactions has yet to come and experiments have so far only  
 331 been able to put upper bounds on the branching ratios. An overview of the best current limits is  
 332 given in [Table 1.8](#). In [Figure 1.7](#) a comparison is shown between the current best limits set by  
 333 ATLAS and CMS with respect to several BSM model benchmark predictions. From there one can  
 334 see that FCNC searches involving a Z or H boson are close to excluding or confirming several  
 335 BSM theories. In [Figure 1.9](#), the searches performed by CMS are summarised. For the tZq  
 336 vertex, the best limit from CMS comes from Ref. [41] where both single top quark and top quark  
 337 pair is studied. The observed (expected) limits 95% CL at 8 TeV for the FCNC tZq interaction  
 338 by CMS are  $\mathcal{B}(t \rightarrow uZ) < 2.2 \times 10^{-4}$ ( $2.7 \times 10^{-4}$ ) and  $\mathcal{B}(t \rightarrow cZ) < 4.9 \times 10^{-4}$ ( $12 \times 10^{-4}$ ). In  
 339 [Figure 1.8](#), the summary of the 95% confidence level observed limits on the branching ratios  
 340 of the top quark decays to a charm or up quark and a neutral boson is given, considering the results from the HERA, the LEP, the Tevatron, and the the LHC.

**Table 1.8:** Overview of the most stringent observed and expected experimental limits on top-FCNC branching ratios  $\mathcal{B}$  at 95% confidence level.

Process	Search mode	Observed $\mathcal{B}$	Expected $\mathcal{B}$	Experiment	
$t \rightarrow uZ$	top quark pair decay	$1.7 \times 10^{-4}$	$2.4 \times 10^{-4}$	ATLAS	[40]
$t \rightarrow u\gamma$	single top quark production	$1.3 \times 10^{-4}$	$1.9 \times 10^{-4}$	CMS	[43]
$t \rightarrow ug$	single top quark production	$4.0 \times 10^{-5}$	$3.5 \times 10^{-5}$	ATLAS	[37]
$t \rightarrow uH$	top quark pair decay	$2.4 \times 10^{-3}$	$1.7 \times 10^{-3}$	ATLAS	[39]
$t \rightarrow cZ$	top quark pair decay	$2.3 \times 10^{-4}$	$3.2 \times 10^{-4}$	ATLAS	[40]
$t \rightarrow c\gamma$	single top quark production	$2.0 \times 10^{-3}$	$1.7 \times 10^{-3}$	CMS	[43]
$t \rightarrow cg$	single top quark production	$2.0 \times 10^{-4}$	$1.8 \times 10^{-4}$	ATLAS	[37]
$t \rightarrow cH$	top quark pair decay	$2.2 \times 10^{-3}$	$1.6 \times 10^{-3}$	CMS	[39]

341

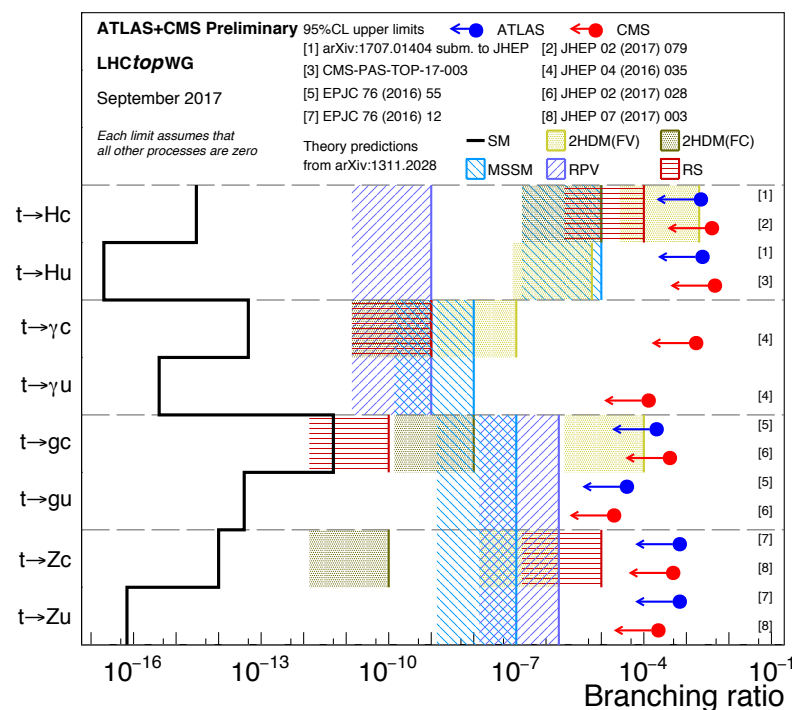


**Figure 1.7:** Current best limits set by CMS and ATLAS for top-FCNC interactions. Figure taken from [23]. (TO DO Remake with new atlas results)

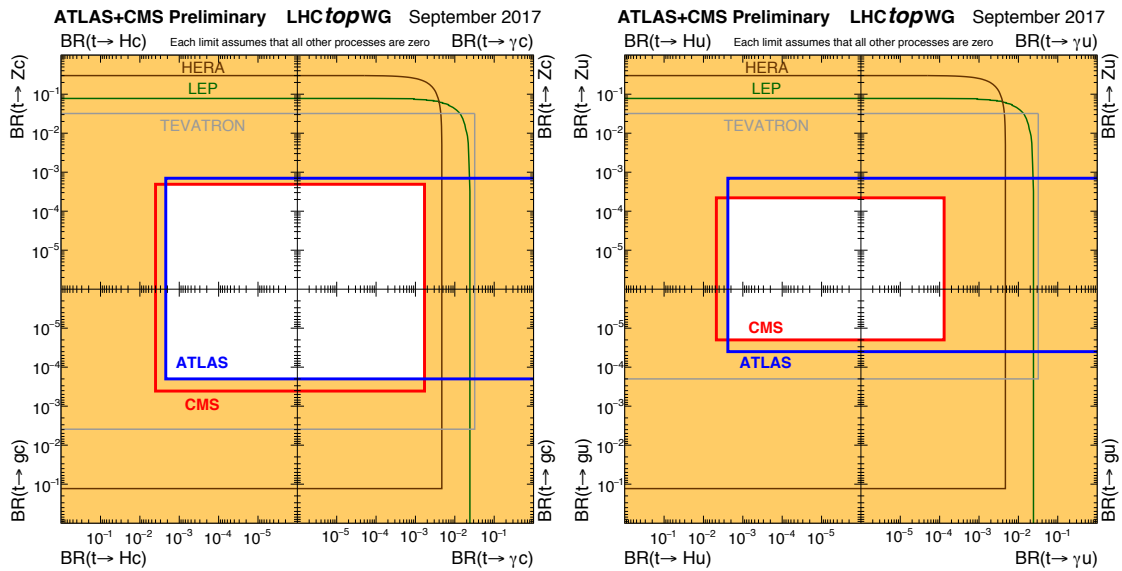


**Figure 1.8:** Summary of the current 95% confidence level observed limits on the branching ratios of the top quark decays via flavour changing neutral currents to a charm (left) or up (right) quark and a neutral boson. The coloured lines represent the results from HERA (the most stringent limits between the ones obtained by the H1 and ZEUS collaborations, in brown), LEP (combined ALEPH, DELPHI, L3 and OPAL collaborations result, in green), TEVATRON (the most stringent limits between the ones obtained by the CDF and D0 collaborations, in grey). The yellow area represents the region excluded by the ATLAS and the CMS Collaborations. Figure taken from [20].

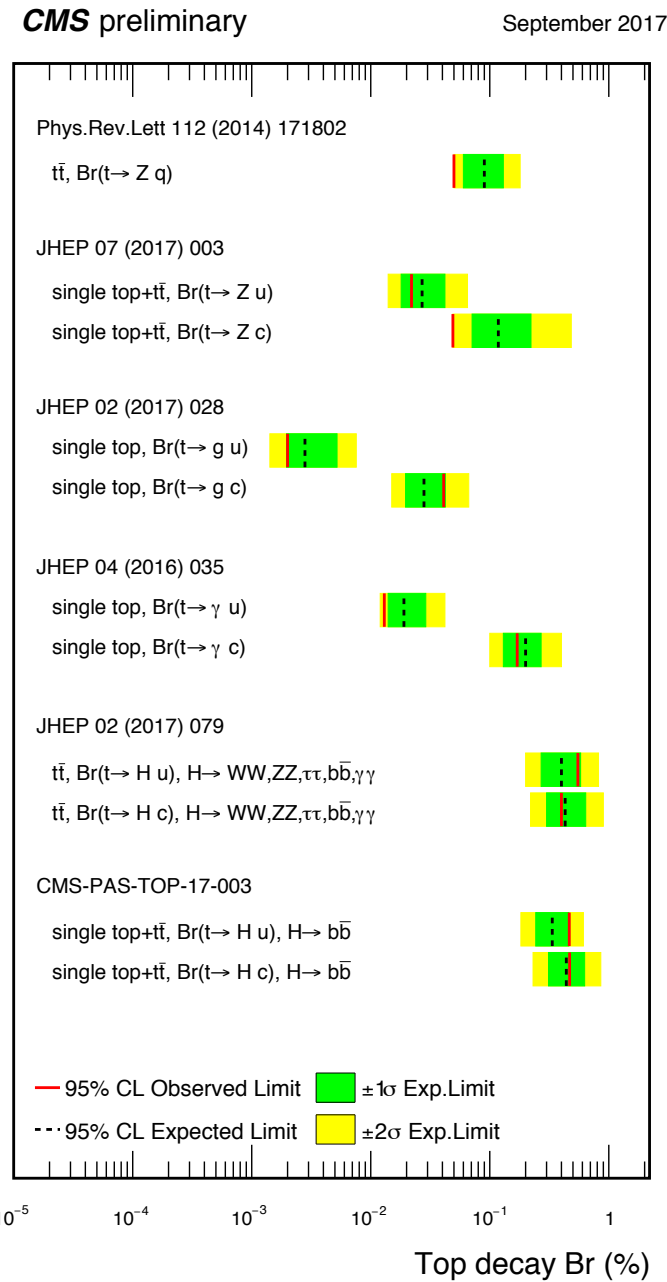


**Figure 1.9:** Summary of the FCNC branching ratios from CMS searches at 8 TeV. Figure taken from [23].

# Experimental set-up

# 2

---

343 A key objective of the Large Hadron Collider (LHC) was the search for the Brout-Englert-Higgs  
 344 boson. The Large Electron Positron (LEP) [48] and Tevatron [49] experiments established  
 345 that the mass of the scalar boson has to be larger than 114 GeV [50, 51], and smaller than  
 346 approximate 1 TeV due to unitarity and perturbativity constraints [52]. On top of this, the  
 347 search for new physics such as supersymmetry or the understanding of dark matter were part  
 348 of the motivation for building the LHC. Since the start of its operation, the LHC is pushing the  
 349 boundaries of the Standard Model, putting the most stringent limits on physics beyond the  
 350 Standard Model as well as precision measurements of the parameters of the Standard Model. A  
 351 milestone of the LHC is the discovery the scalar boson in 2012 by the two largest experiments  
 352 at the LHC [10, 11].

353 This chapter is dedicated to the experimental set up of the LHC and the Compact Muon  
 354 Solenoid (CMS) experiment. Section 2.1 describes the LHC and its acceleration process for  
 355 protons to reach their design energies. The CMS experiment and its components are presented  
 356 in Section 2.2. The upgrades performed during the long shutdown in 2013 are discussed  
 357 in Section 2.2.4. The data acquisition of CMS is presented in Section 2.2.3, while the CMS  
 358 computing model is shown in Section 2.2.5.

## 359 2.1 The Large Hadron Collider

360 The LHC has started its era of cutting edge science on 10 September 2008 [53] after approval by  
 361 the European Organisation of Nuclear Research (CERN) in 1995 [54]. Installed in the previous  
 362 LEP tunnel, the LHC consists of a 26.7 km quasi ring, that is installed between 45 and 170 m  
 363 under the French-Swiss border amidst Cessy (France) and Meyrin (Switzerland). Built to study  
 364 rare physics phenomena at high energies, the LHC can accelerate mainly two types of particles,  
 365 protons and lead ions  $Pb^{45+}$ , and provides collisions at four interaction points, where the particle  
 366 bunches are crossing. Experiments for studying the collisions are installed at each interaction  
 367 point.

368 As can be seen in Figure 2.1, the LHC is the last element in a chain that creates, injects and  
 369 accelerates protons. The starting point is the ionisation of hydrogen, creating protons that are  
 370 injected in a linear accelerator (LINAC 2). Here, the protons obtain an energy of 50 MeV. They

371 continue to the Proton Synchrotron Booster (PSB or Booster), where the packs of protons are  
 372 accelerated to 1.4 GeV and each pack is split up in twelve bunches with 25 or 50 ns spacing.  
 373 The Proton Synchrotron (PS) then increases their energy to 25 GeV before the Super Proton  
 374 Synchrotron (SPS) increases the proton energy up to 450 GeV. Each accelerator ring expands in  
 375 radius in order to reduce the energy loss of the protons by synchrotron radiation<sup>1</sup>. Furthermore,  
 376 the magnets responsible for the bending of the proton trajectories have to be strong enough  
 377 to sustain the higher proton energy. Ultimately, the proton bunches are injected into opposite  
 378 directions into the LHC, where they are accelerated to 3.5 TeV (in 2010 and 2011), 4 TeV (in  
 2012 and 2013) or 6.5 TeV (in 2015 and 2016) [55].

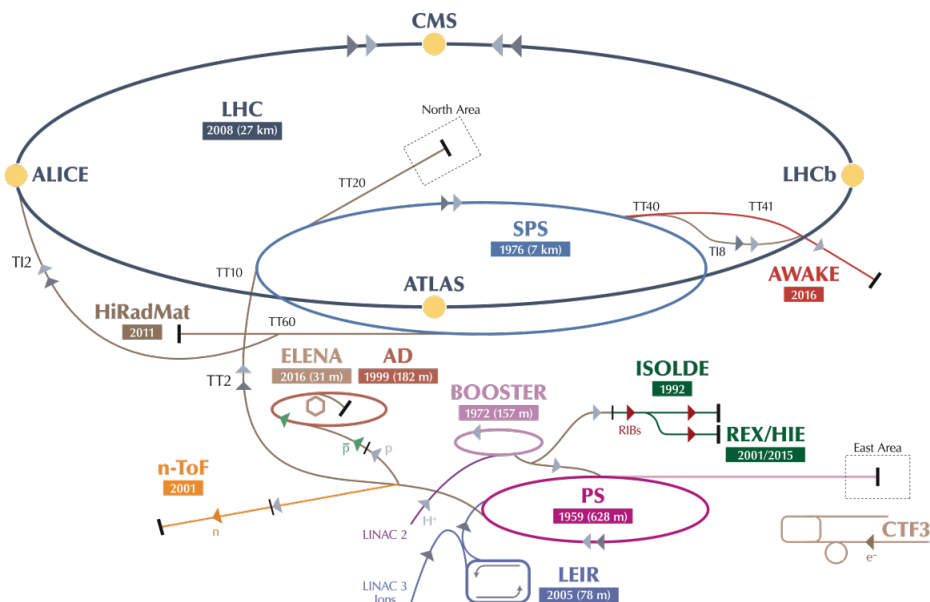


**Figure 2.1:** Schematic representation of the accelerator complex at CERN [56]. The LHC (dark blue) is the last element in chain of accelerators. Protons are successively accelerated by LINAC 2, the Booster, the Proton Synchrotron (PS) and the Super Proton Synchrotron (SPS) before entering the LHC.

379

380 In Figure 2.2 the LHC programme is shown. the first data collisions, so-called Run 1 period,  
 381 lasted from 2008 until 16 February 2013 after which the CERN accelerator complex shut down  
 382 for two years of planned maintenance and consolidation during so-called long shutdown 1  
 383 (LS1). On 23 March 2015, the new data taking period known as Run 2 started. With a brief  
 384 end of the year extended technical stop (EYETS). The main activities carried out during the  
 385 EYETS were the maintenance of many system such as the cryogenics, the cooling, electrical  
 386 systems, etc.; the replacement of magnet, as well as a de-cabling and cabling campaign on  
 387 the SPS. Run 2 will last until July 2018 when the long shut down 2 (LS2) will begin for 2  
 388 years. The main goal of this shutdown is the LHC injectors upgrade (LUI), but also maintenance  
 389 and consolidation will be performed. Furthermore, preparations for the High Luminosity LHC,

<sup>1</sup>This energy loss is proportional to the fourth power of the proton energy and inversely proportional to the bending radius.

390 which will start in 2024, will be done. More information about phase 1 upgrades during LS1  
 391 and EYETS is given in [Section 2.2.4](#).

392 Before the start of the LHC in 2010, the previous energy record was held by the Tevatron collider  
 393 at Fermilab, colliding proton with antiprotons at  $\sqrt{s} = 1.96$  TeV. When completely filled, the  
 LHC nominally contains 2220 bunches in Run 2, compared to 1380 in Run 1 (design: 2200).

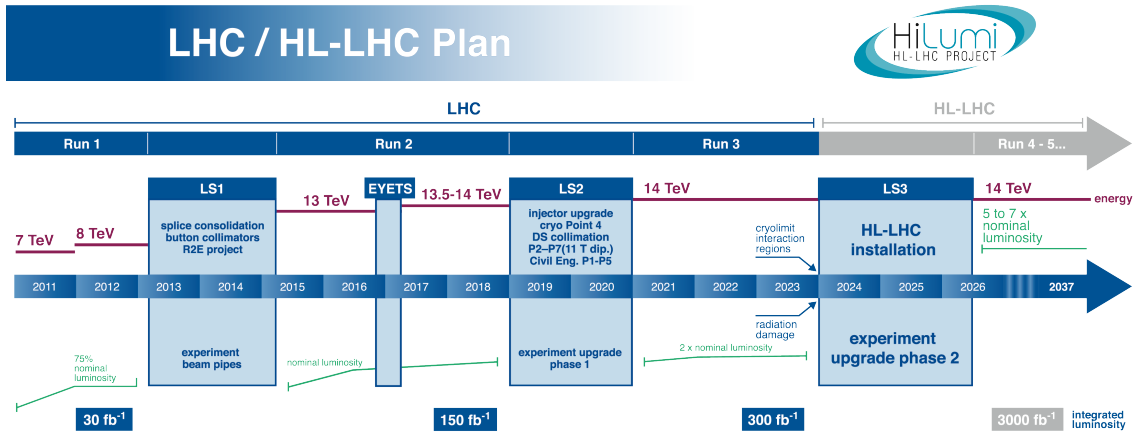


**Figure 2.2:** The HL-LHC timeline. Figure taken from [57].

394

395 Inside the LHC ring [58], the protons are accelerated by the means of radio frequency cavities,  
 396 while 1232 dipole magnets of approximately 15 m long, each weighing 35 t ensure the deflection  
 397 of the beams. The two proton beams circulate in opposite direction in separate pipes inside of  
 398 the magnet. Through the use of a strong electric current in the coils of the magnet, magnetic  
 399 fields are generated and cause the protons to bend in the required orbits. In order for the coil  
 400 to become superconducting and able to produce a strong magnetic field of 8.3 T, the magnet  
 401 structure is surrounded by a vessel. This vessel is filled with liquid Helium making it possible  
 402 to cool down the magnet to 1.9 K. In order to get more focussed and stabilised proton beams,  
 403 additional higher-order multipole and corrector magnets are placed along the LHC beam line.

404 The LHC is home to seven experiments, each located at an interaction point:

- 405 • A Toroidal LHC ApparatuS (ATLAS) [59] and the Compact Muon Solenoid (CMS) [60]  
 406 experiments are the two general purpose detectors at the LHC. They both have a hermetic,  
 407 cylindrical structure and were designed to search for new physics phenomena along with  
 408 precision measurements of the Standard Model. The existence of two distinct experiments  
 409 allows cross-confirmation of any discovery.
- 410 • A Large Ion Collider Experiment (ALICE) [61] and the LHC Beauty (LHCb) [62] experi-  
 411 ments are focusing on specific phenomena. ALICE studies strongly interacting matter  
 412 at extreme energy densities where a quark-gluon plasma forms in heavy ion collisions  
 (Pb-Pb or p-Pb). LHCb searches for differences between matter and antimatter with the  
 413 focus on b physics..

- The forward LHC (LHCf) [63] and the TOTal cross section, Elastic scattering and diffraction dissociation Measurement (TOTEM) [64] experiments are two smaller experiments that focus on head on collisions. LHCf consists of two parts placed before and after ATLAS and studies particles created at very small angles. TOTEM is placed in the same cavern as CMS and measures the total proton-proton cross section and studies elastic and diffractive scattering.
- The Monopoles and Exotics Detector At the LHC (MoEDAL) [65] experiment is situated near LHCb and tries to find magnetic monopoles.

For the enhancement of the exploration of rare events and thus enhancing the number of collisions, high beam energies as well as high beam intensities are required. The luminosity [66] is a measurement of the number of collisions that can be produced in a detector per square meter and per second and is the key role player in this enhancement. The LHC collisions create a number of events per second given by

$$N_{\text{event}} = L\sigma_{\text{event}}, \quad (2.1)$$

where  $\sigma_{\text{event}}$  is the cross section of the process of interest and  $L$  the machine instantaneous luminosity. This luminosity depends only on the beam parameters and is for a Gaussian beam expressed as

$$L = \frac{1}{4\pi} N_b n_b f_{\text{rev}} \frac{N_b}{\epsilon_n} \left( 1 + \left( \frac{\theta_c \sigma_z}{2\sigma^*} \right)^2 \right)^{-\frac{1}{2}} \frac{\gamma_r}{\beta^*}. \quad (2.2)$$

The number of particles per bunch is expressed by  $N_b$ , while  $n_b$  is the number of bunches per beam,  $f_{\text{rev}}$  the revolution frequency,  $\gamma_r$  the relativistic gamma factor,  $\epsilon_n$  the normalized transverse beam emittance - a quality for the confinement of the beam,  $\beta^*$  the beta function at the collision point - a measurement for the width of the beam,  $\theta_c$  the angle between two beams at the interaction point,  $\sigma_z$  the mean length of one bunch, and  $\sigma^*$  the mean height of one bunch. In Equation 2.2, the blue part represents the stream of particles, the red part the brilliance, and the green part the geometric reduction factor due to the crossing angle at the interaction point.

The peak design luminosity for the LHC is  $10^{34} \text{ cm}^{-2}\text{s}^{-1}$ , which leads to about 1 billion proton interactions per second. In 2016, the LHC was around 10% above this design luminosity [67]. The luminosity is not a constant in time since it diminishes due to collisions between the beams, and the interaction of the protons and the particle gas that is trapped in the centre of the vacuum tubes due to the magnetic field. The diffusion of the beam degrades the emittance and therefore also the luminosity. For this reason, the mean lifetime of a beam inside the LHC is around 15 h. The integrated luminosity - the luminosity provided in a certain time range - recorded by CMS and ATLAS over the year 2016 is given in Figure 2.3. In Run 2, the peak luminosity is  $13\text{-}17 \times 10^{33} \text{ cm}^{-2}\text{s}^{-1}$  compared to  $7.7 \times 10^{33} \text{ cm}^{-2}\text{s}^{-1}$  in Run 1. The recorded luminosity is validated for physics analysis keeping  $35.9 \text{ fb}^{-1}$  during 2016 data taking.

Multiple proton-proton interactions can occur during one bunch crossing, referred to as pileup. On average, the number of pileup events is proportional to the luminosity times the total inelastic proton-proton cross section. In 2016, an average of about 27 of pileup interactions has been observed in 13 TeV proton collisions at the interaction point of CMS. For 2012, this number was about 21 pileup interactions for 8 TeV collisions.

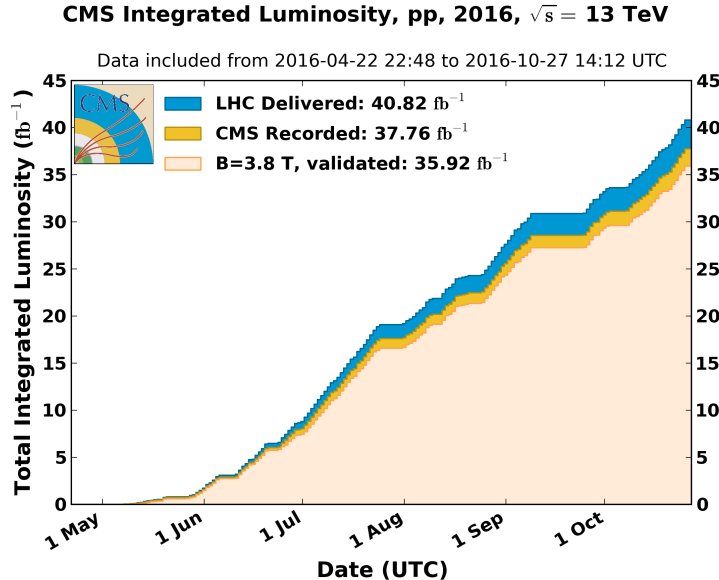


**Figure 2.3:** Cumulative off-line luminosity measured versus day delivered by the LHC (blue), and recorded by CMS (orange), and certified as good physics analysis during stable beams (light orange) during stable beams and for proton collisions at 13 TeV centre-of-mass energy in 2016. [68].

## 445 2.2 The Compact Muon Solenoid

446 At one of the collision points of the LHC, the CMS detector [69–71] is placed. Weighing 14 000 t,  
447 this cylindrical detector is about 28.7 m long and 15 m in diameter. It has an onion like structure  
448 of several specialised detectors and contains a superconducting solenoid with a magnetic field of  
449 3.8 T. Living in a hadronic environment, multi-jet processes produced by the strong interaction  
450 are the main source of background for rare physics processes. Therefore, good identification,  
451 momentum resolution, and charge determination of muons, electrons and photons are one of  
452 the main goals of the CMS detector. Additionally, a good charged particle momentum resolution  
453 and reconstruction efficiency in the inner tracker provides identification for jets coming from b  
454 quarks or tau particles. Also the electromagnetic resolution for an efficient photon and lepton  
455 isolation as well as a good hadronic calorimeter for the missing transverse energy<sup>2</sup> were kept  
456 into account while designing CMS. In Figure 2.4, an overview of the CMS detector is shown.

### 457 2.2.1 CMS coordinate system

The coordinate system used by CMS can be found in Figure 2.5. The origin of the right handed orthogonal coordinate system is chosen to be the point of collisions. The x-axis points towards the centre of the LHC ring such that the y-axis points towards the sky, and the z-axis lies tangent to the beam axis. Since the experiment has a cylindrical shape, customary coordinates are used to describe the momentum  $\vec{p}$ : the distance  $p = |\vec{p}|$ , the azimuthal angle<sup>3</sup>  $\phi \in [-\pi, \pi]$ , the

<sup>2</sup>The missing transverse energy comes from an imbalance in the transverse plane. This will be discussed in Chapter 4.

<sup>3</sup>The azimuthal angle is the angle between the x-axis and the projection in the transverse plane of the momentum  $\vec{p}$ , denoted as  $\vec{p}_T$ .

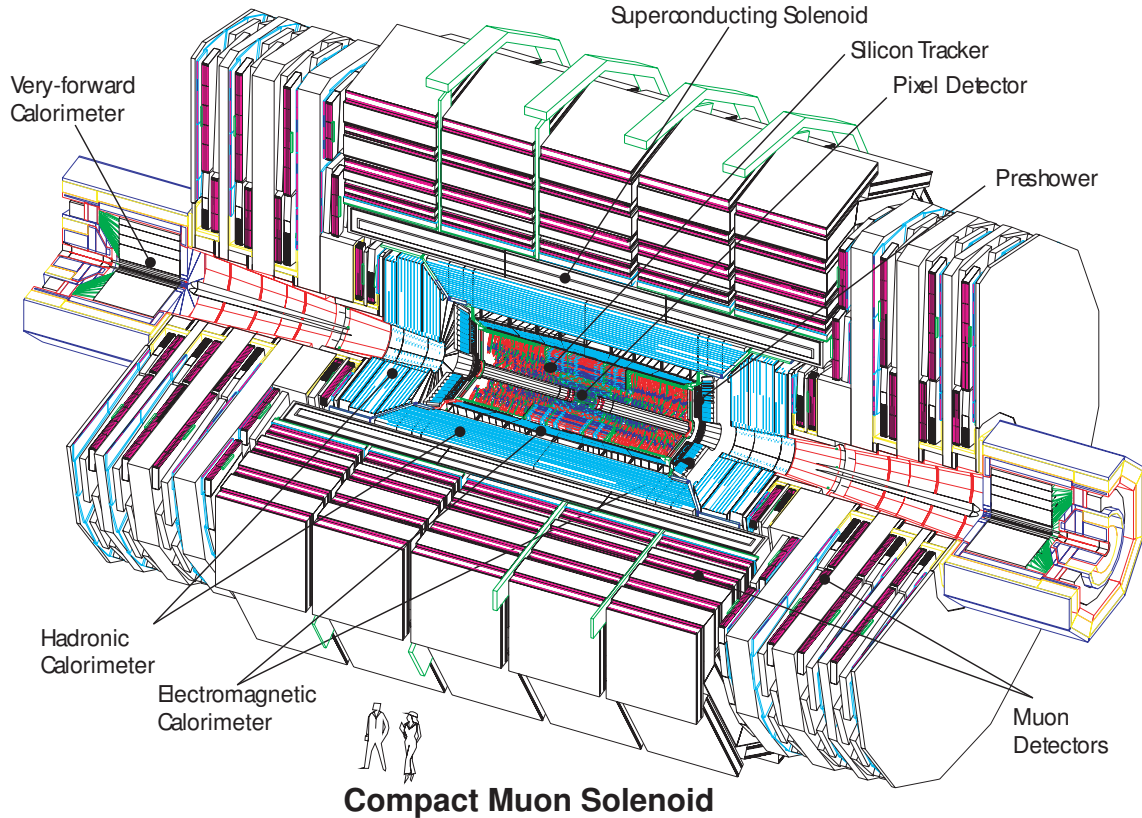


**Figure 2.4:** Mechanical layout of the CMS detector. Figure taken from [72].

pseudo-rapidity<sup>4</sup>  $\eta$  :

$$\eta = -\ln \left( \tan \left( \frac{\theta}{2} \right) \right). \quad (2.3)$$

For the energies considered at the LHC, where  $E \gg m$ , the pseudo-rapidity is a good approximation of the rapidity  $y$

$$y = \frac{1}{2} \ln \left( \frac{E + p_z}{E - p_z} \right), \quad (2.4)$$

458 where the difference of rapidities of two particles is invariant under a Lorentz boost in the  
459 z-direction.

### 460 2.2.2 Towards the heart of CMS

461 The CMS detector can be divided into two parts. A central barrel is placed around the beam  
462 pipe ( $|\eta| < 1.4$ ), and two plugs (endcaps) ensure the hermeticity of the detector. In [Figure 2.4](#)  
463 and [Figure 2.6](#) the onion like structure of the CMS detector is visible. The choice of a solenoid of  
464 12.9 m long and 5.9 m diameter gives the advantage of bending the particle trajectories in the

---

<sup>4</sup>The pseudo rapidity is expressed by the polar angle  $\theta$  between the direction of  $\vec{p}$  and the beam.

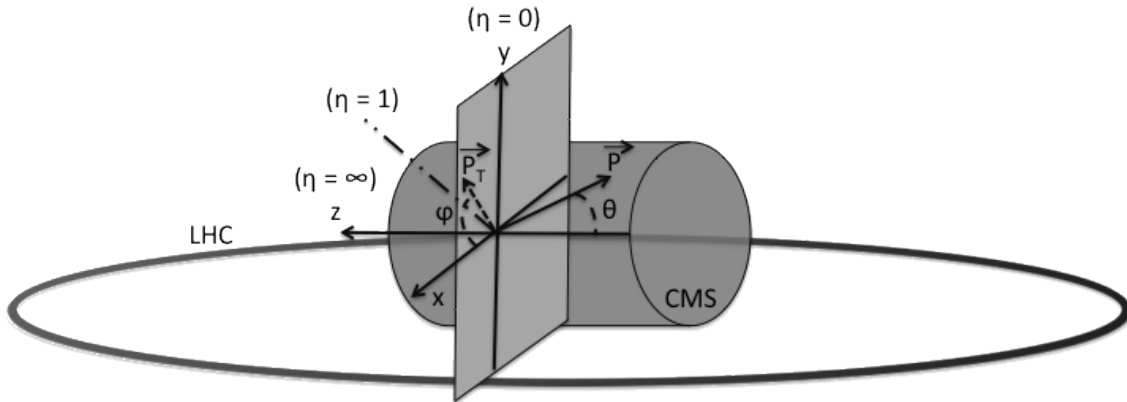


**Figure 2.5:** Representation of the coordinate system used by CMS. The point of origin is put at the collision point. The x-axis points towards the centre of the LHC ring such that the z-axis lies tangent to the beam axis.

465 transverse plane. The hadronic calorimeter (Section 2.2.2.3), the electromagnetic calorimeter  
 466 (Section 2.2.2.4) and the tracker (Section 2.2.2.5) are within the solenoid (Section 2.2.2),  
 467 while the muon chambers (Section 2.2.2.1) are placed outside the solenoid. The data used for  
 468 the search presented in this thesis is collected after the long shutdown 1. After discussing each  
 469 part of CMS in their Run 1 configuration, Section 2.2.4 elaborates on their different upgrades  
 470 for the data collected in Run 2.

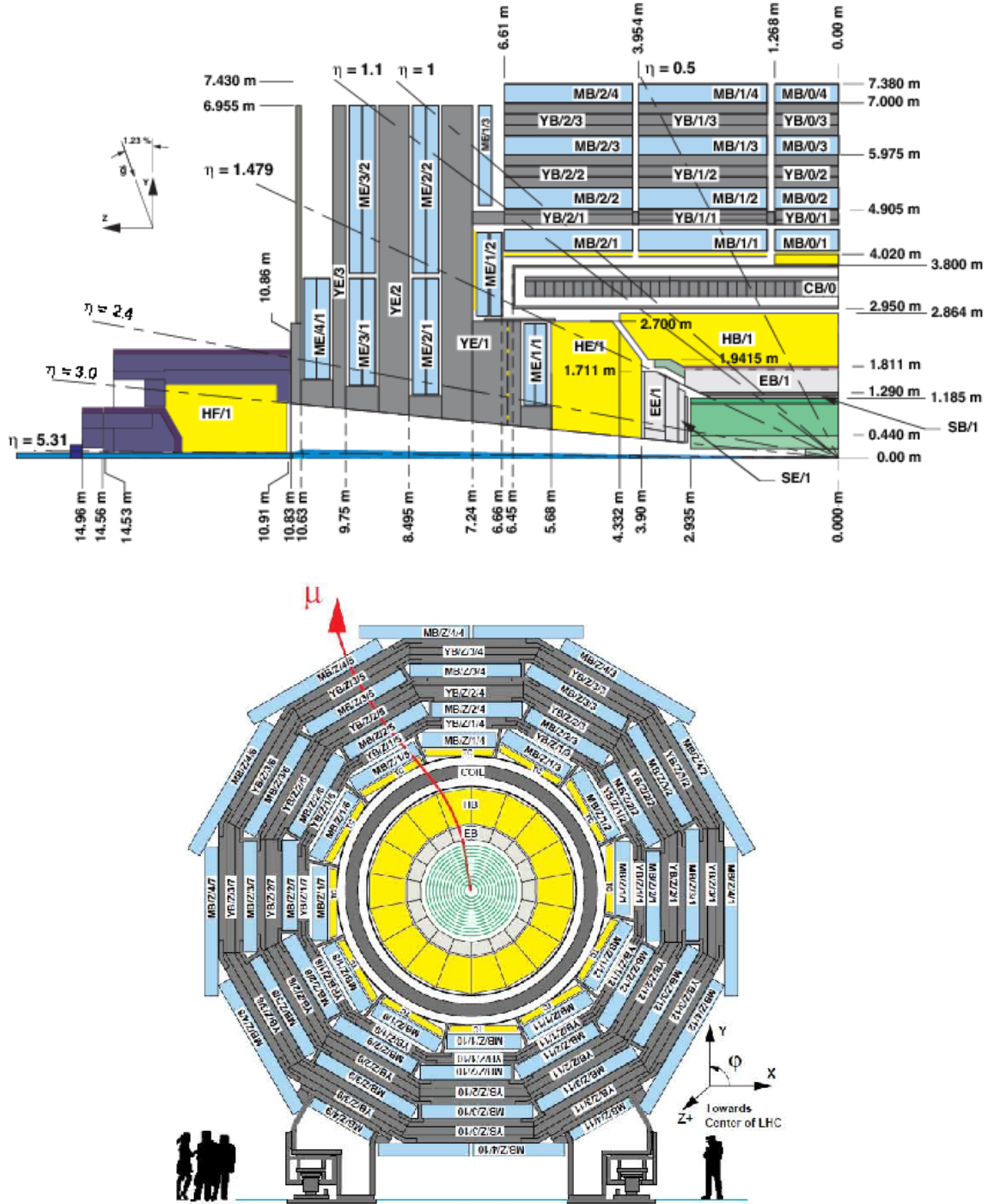


**Figure 2.6:** Schematic view of the CMS detector in the Run 1 configuration. The longitudinal view of one quarter of the detector is given at the top, while the transversal view is shown at the bottom. The muon system barrel elements are denoted as MBZ/N/S, where Z= -2... +2 is the barrel wheel number, N= 1...4 the station number and S= 1...12 the sector number. Similarly, the steel return yokes are denoted as YBZ/N/S. The solenoid is denoted as CB0, while the hadronic calorimeter is denoted as HE (endcap)/ HB (barrel)/HF (forward) and the electromagnetic calorimeter as EE (endcap)/EB (barrel). The green part represents the tracking system (tracker + pixel). Figure taken from [73].

471 **2.2.2.1 Muon system**

472 The outermost part of CMS consists of the muon system. The magnet return yoke is interleaved  
 473 with gaseous detector chambers for muon identification and momentum measurement. The  
 474 barrel contains muon stations arranged in five separate iron wheels, while in the endcap four  
 475 muon stations are mounted onto three independent iron discs on each side. Each barrel wheel  
 476 has 12 sectors in the azimuthal angle.

477 The muon system is divided into three parts, shown in [Figure 2.7](#). The muon rate and neutron  
 478 induced backgrounds are small and the magnetic field is very low for the barrel, thus CMS can  
 479 use drift tube (DT) chambers. For the endcaps however, the muon and background flux is much  
 480 higher and there is a need to use cathode strip chambers (CSC) which are able to provide a  
 481 faster response, higher granularity and have a better resistance against radiation. In order to  
 482 form a redundant trigger system, resistive plate chambers (RPC) are added. This makes a total  
 483 of 250 DT, 540 CSC and 610 RPC chambers. In [Figure 2.6](#) the arrangement is shown.

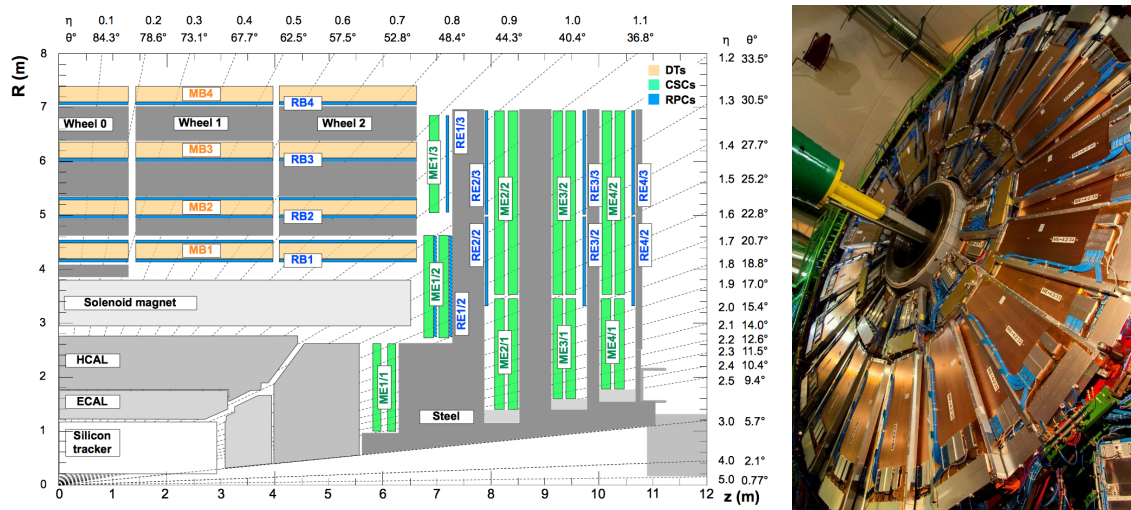


**Figure 2.7:** (Left) Schematic view of one quarter of the CMS muon system in the Run 1 configuration. The cathode strip chambers (CSC) are shown in green, the drift tubes (DT) are shown in yellow, while the resistive plate chambers (RPC) are shown in blue. Figure taken from [73]. (Right) Cathode strip chambers (ME+4/2 chambers on YE+3). Photo taken from [74].

483

484 Providing a measurement for  $|\eta| < 1.2$ , the DT chambers in the barrel are on average  
 485  $2 \times 2.5 \text{ m}^2$  in size and consist of 12 layers of DT cells<sup>5</sup> arranged in three groups of four. The  
 486  $r\phi$  coordinate is provided by the two outside groups, while the middle group measures the  
 487  $z$  coordinate. For the outer muon station, the DT chambers contain only 8 layers of DT cells,  
 488 providing a muon position in the  $r\phi$  plane. There are four CSC stations in each endcap, providing  
 489 muon measurements for  $0.9 < |\eta| < 2.4$  (Run 1 configuration). These CSCs are multi-wired  
 490 proportional chambers that consist of 6 anode wire planes crossed by 7 copper strips cathode  
 491 panels in a gas volume. The  $r$  coordinate is provided by the copper strips, while the  $\phi$  coordinate  
 492 comes from the anode wires, giving a two dimensional position measurement. There are six

<sup>5</sup>The DT cells are 4 cm wide gas tubes with positively charged stretched wires inside.

493 layers of RPCs in the barrel muon system and one layer into each of the first three stations  
 494 of the endcap. They are made from two high resistive plastic plates with an applied voltage  
 495 and separated by a gas volume. Read out strips mounted on top of the plastic plates detect the  
 496 signal generated by a muon passing through the gas volume. The RPCs provide a fast response  
 497 with a time resolution of 1 ns and cover a range of  $|\eta| < 1.8$  for the Run 1 configuration.

498 The muon system provides triggering on muons, identifying muons and improves the momen-  
 499 tum measurement and charge determination of high  $p_T$  muons. On top of the muon system,  
 500 a fraction of the muon energy is deposited in the electromagnetic calorimeter, the hadronic  
 501 calorimeter, and outer calorimeter. The high magnetic field enables an efficient first level trigger  
 502 and allows a good momentum resolution of  $\Delta p/p \approx 1\%$  for a  $p_T$  of 100 GeV and  $\approx 10\%$  for a  
 $p_T$  of 1 TeV. There is an efficient muon measurement up to  $|\eta| < 2.4$ .

**NOTE:** 503  
check num-  
bers for Run  
2 504

### 2.2.2.2 Solenoid

505 Making use of the knowledge of previous experiments like ALEPH and DELPHI at LEP and H1  
 506 at HERA, CMS choose for a large super conducting solenoid with a length of 12.9 m and a  
 507 inner bore of 5.9 m [71]. With 2 168 turns, a current of 18.5 kA resulting in a magnetic field of  
 508 3.8 T, and a total energy of 2.7 GJ, a large bending power can be obtained for a modestly-sized  
 509 solenoid. In order to ensure a good momentum resolution in the forward regions, a favourable  
 510 length/radius was necessary. In [Figure 2.8](#), a photo of the CMS solenoid is shown.

511 The solenoid uses a high-purity aluminium stabilised conductor with indirect cooling from  
 512 liquid helium, together with fully epoxy impregnation. A four-layer winding is implemented that  
 513 can withstand an outward pressure of 64 atm. The NbTi cable is co-extruded by pure aluminium  
 514 that acts as a thermal stabilizer and has an aluminium alloy for mechanical reinforcement. The  
 515 return of the magnetic field is done by five wheels, noted by YB in [Figure 2.6](#).

### 516 2.2.2.3 Hadronic calorimeter

517 The hadronic calorimeter (HCAL) is dedicated to precisely measure the energy of charged and  
 518 neutral hadrons via a succession of absorbers and scintillators. This makes it crucial for physics  
 519 analyses with hadronic jets or missing transverse energy. The HCAL barrel extends between  
 520  $1.77 < r < 2.95$  m, where  $r$  is the radius in the transverse plane with respect to the beam. Due  
 521 to space limitations, the HCAL needs to be as small as possible and is made from materials  
 522 with short interaction lengths<sup>6</sup>. On top of this, the HCAL should be as hermetic as possible and  
 523 extend to large absolute pseudo rapidities such that it can prove a good measurement of the  
 524 missing transverse energy.

525 The quality of the energy measurements is dependent on the fraction of the hadronic shower  
 526 that can be detected. Therefore, the HCAL barrel (HB) inside the solenoid is reinforced by an  
 527 outer hadronic calorimeter between the solenoid and muon detectors (HO, see [Figure 2.9](#)), using  
 528 the solenoid as extra absorber. This increases the thickness to 12 interaction lengths. The HB

<sup>6</sup>Here the interaction length is the nuclear interaction length and this is the length needed for absorbing 36.7% of the relativistic charged particles. For the electromagnetic calorimeter this is defined in radiation length  $X_0$ . The radiation length is the mean distance over which a high energy electron loses all but  $1/e$  of its energy by bremsstrahlung.

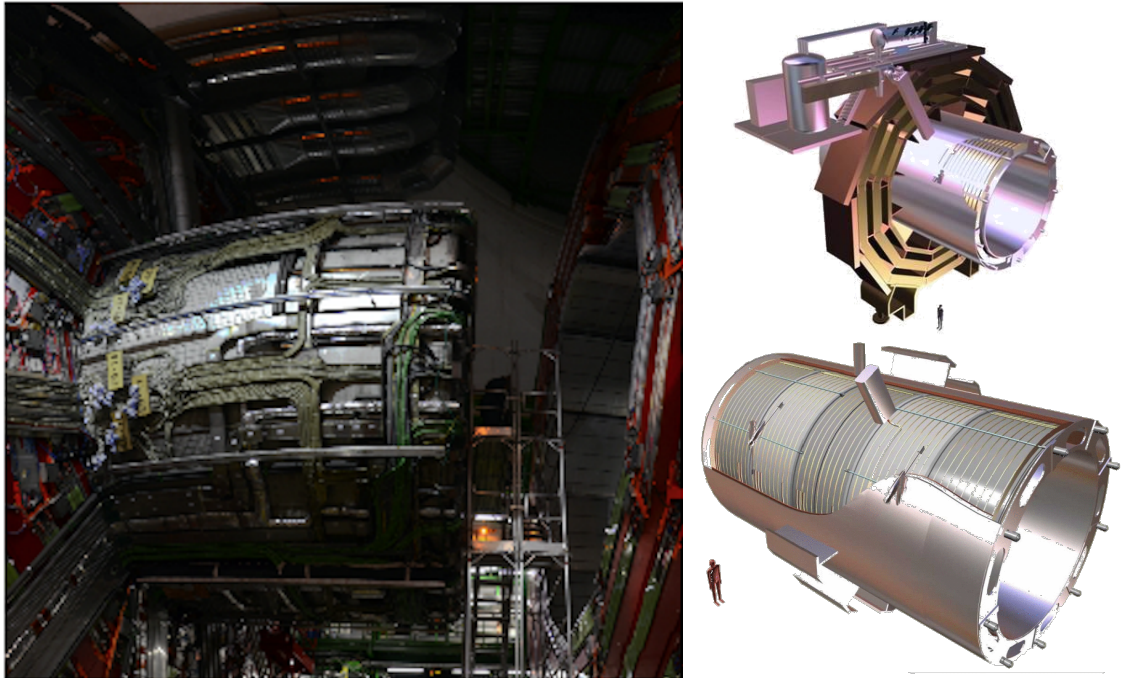


**Figure 2.8:** (Left) CMS solenoid during the long shutdown in 2013. (Right) An impression of the solenoid magnet taken from [75].

529 and HO provide measurements for  $|\eta| < 1.3$ , while an endcap on each side (HE,  $1.3 < |\eta| < 3$ )  
 530 and a forward calorimeter (HF,  $3.0 < |\eta| < 5.2$ ) extend the pseudo rapidity range.

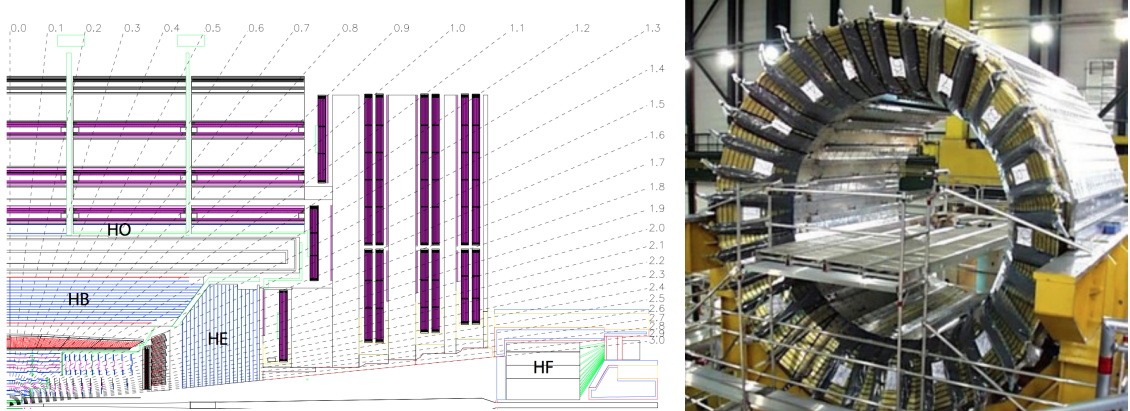


**Figure 2.9:** (Left) Longitudinal view of the CMS detector showing the locations of the HB, HE, HO, and HF calorimeters. Figure taken from [60]. (Right) CMS barrel calorimeter. Photo taken from [76].

531 The HB is made of 16 absorber plates where most of them are built from brass and others are  
 532 made from stainless steel and is about five to ten interaction lengths thick. It is divided in  $\eta \times \phi$   
 533 towers and contains 2592 read out channels. The HO complements the HB and extends the  
 534 reach up to twelve interaction lengths. This subsystem contains 2160 read out channels. The HE  
 535 is also composed of brass absorber plates and has a thickness corresponding to approximately

ten interaction lengths, with 2592 read out channels.. The HF experiences intense particle fluxes with an expected energy of 760 GeV deposited on average in a proton interaction at a centre-of-mass of 14 TeV, compared to 100 GeV in the rest of the detector. Therefore, these are Cherenkov light detectors made of radiation hard quartz fibres. The main causes of such large energy events are high energy muons and charged particles from late showering hadrons. During Run 1, it became clear that the glass windows of the photon multiplier tubes (PMTs) had to be replaced which was done during LS1 [77]. The HF represents 1728 read out channels.

The HCAL and electromagnetic calorimeter combined can measure the hadron energy with a resolution  $\Delta E/E \approx 100\% \sqrt{E[\text{GeV}]} + 5\%$ .

#### 2.2.2.4 Electromagnetic calorimeter

The electromagnetic calorimeter (ECAL) is designed to measure the energy of photons and electrons and covers  $|\eta| < 3$ . It is an hermetic, homogeneous detector and consists of 75 848 lead tungstate ( $\text{PbWO}_4$ ) crystals. These crystals have a fast response time - 80% of the light is emitted within 25 ns - and are radiation hard. The electromagnetic showers produced by passing electrons or photons ionize the crystal atoms which emit a blue-green scintillation light, that is collected by silicon avalanche photodiodes (APDs) in the barrel and vacuum phototriodes (VPTs) in the endcaps. The crystals and the APD response is sensitive to temperature changes and require a stable temperature.

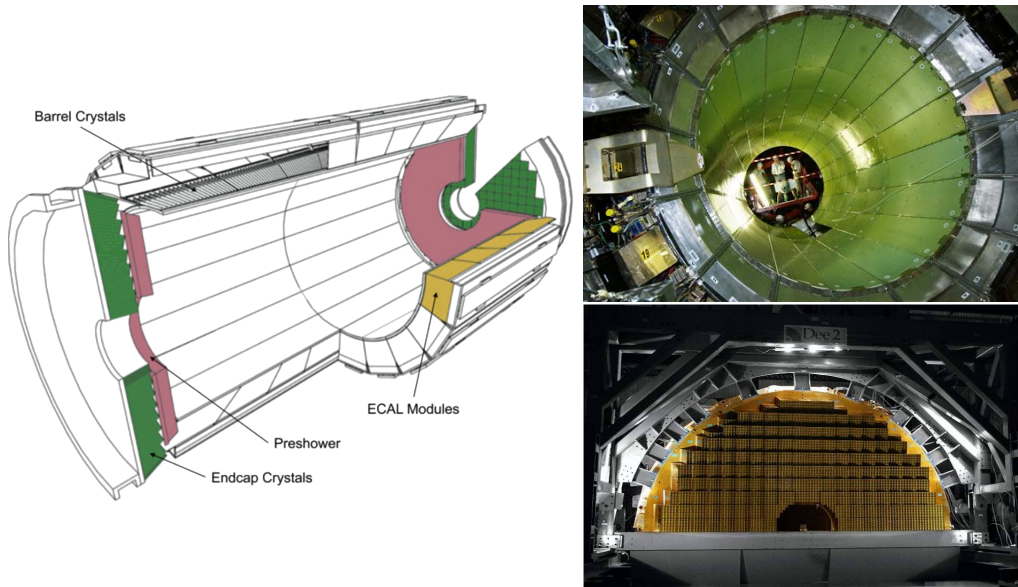


**Figure 2.10:** (Left) Schematic cross section of the electromagnetic calorimeter taken from [60]. (Right top) The ECAL barrel during construction [78]. (Right bottom) One half of an EE [79].

There are three parts: a central barrel (EB), an endcap region (EE) and a preshower (ES) (Figure 2.10). The EB has an inner radius of 129 cm and corresponds to a pseudo rapidity of  $0 < |\eta| < 1.479$ . At a distance of 314 cm from the vertex and covering a pseudo rapidity of  $1.479 < |\eta| < 3.0$ , are the EE. They consist of semi-circular aluminium plates from which structural units of  $5 \times 5$  crystals (super crystals) are supported. The ES is placed in front of

559 the crystal calorimeter over the endcap pseudo rapidity range with two planes of silicon strip  
 560 detectors as active elements.

The electromagnetic shower will typically involve more than one channel. More than 90% of the energy of a 35 GeV electron or photon is contained in a  $5 \times 5$  matrix of crystals. Therefore, a clustering algorithm is performed in order to associate the energy deposits to the particles impinging the calorimeter. The achieved precision [80] for the barrel is  $2 \times 10^{-3}$  rad in  $\phi$  and  $10^{-3}$  in  $\eta$ . For the endcaps this is  $5 \times 10^{-3}$  rad in  $\phi$  and  $2 \times 10^{-3}$  in  $\eta$ . The energy is reconstructed by a supercluster algorithm, taking into account energy radiated via bremsstrahlung or conversion [60]. The energy resolution is given by

$$\frac{\sigma(E)}{E} = \frac{2.8\%}{\sqrt{E}} \oplus \frac{0.128}{E(\text{GeV})} \oplus 0.3\%, \quad (2.5)$$

561 in the absence of a magnetic field, where the contributions come from the stochastic, noise and  
 562 constant terms respectively. The dominating term is the constant term ( $E_{\text{shower}} \approx 100$  GeV)  
 563 and thus the performance is highly dependent on the quality of calibration and monitoring .

#### 564 2.2.2.5 Inner tracking system and operations

565 The tracking system (tracker) [81] is the detecting unit closest to the point of interaction.  
 566 Responsible for the reconstruction of trajectories from charged particles with  $|\eta| < 2.5$  that  
 567 are bent by the magnetic field, it provides a measurement of the momentum. The tracker is  
 568 also responsible for the determination of the interaction point or vertex. It should be able to  
 569 provide high granularity as well as fast read out, and be able to endure high radiation. For these  
 570 reasons, the CMS collaboration choose silicon detector technology.

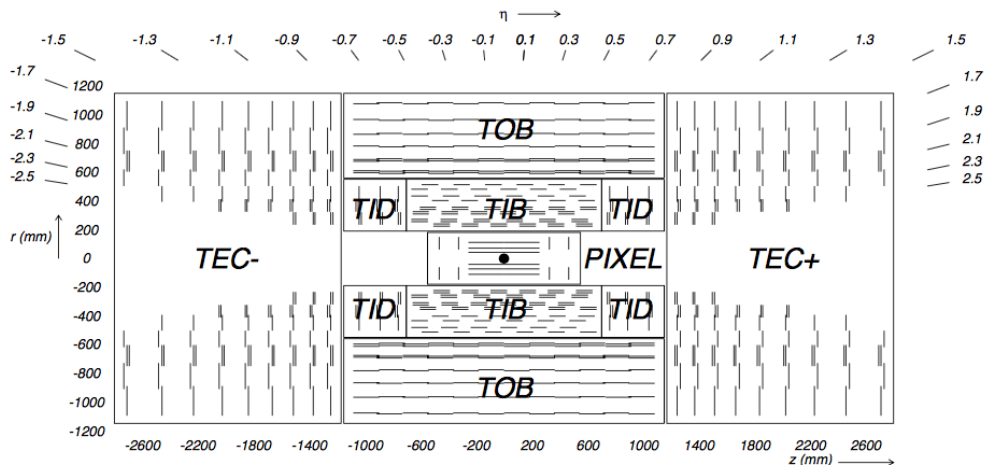


**Figure 2.11:** Schematic cross section through the CMS tracker. Each line represents a detector module. Double lines indicate back-to-back modules that deliver stereo hits. Figure taken from [60].

571 The tracking system consists of a cylinder of 5.8 m long and 2.5 m in diameter. It is immersed  
 572 in a co-axial magnetic field of 3.8 T provided by the solenoid. As shown in Figure 2.11, the  
 573 tracker is built up from a large silicon strip tracker with a small silicon pixel tracker inside. The

574 inner pixel region ( $4.4 < r < 10.2$  cm), gets the highest flux of particles. Therefore, pixel silicon  
 575 sensors of  $100 \times 150 \mu\text{m}^2$  are used. It consists of three cylindrical barrels that are complemented  
 576 by two discs of pixel modules at each side. The silicon strip tracker ( $20 < r < 116$  cm) has three  
 577 subdivisions. The Tracker Inner Barrel and Discs (TIB, TID, see [Figure 2.13](#)) are composed  
 578 of four barrel layers accompanied by three discs at each end. The outer part of the tracker -  
 579 Tracker Outer Barrel (TOB) - consists of 6 barrel layers. In the outer discs, there are nine discs  
 580 of silicon sensors, referred to as Tracker End Caps (TEC).

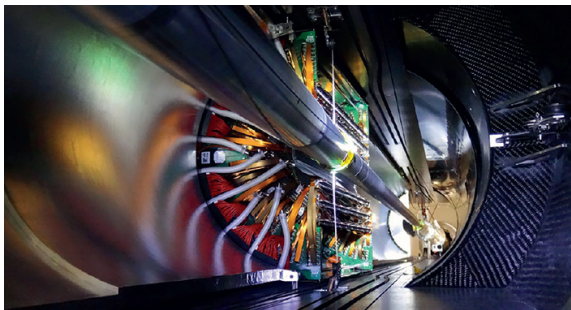


**Figure 2.12:** The pixel barrel being re-installed after the Long Shutdown in 2015, around the beam pipe at CMS [82].



**Figure 2.13:** First half of the inner tracker barrel, consisting of three layers of silicon modules [83].

581 The pixel detector, shown in [Figure 2.12](#), has 1440 modules that cover an area of about  $1 \text{ m}^2$   
 582 and have 66 million pixels. It provides a three-dimensional position measurement of the hits  
 583 arising from the interaction from charged particles with the sensors. In transverse coordinate  
 584 ( $r\phi$ ), the hit position resolution is about  $10 \mu\text{m}$ , while  $20\text{-}40 \mu\text{m}$  is obtained in the longitudinal  
 585 coordinate ( $z$ ). The sensor plane position provides the third coordinate. The TIB/TID, shown in  
 586 [Figure 2.13](#), delivers up to four  $r\phi$ -measurements using  $320 \mu\text{m}$  thick silicon micro-strip sensors.  
 587 These sensors are placed with their strips parallel to the beam axis in the barrel and radial  
 588 in the discs. In the TIB, the first two layers have a strip pitch of  $80 \mu\text{m}$ , while the remaining  
 589 two have a strip pitch of  $120 \mu\text{m}$ . This leads to a respective single point resolution of  $23 \mu\text{m}$   
 590 and  $35 \mu\text{m}$ . For the TID, the pitch varies between  $100 \mu\text{m}$  and  $141 \mu\text{m}$ . The TOB provides six  
 591  $r\phi$ -measurements with a single point resolutions of  $53 \mu\text{m}$  in the first four layers, and  $35 \mu\text{m}$  in  
 592 the last two layers. It consists of  $500 \mu\text{m}$  thick microstrip sensors with strip pitches of  $183 \mu\text{m}$   
 593 (first 4 layers) or  $122 \mu\text{m}$  (last two layers). The TEC provides up to 9  $\phi$ -measurements via 9  
 594 discs consisting of up to 7 rings of silicon microstrip sensors of  $97 \mu\text{m}$  to  $184 \mu\text{m}$  average pitch.

595 A second co-ordinate measurement ( $z$  in the barrel,  $r$  on the discs) is provided through the  
 596 use of a second micro strip detector module mounted back-to-back with a stereo angle of 100  
 597 mrad. This is done on the modules in the first two layers and rings of the TIB, TID, and TOB, as  
 598 well as rings 1,2, and 5 of the TECs (blue line in [Figure 2.11](#)). The resolution in the  $z$  direction is  
 599 approximately  $230 \mu\text{m}$  in the TIB and  $530 \mu\text{m}$  in the TOB, and is varying with pitch in the TID  
 600 and TEC. To allow overlay and avoid gaps in acceptance, each module is shifted slightly in  $r$  or  
 601  $z$  with respect to its neighbouring modules within a layer. With this detector layout, at least  
 602 nine points per charged particle trajectory can be measured in an  $|\eta|$  range up to 2.4, where at  
 603 least four of them being two dimensional. The CMS silicon tracker provides 9.3 million readout  
 604 channels and covers an active area of about  $198 \text{ m}^2$ .

605 **2.2.3 Data acquisition**

606 At a design luminosity of  $10^{34} \text{ cm}^{-2}\text{s}^{-1}$ , the proton interaction rate exceeds 1 GHz. Given the  
 607 large size of an event (about 1 MB), the high crossing rate, and that typically tens of collisions  
 608 happen at the same time, it is impossible for the CMS experiment to store all the data generated.  
 609 In order to deal with the large amount of data, a two level trigger system has been put in place.  
 610 The first level (Level-1) is a custom hardware system, while a second high level trigger (HLT) is  
 611 software based running on a large farm of computers.

612 **CMS Level-1 Trigger**

613 The Level-1 Trigger has to be a flexible, maintainable system, capable of adapting to the  
 614 evolving physics programme of CMS [84]. Its output rate is restricted to 100 kHz imposed  
 615 by the CMS readout electronics. It is implemented by custom hardware and selects events  
 616 containing candidate objects - e.g. ionization deposits consistent with a muon, or energy clusters  
 617 corresponding to an electron / photon / tau lepton / missing transverse energy / jet. Collisions  
 618 with large momenta can be selected by using scalar sum of the transverse momenta of the jets.

619 By buffering the raw data from the CMS subdetectors in front-end drivers, the Level-1 Trigger  
 620 has a pipeline memory of 3.2  $\mu\text{s}$  to decide whether to keep an event or reject it. The trigger  
 621 primitives (TP) from the calorimeters and muon detectors are processed in several steps and  
 622 combined into a global trigger. This information is then combined with the input from the other  
 623 subsystems for the HLT. The separate inputs are synchronized to each other and the LHC orbit  
 624 clock and sent to the global trigger module. Here, Level-1 Trigger algorithms are performed  
 625 within 1  $\mu\text{s}$  to decide whether to keep the event.

626 **CMS HLT Trigger**

627 The HLT is an array of commercially available computers with a programmable menu that has  
 628 an output rate of on average 400 Hz for off-line event storage. The data processing is based on  
 629 an HLT path. This is a set of algorithmic steps to reconstruct objects to define selection criteria.  
 630 Here, the information of all subdetectors can be used to perform algorithms on higher level  
 631 reconstructed objects.

632 **2.2.4 Phase 1 upgrades**

633 Before the start of taking collision data for 13 TeV operations on 3 June 2015, CMS had a  
 634 long shutdown (LS1) [85]. During this shutdown, the section of the beryllium beam pipe  
 635 within CMS was replaced by a narrower one. This operation required the pixel detector to be  
 636 removed and reinserted into CMS. During Run 2, higher particle fluxes with respect to Run  
 637 1 are expected. To avoid longterm damage caused by the intense particle flux at the heart of  
 638 CMS, the tracker is been made ready to operate at much lower temperature than during Run 1.  
 639 The electromagnetic calorimeter preshower system was damaged during Run 1, therefore the  
 640 preshower discs were removed, repaired and reinstalled successfully inside CMS in 2014. To  
 641 help the discrimination between interesting low momentum muons coming from collisions and  
 642 muons caused by backgrounds, a fourth triggering and measurement station for muons was  
 643 added in each of the endcaps. Several new detectors were installed into CMS for measuring the  
 644 collision rate within the detector and to monitor beam related backgrounds.

645 During the LS1, the muon system underwent major upgrades [86, 87]. In the fourth station  
 646 of each endcap, the outermost rings of CSC and RPC chambers were completed, providing an  
 647 angular coverage of  $1.2 < |\eta| < 1.8$  for Run 2, increasing the system redundancy, and allowing  
 648 tighter cuts on the trigger quality. In order to reduce the environmental noise, outer yoke discs  
 649 have been placed on both sides for the endcaps. At the innermost rings of the first station,  
 650 the CSCs have been upgraded by refurbishing the readout electronics to make use of the full  
 651 detector granularity instead of groups of three as was the case for Run 1. In Figure 2.7 (right),  
 652 the refurbishing of the CSCs is shown.

653 Since the HF experiences intense particle fluxes, it became clear during Run 1 that the glass  
 654 windows of the PMTs need replacing. For the ECAL in Run 1, the energy reconstruction happened  
 655 via a weighted sum of the digitized samples [88]. For Run 2 however, the reconstruction had  
 656 to be made more resistant for out of time pile up and a multi-fit approach has been set into  
 657 place. In this approach, the pulse shape is modelled as a sum of one in-time pulse plus the out  
 658 of time pulses [80]. The energy resolution is better than 2% in the central barrel region and  
 659 2-5 % elsewhere.

During the first data taking period of the LHC (2010 to 2013), the tracker operated at +4°C. With the higher LHC beam intensities from 2015 onwards, the tracker needs to be operated at much lower temperatures. The reason for this is that with intense irradiation, the doping concentration changes, the leakage current increases proportional to the fluence and the charge collection efficiency decreases due to charge trapping. Mostly the leakage current ( $I$ ) is affected by the temperature change:

$$I \propto T^2 e^{-\frac{E_g}{2kT}}, \quad (2.6)$$

660 where  $T$  is the operating temperature,  $E_g$  the band gap and  $k$  the Boltzmann constant. There is  
 661 approximately a factor 15 between the leakage currents at room temperatures and at -10 °C.

662 During the LS1, the CMS cooling plant was refurbished [89] and the fluorocarbon cooling  
 663 system overhauled. To help to suppress the humidity inside the tracker, new methods for vapour  
 664 sealing and insulation were applied. Furthermore, several hundred high-precision sensors are  
 665 used to monitor the humidity and temperature. In order to get as dry air as possible, a new  
 666 dry-gas plant provides eight times more dry gas (air or nitrogen) than during the first run, and  
 667 allows regulation of the flow. As a final addition, the cooling bundles outside the tracker are  
 668 equipped with heater wires and temperature sensors in order to maintain safe operations above  
 669 the cavern dew point. For the data taking in 2015-2016, the tracker operated at -15°C.

670 In Run 2, with the increase in centre of mass energy and a higher luminosity, a larger number  
 671 of simultaneous inelastic collisions per crossing is expected with respect to Run 1. For this, the  
 672 CMS Level-1 has been upgraded [90]. All hardware, software, databases and the timing control  
 673 system have been replaced for Run 2, where the main changes are that the muon system now  
 674 uses the redundancy of the muon detector system earlier to make a high resolution muon trigger.  
 675 Other upgrades are that the calorimeter system isn't bound any more for streaming data and  
 676 the global trigger has more Level-1 Trigger algorithms.

677 After the first half of Run 2, the innermost part of detection in CMS (pixel detector) was  
 678 replaced, enhancing the particle tracking capabilities of CMS. The data used in the framework

of this thesis however is from before this upgrade. More information on the Pixel upgrade can be found in Refs. [91, 92].

### 2.2.5 CMS computing model

The selected data is stored, processed and dispersed via the Worldwide Large Hadron Collider Computing Grid (WLCG) [93, 94]. This has a tiered structure that functions as a single, coherent system.

At CERN and the Wigner Research Center for physics, a single Tier-0 is located. The raw data collected by the experiments is archived here, and a first reconstruction of the data is done. This data is then already in a file format usable for physics analysis. Furthermore, it is able to reprocess data when new calibrations become available. The Tier-0 site distributes this data to a total of 14 Tier-1 centres. They carry out data reprocessing and store real data as well as simulated data. The Tier-1 further distributes the data to over 150 Tier-2 centres. These make the data accessible for physics analysis and are also being used for the production of simulated data. The data is made accessible for physicists around the world. For CMS, the Tier-0 site at CERN reconstructs the full collision events and the backup of the data is send to seven Tier-1 computer centres: France, Germany, Italy, Spain, Taiwan, UK, and the US. At the Tier-1 sites the events are again reconstructed using refined calibration constants. The patterns are created and the more complex events are sent to forty Tier-2 centres for specific analysis task.

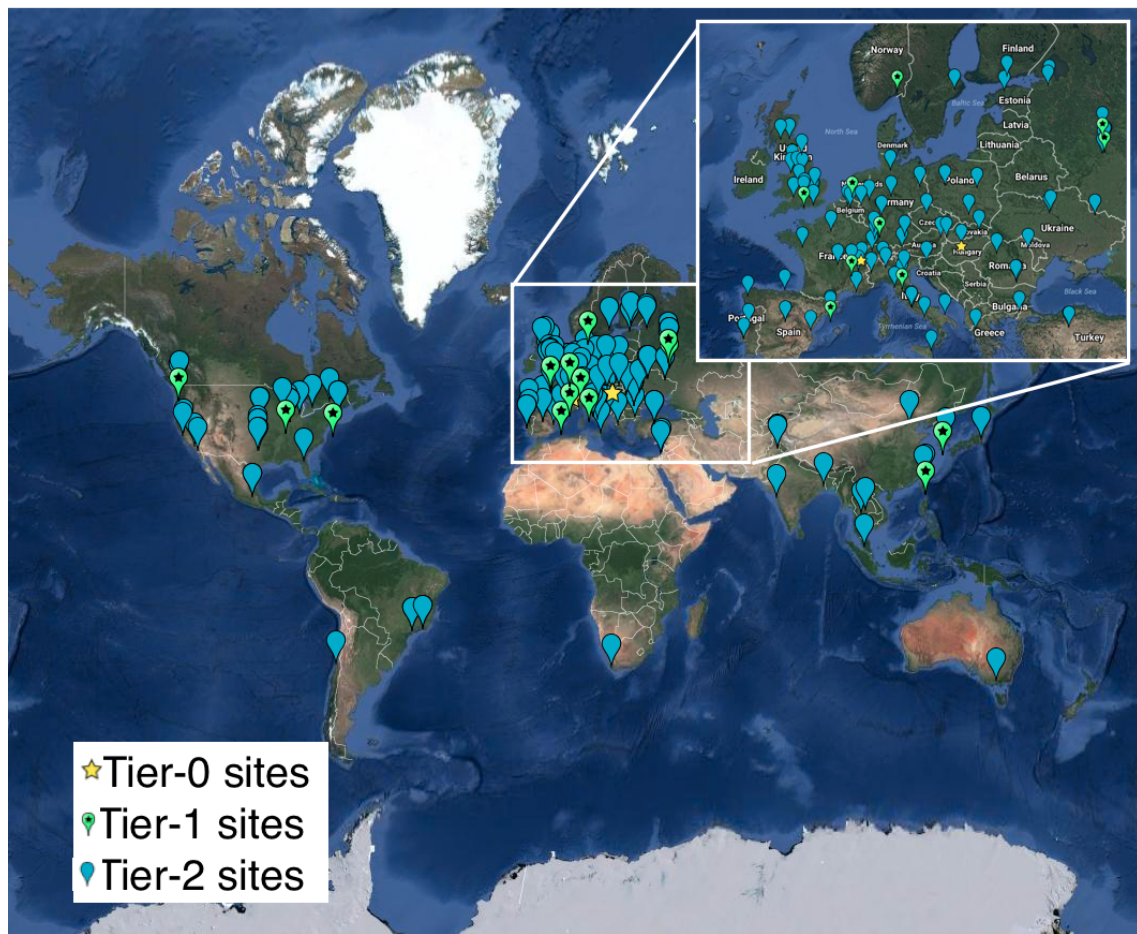


Figure 2.14: Worldwide LHC Computing Grid in 2017 [95].

# Analysis techniques

# 3

698 In order to study the collisions coming from high energy experiments, many tools have been  
 699 developed. In [Section 3.1](#), the physics of hadron collision at high energies are presented. These  
 700 insights are used to generate events via Monte Carlo event generators, explained in [Section](#)  
 701 [3.2](#). Machine learning helps to differentiate between signal- and background like events. In  
 702 [Section 3.3](#), the multivariate technique of boosted decision trees is explained. This yields  
 703 powerful discriminants for separating signal and background events and provides distributions  
 704 for template-based maximum likelihood fits. The fitting method used in the search presented  
 705 in this thesis is discussed in [Section 3.4](#).

## 706 3.1 Hadron collisions at high energies

All partons can be approximated as free when there is sufficiently high momentum transfer in hadron collisions. This makes it possible to treat a hadron-hadron scattering as a single parton-parton interaction. The momentum of the parton can then be expressed as a fraction of the hadron momentum

$$\vec{p}_{\text{parton}} = x \vec{p}_{\text{hadron}}, \quad (3.1)$$

where  $x$  is referred to as the Björken scaling variable. The interaction  $p_A p_B \rightarrow X$  can then be factorised in terms of partonic cross sections  $\hat{\sigma}_{ij \rightarrow X}$  [96]

$$\sigma_{p_A p_B \rightarrow X} = \sum_{ij} \iint dx_1 dx_2 f_i^A(x_1, Q^2) f_j^B(x_2, Q^2) d\hat{\sigma}_{ij \rightarrow X}, \quad (3.2)$$

707 where  $i$  and  $j$  are the partons resolved from protons A and B. The parton density functions  
 708 (PDF) are denoted as  $f_i(x_j, Q^2)$ , and  $Q^2$  is the factorisation scale more commonly denoted as  
 709  $\mu_F$ . This factorisation scale represents the energy at which the hadronic interaction can be  
 710 expressed as a product of the partonic cross section and the process independent PDF. In [Figure](#)  
 711 [3.1](#), the kinematic regions in  $x$  and  $\mu_F$  are shown for fixed target and collider experiments.

712 The parton density functions (PDF) [97–99] represent the momentum distribution of the  
 713 proton amongst its partons at an energy scale  $\mu_F$ . These functions are obtained from global  
 714 fits to data since they can not be determined from first principles. From measurements on deep

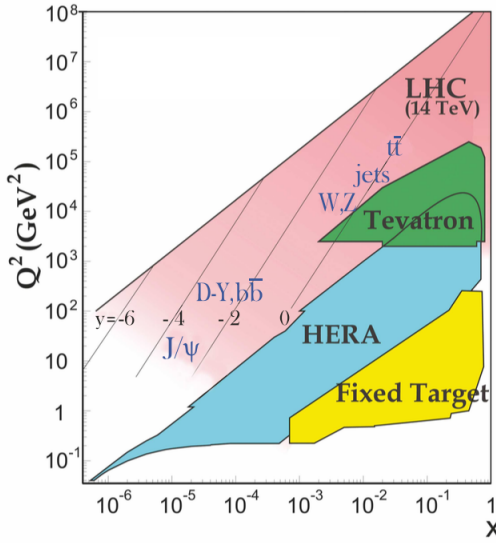


**Figure 3.1:** Kinematic regions in momentum fraction  $x$  and factorisation scale  $Q^2$  probed by fixed-target and collider experiments. Some of the final states accessible at the LHC are indicated in the appropriate regions, where  $y$  is the rapidity. In this figure, the incoming partons have  $x_{1,2} = (M/14\text{TeV})e^{\pm y}$  with  $Q = M$  where  $M$  is the mass of the state shown in blue in the figure. For example, exclusive  $J/\psi$  and  $\Upsilon$  production at high  $|y|$  at the LHC may probe the gluon PDF down to  $x \sim 10^{-5}$ . Figure taken from [6].

715 inelastic scattering using lepton-proton collision by the HERA collider [100], supplemented  
 716 with proton-antiproton collisions from the Tevatron [101], and proton collision data from the  
 717 ATLAS, CMS and LHCb collaborations at the LHC (Run 1) [102] the PDFs are determined and  
 718 included in global PDF sets known as the PDF4LHC recommendation [99]. Their measurement  
 719 at scale  $\mu_F$  is extrapolated to higher energies by use of the DGLAP equations [103]. Once  
 720 these PDFs are known, the cross section of a certain process can be calculated and used as  
 721 input for the Monte Carlo generators used to make the simulated data samples at the LHC. In  
 722 the framework of this thesis, the NLO PDF4LHC15\_100 set is used. This set is an envelope of  
 723 three sets: CT14, MMHT2014 and NNPDF3.0 [99]. As illustration, the dependency of the PDFs  
 724 on the momentum fraction  $x$  is shown for the NNPDF3.0 set on hadronic scale  $\mu_F^2 = 10\text{GeV}^2$   
 725 and LHC scale  $\mu_F^2 = 10^4\text{GeV}^2$  in Figure 3.2. The gluon density dominated for most values of  
 726 the momentum fraction, implying that it is easier to probe gluons than the quarks. When the  
 727 Björken scale is to one, the parton densities of the valence quarks of the proton, up and down  
 728 quarks, dominate over the gluon density. The sea quarks originating from gluon splitting, the  
 729 charm, anti-up, and anti-down quarks, have lower densities in general for the proton. The  
 730 resolution scale  $Q^2$  is typically taken to be the energy scale of the collision. For the top quark pair  
 731 production a scale of  $Q^2 = (350\text{ GeV})^2$  is chosen, meaning that the centre-of-mass energy of the  
 732 hard interaction is about twice the top quark mass. The uncertainty on the parton distributions  
 733 is evaluated using the Hessian technique [104], where a matrix with a dimension identical to  
 734 the number of free parameters needs to be diagonalised. In the case of PDF4LHC15\_100 set, this  
 735 translates into 100 orthonormal eigenvectors and 200 variations of the PDF parameters in the  
 736 plus and minus direction.

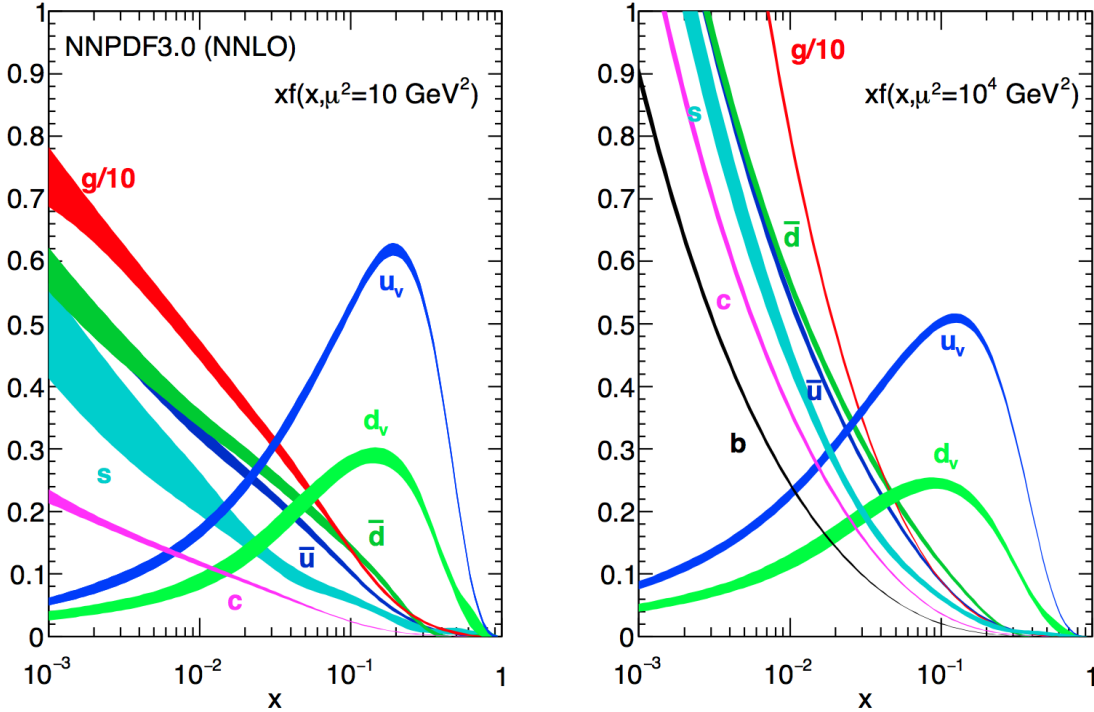


**Figure 3.2:** The momentum fraction  $x$  times the parton distribution functions  $f(x)$ , where  $f = u_v, d_v, \bar{u}, \bar{d}, s, c$ , or  $g$  as a function of the momentum fraction obtained in the NNLO NNPDF3.0 global analysis at factorisation scales  $\mu^2 = 10 \text{ GeV}^2$  (left) and  $\mu^2 = 10^4 \text{ GeV}^2$  (right), with  $\alpha_s(M_Z^2) = 0.118$ . The gluon PDF has been scaled down by a factor of 0.1. Figure taken from [6].

Quantum fluctuations can cause divergences at high energies. This is solved by introducing a renormalization scale  $\mu_R$  to redefine physical quantities, making the theory still able to describe the experimental regime. A consequence of this method is that the coupling constants will run as a function of  $\mu_R$ . Beyond the renormalization scale, the high energy effects such as the loop corrections to propagators (self energy) are absorbed in the physical quantities through a renormalization of the fields. In particular the running behaviour of the strong coupling constant<sup>1</sup>  $\alpha_S$  is found to be

$$\alpha_S = \frac{\alpha_S(\mu_0^2)}{1 + \alpha_S(\mu_0^2) \frac{33-2n_f}{12\pi} \ln\left(\frac{|\mu_R^2|}{\mu_0^2}\right)}, \quad (3.3)$$

with  $n_f$  the number of quarks and  $\mu_0$  the reference scale at which the coupling is known. The current world average of the strong coupling constant at the Z boson mass is  $\alpha_S(\mu_R = m_Z) = 0.1181 \pm 0.0011$  [6]. From Equation 3.3 one can see easily that the coupling strength decreases with increasing renormalization scale, this is known as asymptotic freedom. Additionally, following the behaviour of  $\alpha_S(\mu_R^2)$ , a limit  $\Lambda_{\text{QCD}} \approx 200 \text{ MeV}$  is found for which  $\alpha_S$  becomes larger than one. Under this limit, the perturbative calculations of observables can no longer be done.

<sup>1</sup>The strong coupling constant is defined as  $\alpha_S = \frac{g_S^2}{4\pi}$ .

Cross sections can be written in terms of interacting vertices contributing to the matrix element (ME) originating from elements of a perturbative series [105], allowing them to be expanded as a power series of the coupling constant  $\alpha$

$$\sigma = \sigma_{\text{LO}} \left( 1 + \left( \frac{\alpha}{2\pi} \right) \sigma_1 + \left( \frac{\alpha}{2\pi} \right)^2 \sigma_2 + \dots \right). \quad (3.4)$$

744 Leading order (LO) accuracy contains the minimal amount of vertices in the process, then  
 745 depending on where the series is cut off one speaks of next-to-leading order (NLO), or next-to-  
 746 next-to-leading order (NNLO) accuracy in  $\alpha$ . Predictions including higher order corrections  
 747 tend to be less affected by theoretical uncertainties originating from a variation of the chosen  
 748 renormalization and factorisation scales.

## 749 3.2 Event generation

750 In order to compare reconstructed data with theoretical predictions, collision events are gener-  
 751 ated and passed through a simulation of the CMS detector and an emulation of its readout. For  
 752 the detector simulation, a so-called Full Simulation package [106, 107] based on the Geant4  
 753 toolkit [108] is employed. This allows detailed simulations of the interactions of the particles  
 754 with the detector material.

### 755 3.2.1 Fundamentals of simulating a proton collision

756 The generation of  $\text{pp} \rightarrow \text{X}$  events is subdivided into sequential steps [109–111], as shown in  
 757 [Figure 3.3](#).

758 The interaction of two incoming protons is often soft and elastic leading to events that are not  
 759 interesting in the framework of this thesis. More intriguing are the hard interactions between  
 760 two partons from the incoming protons. The event generation starts from the matrix elements of  
 761 a hard scattering process of interest. The corresponding cross section integral is sampled using  
 762 Monte Carlo techniques and the resulting sample of events reflect the probability distribution  
 763 of a process over its final state phase space. A parton shower (PS) program is then used to  
 764 simulate the hadronisation of final state partons, coming from the sample of events of the hard  
 765 interaction, into hadrons which then decay further. On top of this, radiation of soft gluons or  
 766 quarks from initial or final state partons is simulated. These are respectively referred to as  
 767 initial state radiation (ISR) or final state radiation (FSR). The contributions from soft secondary  
 768 interactions, the so-called underlying event (UE), and colour reconnection effects are also taken  
 769 into account. A brief overview of the employed programs used for the event generation of the  
 770 signal and main background processes used in the search presented in the thesis is given in  
 771 [Section 3.2.2](#).

### 772 3.2.2 Programs for event generation

773 The FEYNRULES package [112] allows for the calculation of the Feynman rules in momentum  
 774 space for any quantum field theory model. By use of a Lagrangian, the set of Feynman rules asso-  
 775 ciated with this Lagrangian is calculated. Via the Universal FeynRules Output (UFO) [113]  
 776 the results are then passed to matrix element generators.

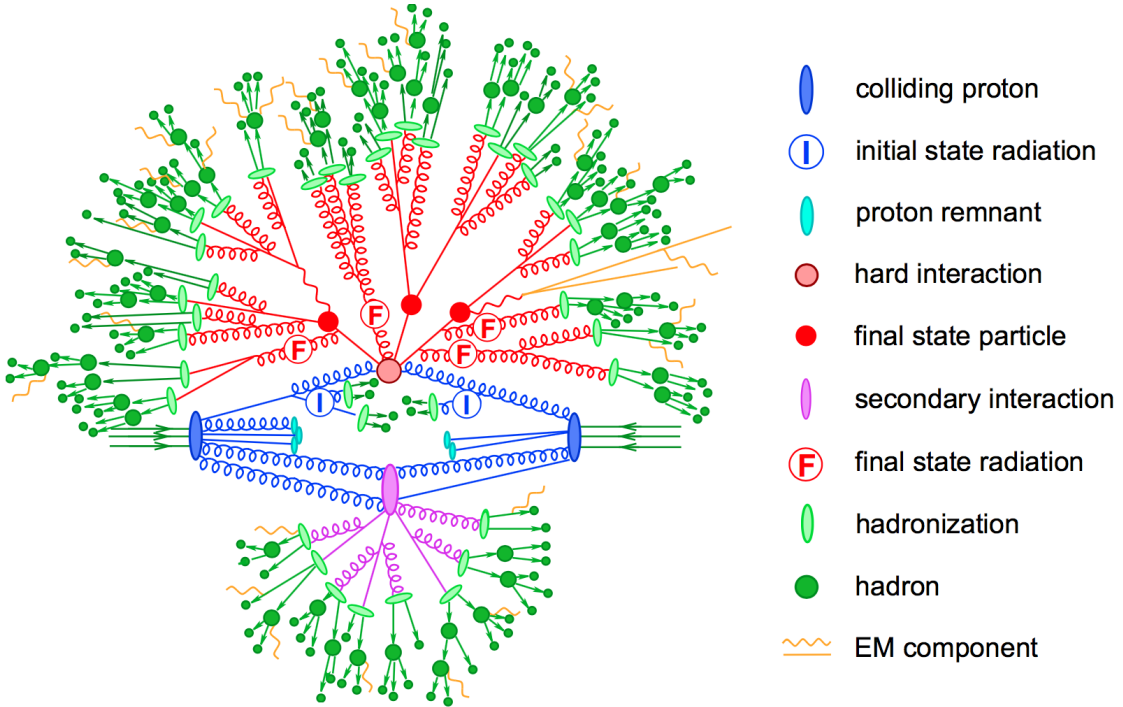


**Figure 3.3:** Sketch of a hadron collision as simulated by a Monte-Carlo event generator. The red blob in the centre represents the hard collision, surrounded by a tree-like structure representing Bremsstrahlung as simulated by parton showers. The purple blob indicates a secondary hard scattering event. Parton-to-hadron transitions are represented by light green blobs, dark green blobs indicate hadron decays, while yellow lines signal soft photon radiation. Figure taken from [111].

777     The MadGraph program [114] is used to interpret the physics model and calculate the cor-  
 778     responding Feynman diagrams and matrix elements. After this, MadEvent [115] is used to  
 779     calculate the corresponding partons. These generated parton configurations are then merged  
 780     with Pythia [116–118] parton showers using the MLM merging scheme [119].

781     The MadGraph5\_aMC@NLO program [120] combines the LO MadGraph [114] and the aMC@NLO  
 782     program into a common framework. This combination supports the generation of samples at  
 783     LO or NLO together with a dedicated matching to parton showers using the MC@NLO [121]  
 784     or FxFx [122] schemes respectively. The FxFx scheme produces a certain fraction of events  
 785     with negative weights originating from the subtraction of amplitudes that contain additional  
 786     emissions from the NLO matrix element to prevent double-counting.

787     The POWHEG box (versions 1 and 2) [123–128] contains predefined implementations of various  
 788     processes at NLO. It applies the POWHEG method for ME- to PS- matching, where the hardest  
 789     radiation generated from the ME has priority over subsequent PS emission to remove the overlap  
 790     with the PS simulation.

791     The JHU generator (version 7.02) [129–132] is used to generate the parton level information  
 792     including full spin and polarization correlations. It is commonly used for studying the spin and  
 793     parity properties of new resonances such as  $ab \rightarrow X \rightarrow VV$ , where  $V = Z, W, \gamma$ .

794     The generation of events from processes involving the production and decay of resonances  
 795    creates a computational heavy load, especially at NLO. The narrow width approximation assumes  
 796    that the resonant particle is on-shell. This factorizes the production and decay amplitude,  
 797    allowing to perform the simulation of the production and decay of heavy resonances like top  
 798    quarks or Higgs bosons to be performed in separate steps. The MadSpin program [133] extends  
 799    this approach and accounts for off-shell effects through a partial reweighting of the events.  
 800    Additionally, spin correlation effects between production and decay products are taken into  
 801    account.

802     The Pythia program (versions 6 and 8) [116–118] generates events of various processes at  
 803    LO. However more commonly it is only used for its PS simulation and is then used after other  
 804    LO and NLO event generators to perform subsequent parton showering, hadronisation, and  
 805    simulation of the underlying event. In this thesis the underlying event tunes [134] are the  
 806    CUETP8M2T4, CUETP8M1 and CUETP8M2.

807     The detector response is simulated via the Geant4 [108] program. This program tracks the  
 808    particles through the detector material via a detailed description of the detector and generates  
 809    several hits throughout several sensitive layers. In addition, the response of the detector  
 810    electronics to these hits are simulated.

### 811    3.2.3 Generating FCNC top-Z interactions

812     The FCNC processes are generated by interfacing the Lagrangian in Equation 1.36 with  
 813    MadGraph5\_aMC@NLO by means of the FeynRules package and its Universal FeynRules  
 NOTE: RH<sup>814</sup>  
 and LH<sup>815</sup>  
 gave the<sup>816</sup>  
 same re-<sup>817</sup>  
 sulting vari-<sup>818</sup>  
 ables and<sup>819</sup>  
 RH is easier<sup>820</sup>  
 to simulate<sup>821</sup>  
 since those<sup>822</sup>  
 are singlets<sup>823</sup>  
 under SU<sup>821</sup>  
 (no doublet<sup>822</sup>  
 with b)<sup>823</sup>

814    Output format. The complex chiral parameters are arbitrary chosen to be  $f_{Xq}^L = 0$  and  $f_{Xq}^R = 1$ .  
 815    The processes are generated with the MadGraph5\_aMC@NLO (version 2.2.2) and showered with  
 816    Pythia (version 8.22). The signal consists of two components: events describing the top quark  
 817    pair production followed by an FCNC decay of one top quark ( $t \rightarrow Zq$ ), and events with the  
 818    FCNC single top quark production ( $Zq \rightarrow t$ ) for which the top quark decays according the to  
 819    SM. The leading order generation of the single top quark FCNC process  $tZ+0,1$  jet including a  
 820    merging technique can not be done since  $tZ+1$  jet also contains contributions from top quark  
 821    pair FCNC where one quark is decaying in  $tZ$ . Therefore, single top quark and top quark pair  
 822    processes are generated independently, where the single top quark process is generated without  
 823    the extra hard jet, and the top quark pair FCNC process is generated with up to two extra jets.

824     The signal rates are estimated by use of the MadGraph5\_aMC@NLO program for estimating the  
 825    partial widths. The anomalous couplings are left free to float for this estimation, and only one  
 826    coupling is allowed to be non-vanishing at a time. The results are presented in Table 3.1.

827     The anomalous single top quark cross sections are calculated by convolution of the hard  
 828    scattering matrix elements with the LO order set of NN23L01 [135] partons densities. The NLO  
 829    effects are modelled by multiplying each LO cross section by a global  $k$ -factor. The LO single top  
 830    quark production cross section and the global  $k$ -factors for the top-Z production are shown in  
 831    Table 3.2. The hard scattering events are then matched to parton showers to Pythia to account  
 832    for the simulation of the QCD environment relevant for hadronic collisions.

**Table 3.1:** Leading order partial widths related to the anomalous decay modes of the top quark, where the new physics scale  $\Lambda$  is given in GeV.

Anomalous coupling	vertex	Partial decay width (GeV)
$\kappa_{tZq}/\Lambda$	tZu	$1.64 \times 10^4 \times (\kappa_{tZu}/\Lambda)^2$
	tZc	$1.64 \times 10^4 \times (\kappa_{tZc}/\Lambda)^2$
	tZu	$1.69 \times 10^{-1} \times (\zeta_{tZu})^2$
	tZc	$1.68 \times 10^{-1} \times (\zeta_{tZc})^2$

**Table 3.2:** Leading order single top quark production cross section at a centre-of-mass of 13 TeV for  $pp \rightarrow tZ$  or  $t\bar{Z}$ , where the new physics scale is given in GeV. The NLO  $k$ -factors [136] are given in the last column.

Anomalous coupling	vertex	Cross section (pb) $pp \rightarrow t + pp \rightarrow \bar{t}$	$\sigma_{pp \rightarrow \bar{t}}/\sigma_{pp \rightarrow t}$	NLO $k$ -factor
$\kappa_{tZq}/\Lambda$	tZu	$1.92 \times 10^7 \times (\kappa_{tZu}/\Lambda)^2$	0.12	1.40
	tZc	$2.65 \times 10^6 \times (\kappa_{tZc}/\Lambda)^2$	0.50	1.40
$\zeta_{tZq}$	tZu	$8.24 \times 10 \times (\zeta_{tZu})^2$	0.14	1.40
	tZc	$1.29 \times 10 \times (\zeta_{tZc})^2$	0.50	1.40

The top quark pair cross sections are derived from the SM  $t\bar{t}$  cross section, calculated with MadGraph5\_aMC@NLO at NLO at a centre-of-mass of 13 TeV ( $\sigma_{t\bar{t}}^{\text{SM,NLO}} = 6.741 \times 10^2 \text{ pb}$ ), and considering the decay  $t\bar{t} \rightarrow (bW^\pm)(Xqt)$ . The branching ratio  $\mathcal{B}(t \rightarrow bW^\pm)$  is assumed to be equal to one and the FCNC branching ratio is calculated as

$$\mathcal{B}(t \rightarrow qX) = \frac{\Gamma_{t \rightarrow qX}}{\Gamma_t^{\text{SM}} + \Gamma_t^{\text{FCNC}}} \approx \frac{\Gamma_{t \rightarrow qX}}{\Gamma_t^{\text{SM}}}, \quad (3.5)$$

833 where  $\Gamma_{t \rightarrow qX}$  is given in Table 3.1,  $\Gamma_t^{\text{SM}} = 1.32 \text{ GeV}$  [47], and the assumption  $\Gamma_t^{\text{FCNC}} \ll \Gamma_t^{\text{SM}}$  is  
834 made. In Table 3.3 the resulting NLO cross sections for the top-Z FCNC interactions are given.

**Table 3.3:** Next to leading order top quark pair cross section for the top-Z FCNC interactions  $t\bar{t} \rightarrow (bW^\pm)(X_{qt})$  with a full leptonic decay at a centre-of-mass of 13 TeV, where  $\sigma_{pp \rightarrow t\bar{t}}^{\text{SM,NLO}} = 6.741 \times 10^2 \text{ pb}$ ,  $\mathcal{B}(Z \rightarrow \ell\bar{\ell}) = 3.36 \times 3 \times 10^{-2}$ , and  $\mathcal{B}(W \rightarrow \ell\nu) = 10.80 \times 3 \times 10^{-2}$ .

Anomalous coupling	vertex	Process	Cross section (pb)
$\kappa_{tZq}/\Lambda$	$tZ_u$	$t\bar{t} \rightarrow (b\ell^+\nu)(\bar{u}\ell^+\ell^-)$	$2.727 \times 10^5 \times (\kappa_{tZu}/\Lambda)^2$
		$t\bar{t} \rightarrow (\bar{b}\ell^-\bar{\nu})(u\ell^+\ell^-)$	$2.727 \times 10^5 \times (\kappa_{tZu}/\Lambda)^2$
	$tZ_c$	$t\bar{t} \rightarrow (b\ell^+\nu)(\bar{c}\ell^+\ell^-)$	$2.726 \times 10^5 \times (\kappa_{tZc}/\Lambda)^2$
		$t\bar{t} \rightarrow (\bar{b}\ell^-\bar{\nu})(c\ell^+\ell^-)$	$2.726 \times 10^5 \times (\kappa_{tZc}/\Lambda)^2$
$\zeta_{tZq}$	$tZ_u$	$t\bar{t} \rightarrow (b\ell^+\nu)(\bar{u}\ell^+\ell^-)$	$2.807 \times (\zeta_{tZu})^2$
		$t\bar{t} \rightarrow (\bar{b}\ell^-\bar{\nu})(u\ell^+\ell^-)$	$2.807 \times (\zeta_{tZu})^2$
	$tZ_c$	$t\bar{t} \rightarrow (b\ell^+\nu)(\bar{c}\ell^+\ell^-)$	$2.807 \times (\zeta_{tZc})^2$
		$t\bar{t} \rightarrow (\bar{b}\ell^-\bar{\nu})(c\ell^+\ell^-)$	$2.807 \times (\zeta_{tZc})^2$

### 3.2.4 Generating SM background events

The SM  $tZq$  sample is generated using the MadGraph5\_aMC@NLO generator (version 2.2.2) [137] at leading order accuracy. The  $t\bar{t}Z$  and triboson samples were generated using the MadGraph5\_aMC@NLO generator (version 2.2.2), interfaced through the dedicated MC@NLO matching scheme [121]. The  $WZ + \text{jets}$  and  $t\bar{t}W$  samples are produced with up to one additional parton at next-to-leading order accuracy using MadGraph5\_aMC@NLO (version 2.2.2) and using FxFx approach [138] for matching and merging. Other minor background are simulated using different generators. The samples of  $t\bar{t}H$ ,  $WW$ ,  $ZZ$ , and single top quark production channels are generated with the POWHEG box (versions 1 and 2) [123–128]. The JHU generator [129–132] is used for the  $tqH$  sample, while the  $tWZ$  sample is generated using MadGraph [114] interfaced with the MLM matching scheme [119]. All events are interfaced to Pythia version 8.22 [118] to simulate parton shower, hadronisation, and underlying event. Additionally, MadSpin is used for the  $tZq$ ,  $WZ + \text{jets}$ ,  $t\bar{t}Z$ ,  $t\bar{t}W$ ,  $tWZ$ , and triboson samples.

The complete list of SM samples is given in Table 3.4, along with their cross sections at a centre-of-mass of 13 TeV. The cross sections without a reference are coming from the generator with which the sample has been made, for some of them the uncertainties are provided by the Generator Group [139]. For each MC sample, the integrated luminosity that the sample represents is estimated as the number of simulated events divided by the cross section of the generated process. This luminosity is then matched to integrated luminosity of  $35.9 \text{ fb}^{-1}$  represented by the data used for analysis. For processes generated with MadGraph5\_aMC@NLO, the effective number of simulated events is used, taking into account positive and negative event weights. In Figure 3.4, a summary is given of the SM cross section measurements performed by the CMS collaboration. These cross sections are all in agreement with their SM predictions.

**Table 3.4:** SM MC samples used in this analysis with their corresponding cross section at a centre-of-mass of 13 TeV and MadGraph5\_aMC@NLO correction C when applicable. The generators used for each sample are indicated and the simulation of the parton shower, hadronisation, and underlying event is done by Pythia version 8.22 [118] for all samples.

Process	Generator	Cross section (pb)	C	Ref.
$WZ \rightarrow 3\ell\nu$	MadGraph5_aMC@NLO+MadSpin	5.26	1.61	[139]
$tZq$ with $Z \rightarrow \ell^+\ell^-$	MadGraph5_aMC@NLO+MadSpin	0.0758	3.77	[139]
$tqH$ with $H \rightarrow ZZ \rightarrow \ell^+\ell^-\ell^+\ell^-$	JHU	$8.80 \cdot 10^{-6}$	-	[139]
$t\bar{t}W + \text{jets}$ with $W \rightarrow \ell\nu$	MadGraph5_aMC@NLO+MadSpin	$0.2043 \pm 0.0020$	1.94	[139]
$t\bar{t}Z \rightarrow 2\ell + 2\nu + \text{other}$ , with $m_{\ell\ell} > 10$ GeV	MadGraph5_aMC@NLO+MadSpin	$0.2529 \pm 0.0004$	2.15	[139]
$t\bar{t}H, \text{no } b\bar{b} \text{ decays}$	POWHEG	0.2151	-	[139]
$t\bar{t}H, b\bar{b} \text{ decays}$	POWHEG	0.2934	-	[139]
$WW \rightarrow 2\ell 2\nu$	POWHEG	12.178	-	[140]
$ZZ \rightarrow 4\ell$	POWHEG	0.3366	-	[139]
$WZZ$	MadGraph5_aMC@NLO+ MadSpin	0.05565	1.14	[139]
$ZZZ$	MadGraph5_aMC@NLO	0.01398	1.17	[139]
single top quark $tWZ$ , with $Z_\mu \rightarrow \ell^+\ell^-$	MadGraph5_aMC@NLO(LO)+MadSpin	0.001123	-	[139]
single top quark t-channel $\bar{t}$	POWHEG+MadSpin	$44.33^{+1.76}_{-1.49}$	-	[139]
single top quark t-channel $t$	POWHEG+MadSpin	$26.38^{+1.32}_{-1.18}$	-	[139]
single top quark $t\bar{W}$	POWHEG	$35.85 \pm 0.90 \text{ (scale)} \pm 1.70 \text{ (PDF)}$	-	[139]
single top quark $tW$	POWHEG	$35.85 \pm 0.90 \text{ (scale)} \pm 1.70 \text{ (PDF)}$	-	[139]
$t\bar{t}$	POWHEG	$831.76^{+19.77+35.06}_{-29.20-35.06}$	-	[139]
$Z/\gamma^* + \text{jets}$ , with $m_{\ell\ell} > 50$ GeV	MadGraph5_aMC@NLO	$3 \times (1921.8 \pm 0.6 \pm 33.2)$	1.49	[139]
$Z/\gamma^* + \text{jets}$ , with $10 \text{ GeV} < m_{\ell\ell} < 50 \text{ GeV}$	MadGraph	18610	-	[139]

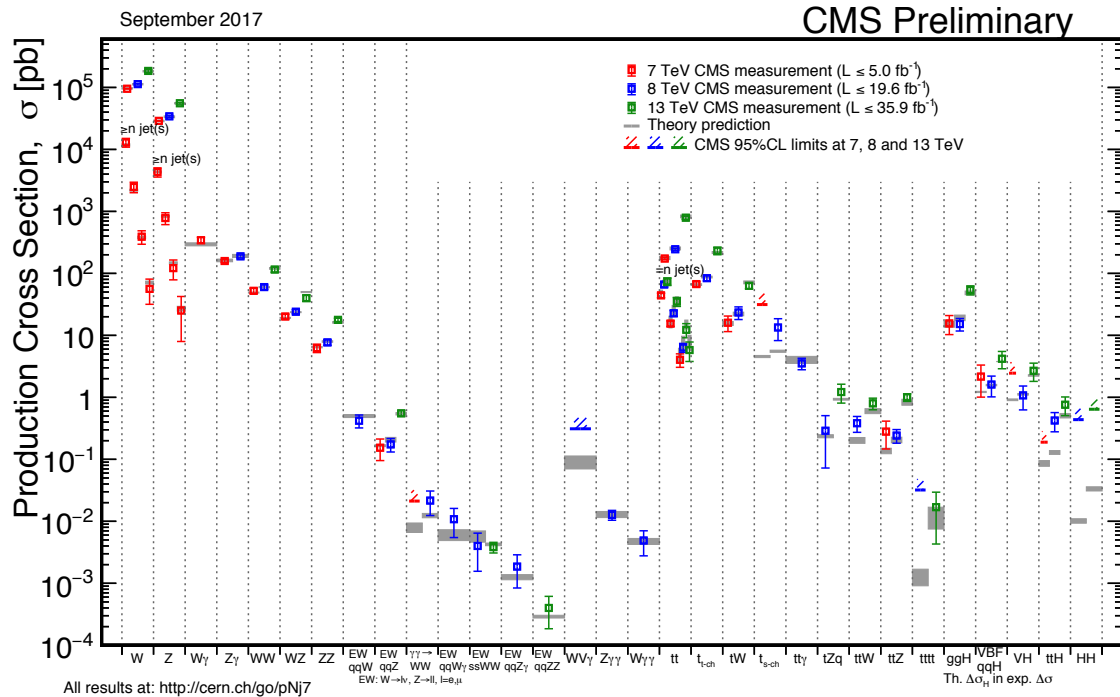


**Figure 3.4:** Summary of the SM cross section measurements performed by the CMS collaboration. Figure taken from [23]

### 3.3 Multivariate analysis techniques: Boosted Decision Trees

The need of processing large quantities of data and discriminating between events with largely similar experimental signatures makes multivariate analysis (MVA) a largely used method in the physics community. Multivariate classification methods based on machine learning techniques are a fundamental ingredient to most analyses. The advantage of using a MVA classifier is that it can achieve a better discrimination power with respect to a simpler analysis based on individual selection criteria or poorly discriminating variables. A risk of using MVA classifiers is overtraining. This happens when there are too many model parameters of an algorithm adjusted to too few data points. This leads to an increase in the classification performance over the objectively achievable one.

There are many software tools that exist for MVA. In this thesis the Tool for Multivariate Analysis (TMVA) [141] is used. This software is an open source project included into ROOT [142]. By training on events for which the classification is known, a mapping function is determined that describes a classification or an approximation of the underlying behaviour defining the target value (regression). In this thesis boosted decision trees (BDT) are employed for the classification of events as implemented in the TMVA framework [141]. This multivariate technique is based on a set of decision trees where each tree yields a binary output depending on the fact that an event is signal- or background-like. This has as advantage that several discriminating variables can be combined into a powerful one-dimensional discriminant  $D$ .

877 The decision tree is constructed by training on a dataset for which the outcome is already  
 878 provided, such as simulation datasets with signal and background processes (supervised learn-  
 879 ing). Different trees can be combined into a forest where the final output is determined by the  
 880 majority vote of all trees, so-called boosting. This stabilises the decision trees against statistical  
 881 fluctuations and makes it possible to keep the decision trees very shallow, making the method  
 882 more robust against overtraining. Examples of such boosting algorithms are Adaptive Boosting  
 883 (AdaBoost) and Gradient Boosting [143]. In this thesis Gradient boost is used with a learning  
 884 rate of 0.2-0.3 and the depth of the tree is set to three. Additionally, the Gradient boost is  
 885 used in combination with bagging, so-called stochastic gradient boosting. Bagging smears the  
 886 statistical fluctuations in the training data and therefore stabilises the response of the classifier  
 887 and increases the performance by eliminating overtraining. More information about stochastic  
 888 gradient boosting can be found in Ref. [144].

889 The discriminating power of a BDT is assessed by analysing the receiver operating characteristic  
 890 (ROC) curve. This curve represents the background rejection over the signal efficiency of the  
 891 remaining sample. The area under the curve (AUC) is compared to random guessing in order  
 892 to identify the best classifier can be identified. When the multivariate discriminator has no  
 893 discriminating power, the resulting AUC will be 0%, while 50% means fully separated event  
 classes. In Figure 3.5 examples of ROC curves are shown.

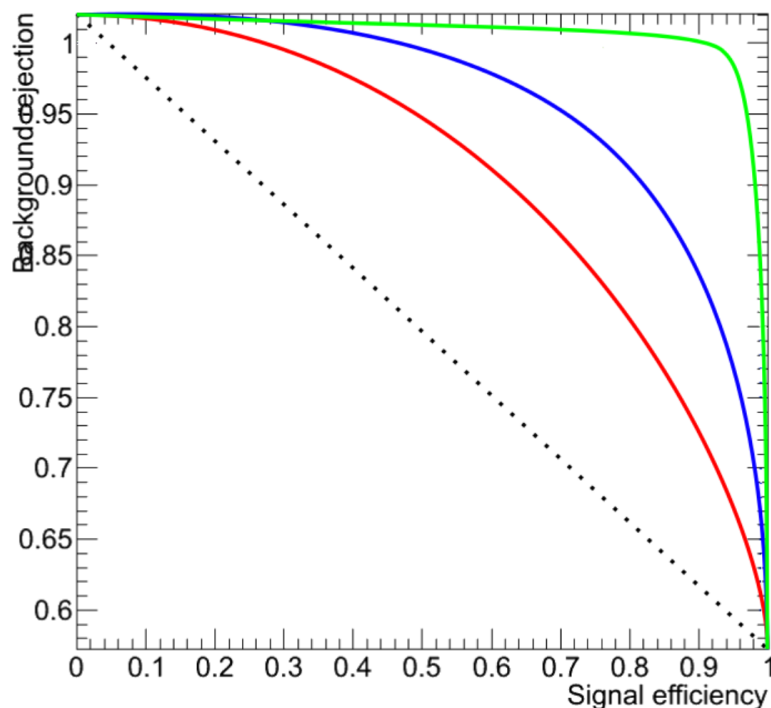


**Figure 3.5:** Example of ROC curves. In this example, the green method is better than the blue one, which is better than the red one. The dashed line represents a case where there is no separation. Figure taken from [145].

### 895 3.4 Statistical methodology

896 The search performed in the framework of this thesis requires the simultaneous analysis of data  
 897 from different decay channels. The statistical methodology used for this search is developed by  
 898 the ATLAS and CMS collaborations in the context of the LHC Higgs Combination group [146–  
 899 149]. The Higgs Combined Tool [150] is a RooStats [151] framework which runs different  
 900 statistical methods. In this section, only the statistical tools necessary for the performed search  
 901 are described [152].

902 The event yields of signal and background processes are denoted as  $s$  and  $b$  respectively.  
 903 These represent event counts in multiple bins or unbinned probability density functions. By  
 904 use of simulation, predictions on both signal and background yields are made the multiple  
 905 uncertainties on these predictions are accounted for by introducing nuisance parameters  $\theta$  such  
 906 that  $s = s(\theta)$  and  $b = b(\theta)$ .

907 The Bayesian and modified classical frequentist statistical approaches are used in high energy  
 908 physics to characterise the absence of a signal. The level of incompatibility of data with a signal  
 909 hypothesis is quantified in terms of confidence levels (CL). The convention is to require a 95%  
 910 CL for excluding a signal. In general limits are not set on the signal cross section directly, but  
 911 are set on the signal strength modifier  $\mu$ . The signal strength modifier is defined such that it  
 912 equally changes all the cross sections of all production mechanisms of the signal by the same  
 913 scale.

In this thesis, the modified frequentist approach [153, 154] for confidence levels that adopts the classical frequentist method to allow nuisance parameters, is used. It constructs a likelihood  $\mathcal{L}(\text{data}|\mu, \theta)$  is as

$$\mathcal{L}(\text{data}|\mu, \theta) = \text{Poisson}(\text{data}|\mu s(\theta) + b(\theta)) \text{pdf}(\tilde{\theta}|\theta). \quad (3.6)$$

914 The probability density function  $\text{pdf}(\tilde{\theta}|\theta)$  describes all sources of uncertainty. In this thesis, all  
 915 sources of uncertainties are assumed to be either 100% correlated or uncorrelated. Partially  
 916 correlated uncertainties are broken down to subcomponents that fit those requirements, allowing  
 917 to include all constraints in the likelihoods in a clean factorised form.

A systematic uncertainty pdf  $\rho(\theta|\tilde{\theta})$  for the nuisance  $\theta$  with nominal value  $\tilde{\theta}$  is used. It reflects the degree of belief of what the true value of the  $\theta$  is. In this thesis, the approach from the Higgs Combined Tool is used where the pdfs  $\rho(\theta|\tilde{\theta})$  are re-interpret as posteriors of real or imaginary measurements  $\tilde{\theta}$

$$\rho(\theta|\tilde{\theta}) \sim \text{pdf}(\tilde{\theta}|\theta) \pi_\theta(\theta), \quad (3.7)$$

918 where  $\pi_\theta(\theta)$  is the hyper prior for the (imaginary) measurements. The the pdfs used by the  
 919 Higgs Combine Tool are described in Ref. [149].

The data in Equation 3.6 represents either the actual observation or pseudo-data to construct sampling distributions. For a binned likelihood, the Poisson probabilities to observe  $n_i$  events in bin  $i$  is given as

$$\text{Poisson}(\text{data}|\mu s(\theta) + b(\theta)) = \prod_i \frac{(\mu s_i(\theta) + b_i(\theta))^{n_i}}{n_i!} e^{-\mu s_i(\theta) - b_i(\theta)}. \quad (3.8)$$

At the LHC, the test statistic is defined as

$$q_\mu = -2 \ln \frac{\mathcal{L}(\text{data} | \mu, \hat{\theta}_\mu)}{\mathcal{L}(\text{data} | \hat{\mu}, \hat{\theta}_\mu)}, \quad (3.9)$$

where the likelihood is maximised in the numerator (maximum likelihood estimator, MLE) for a given  $\mu$  and (pseudo) data at  $\hat{\theta}_\mu$ , while  $\hat{\mu}$  combined with  $\hat{\theta}$  defines the point for which the likelihood reaches its global maximum. The estimated signal strength modifier  $\hat{\mu}$  can not become negative since a signal rate is positive defined by physics. Furthermore, an upper constraint on the MLE  $\hat{\mu} \leq \mu$  is imposed.

The signal is excluded at  $1 - \alpha$  confidence level when

$$\text{CLs} = \frac{P(q_\mu \geq q_\mu^{\text{obs}} | \mu s + b)}{P(q_\mu \geq q_\mu^{\text{obs}} | b)} \leq \alpha, \quad (3.10)$$

with  $P(q_\mu \geq q_\mu^{\text{obs}} | \mu s + b)$  the probability to observe a value of the test statistic at least as large as the one observed in data  $q_\mu^{\text{obs}}$ , under the signal plus background ( $s + b$ ) hypothesis, and  $P(q_\mu \geq q_\mu^{\text{obs}} | b)$  for the background only ( $b$ ) hypothesis. These probabilities are defined as

$$p_\mu = P(q_\mu \geq q_\mu^{\text{obs}} | \mu s + b) = \int_{q_\mu^{\text{obs}}}^{\infty} f(q_\mu | \mu, \hat{\theta}_\mu^{\text{obs}}) dq_\mu, \\ 1 - p_b = P(q_\mu \geq q_\mu^{\text{obs}} | b) = \int_{q_{\mu=0}^{\text{obs}}}^{\infty} f(q_\mu | \mu = 0, \hat{\theta}_{\mu=0}^{\text{obs}}) dq_\mu, \quad (3.11)$$

where  $p_\mu$  and  $p_b$  are the p-values associated to the two hypothesis, and  $f(q_\mu | \mu, \hat{\theta}_\mu^{\text{obs}})$  and  $f(q_\mu | \mu = 0, \hat{\theta}_{\mu=0}^{\text{obs}})$  are the probability density functions of the signal plus background and background only hypothesis constructed from toy Monte Carlo pseudo data. These are generated with nuisance parameters fixed to  $\hat{\theta}_{\mu=0}^{\text{obs}}$  (background only) and  $\hat{\theta}_\mu^{\text{obs}}$  (signal plus background). The 95% CL level upper limit on  $\mu$  is achieved by adjusting  $\mu$  until  $\text{CL} = 0.05$ , this is the so-called observe limit. The expected median upper limit and the  $\pm 1\sigma$  and  $\pm 2\sigma$  bands for a hypothesis is generated by a large set of pseudo data and calculate the CLs and the value of  $\mu$  at 95% CL for each of them. A cumulative probability distribution can be build by starting the integration from the side corresponding to low event yields. The median expected value, so-called expected limit at 95% CL, is where the cumulative distribution function crosses the 50% quantile. The  $\pm 1\sigma$  (68%) and  $\pm 2\sigma$  (95%) bands on the expected limit are defined by the crossings of the 16% and 84%, and 2.5% and 97.5% quantiles.

In order to significantly reduce computing time, the Asymptotic CL method is used. This method avoids an ensemble of toy Monte Carlo samples and instead replaces it by one representative dataset, called Asimov dataset. This dataset is constructed such that all observed quantities are set equal to their MLE values ( $\hat{\theta}_{\text{Asimov}} = \theta_0$ ). More information about this procedure can be found in Refs. [147].



# Event reconstruction and identification

4

943 The simulated data after the detector simulation described in [Section 3.2](#), has the exact same  
944 format as the real collision data recorded at the CMS experiment. Therefore the same software  
945 can be used for the reconstruction of both simulation and real data. In [Section 4.1](#), the object  
946 reconstruction is explained. After reconstructing the objects, they are connected to physics  
947 objects need to be identified ([Section 4.2](#)) and corrected for pileup ([Section 4.3](#)). The objects  
948 used for physics analysis have extra requirements as shown in [Section 4.4](#). A summary of all  
949 the corrections applied to data and simulation is given in [Section 4.5](#).

## 950 4.1 Object Reconstruction

951 In [Figure 4.1](#), the particle interaction in a transverse slice of the CMS detector is shown. When  
952 a particle enters the detector, it first enters the tracker where charged particle trajectories,  
953 so-called tracks, and origins, so-called vertices, are reconstructed from signals or hits in the  
954 sensitive layers. The magnetic field bends the charged particles making it able to measure the  
955 electric charges and momenta of charged particles. The electron and photons are absorbed in  
956 the ECAL and the corresponding electromagnetic showers are detected as clusters of energy  
957 in adjacent cells. From this, the energy and the direction of the particles can be determined.  
958 The charged and neutral hadrons can also initiate a hadronic shower in the ECAL that is fully  
959 absorbed in the HCAL. The clusters from these showers are also used to estimate the energy  
960 and direction. Muons and neutrino's pass through the calorimeters without little to no energy  
961 loss and the neutrinos even escape the CMS detector undetected while muons produce hits in  
962 the muon detectors.

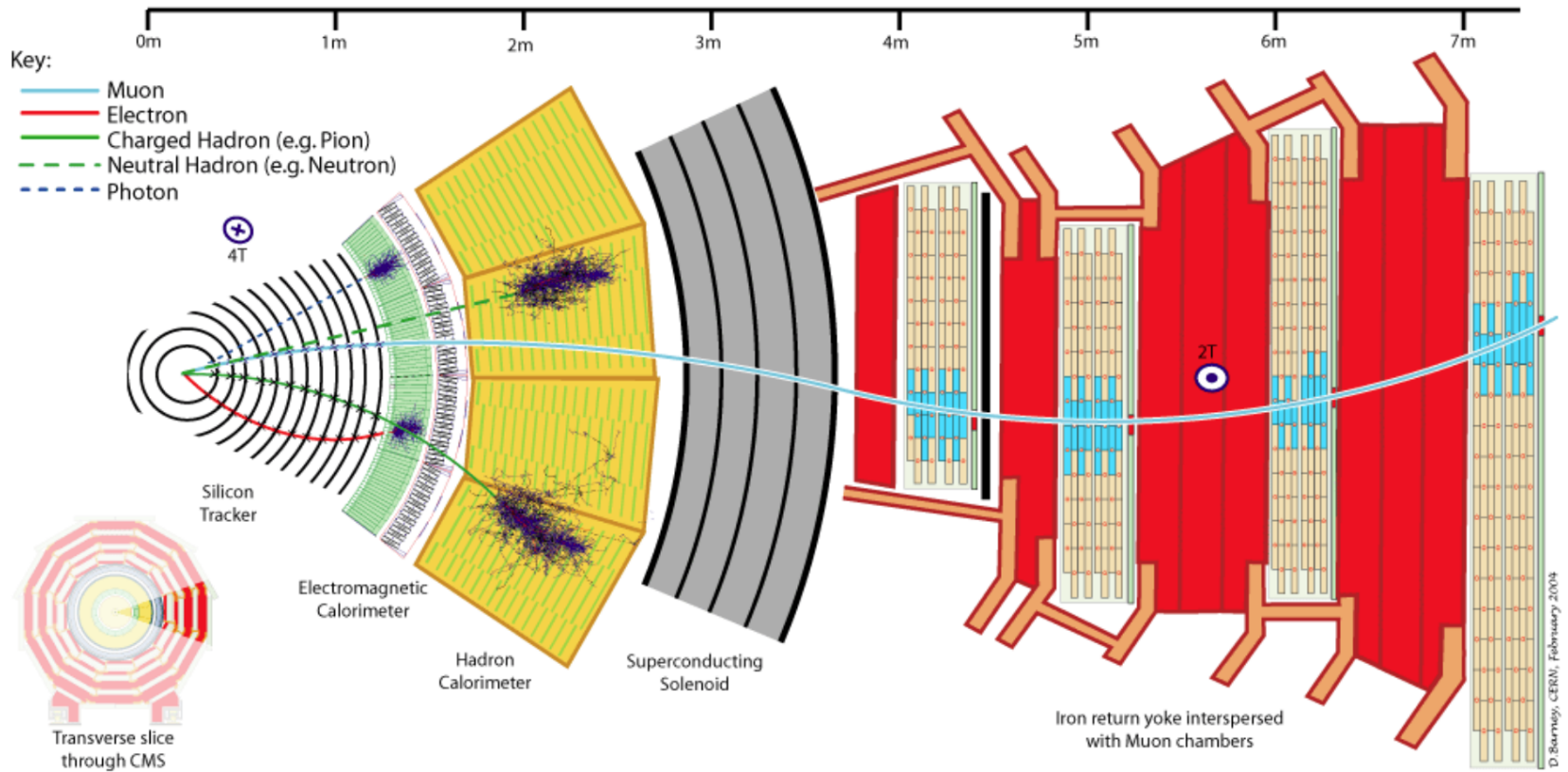


**Figure 4.1:** Cross-section of the CMS detector with all parts of the detector labelled. This sketch shows the specific particle interactions from a beam interaction point to the muon detector. The muon and charged pion are positively charged, the electron is negatively charged. Figure taken from [155].

963 The particle flow (PF) [155] reconstruction algorithm correlates the tracks and clusters  
 964 from all detector layers with the identification of each final state particle, and combines the  
 965 corresponding measurements to reconstruct the properties. The muon is identified by a track  
 966 in the inner tracker connected to a track in the muon detector as described in Section 4.1.2.  
 967 The electrons are identified by a track and an ECAL cluster, not connected to an HCAL cluster  
 968 as described in Section 4.1.3. The ECAL and HCAL clusters without a track link identify the  
 969 photons and neutral hadrons, while the addition of the tracker determines the energy and  
 970 direction of a charged hadron.

### 971 4.1.1 Charged particle tracks

972 An iterative tracking algorithm is responsible for the reconstruction of the tracks made by  
 973 charged particles in the inner tracking system. Each iteration consists of four steps [71]: the  
 974 track-seed generation, the pattern recognition algorithm, removal of track-hit ambiguities and  
 975 a final track fit. The pattern recognitions done by use a Kalman filter method [156, 157] which  
 976 into account the magnetic field and multiple scattering effects. All hits that are unambiguously  
 977 associated to the final track are removed from the list of available hits. In order to associate the  
 978 remaining hits, the procedure is repeated with looser track reconstruction criteria. The use of  
 979 the iterative track reconstruction procedure has a high track finding efficiency, where the fake  
 980 track reconstruction rate is negligible.

**NOTE:** Ik kan hier stoppen en 4.1.1, 4.1.2, 4.1.3.4.1.4 volledig schrappen (dus enkel primary vertex houden)

### 981 4.1.2 Following the Muon's Footsteps

982 The muon reconstruction [158] has three subdivisions: local reconstruction, regional reconstruction  
 983 and global reconstruction. The local reconstruction is performed on individual detector  
 984 elements such as strip and pixel hits in the inner tracking system, and muon hits and/or segments  
 985 in the muon chambers. Independent tracks are reconstructed in the inner tracker - called tracker  
 986 tracks - and in the muon system, called standalone muon tracks. Based on these tracks, two  
 987 reconstructions are considered: Global Muon reconstruction and Tracker Muon reconstruction.  
 988 The first is an outside in approach starting from a standalone muon track while the second uses  
 989 an inside-out approach starting from tracker tracks. For low transverse momenta ( $p_T \lesssim 5$  GeV),  
 990 the tracker muon reconstruction is more efficient than the global muon approach. This is due  
 991 to the fact that tracker muons only require a single muon segment in muon system, while the  
 992 global muon approach requires typically segments in at least two muon stations. These tracker  
 993 muons are used for identifying muons from the hadronisation of b or c quarks. The global muon  
 994 approach typically improves the tracker reconstruction for  $p_T \gtrsim 200$  GeV.

### 995 4.1.3 The path of the Electron

996 Standard tracking algorithms are based on Kalman filtering which assume that the energy loss  
 997 is Gaussian distributed. Since the electron tracks are increasingly curved in the magnetic field  
 998 as a function of its flight distance, these standard tracking algorithms are not suitable to fit the  
 999 electron tracks and different filtering algorithm, the Gaussian sum filter (GSF) [159] is used  
 1000 instead.

1001 In CMS, the electrons are reconstructed in two ways. The older ECAL based tracking is  
 1002 developed to identify high energetic isolated electrons. This tracking algorithm starts from

1003 ECAL clusters with a transverse energy above 4 GeV and extrapolates from these cluster the  
 1004 position of the hits in the tracker. Another, tracker based algorithm uses all the tracks with  
 1005 a  $p_T$  higher than 2 GeV found with iterative tracking as seeds. The electron seeds from the  
 1006 ECAL- and tracker-based procedures are merged into a unique collection and are then refitted  
 1007 by using the summed Gaussian distributions as uncertainty per hit in the track fit. The electron  
 1008 efficiency is measured in 8 TeV proton collision data to be better than 93% for electrons with an  
 1009 ECAL supercluster energy of  $E_T > 20$  GeV [160]. For electrons with an  $E_T > 25$  GeV in 13 TeV  
 1010 proton collision data, the efficiency is about 96%[161].

#### 1011 4.1.4 Primary Vertex Reconstruction

1012 The primary vertex (PV) reconstruction is able to measure the location of all proton interaction  
 1013 vertices in each event consisting of the signal vertex and all vertices from pileup events. First  
 1014 tracks are selected to be consistent with being produced promptly in the primary interaction [81].  
 1015 Then the tracks are grouped according to the  $z$  coordinate of their closest approach to the beam  
 1016 line [162] and a vertex fitting algorithm [163] is performed. The primary vertex is found as the  
 1017 vertex corresponding to the highest sum of squared track transverse momenta and is taken to  
 1018 be the main interaction point. The resolution on the primary vertex is about 14  $\mu\text{m}$  in  $r\phi$  and  
 1019 about 19  $\mu\text{m}$  in the  $z$  direction for primary vertices with the sum of the track  $p_T > 100$  GeV  
 1020 for 2016 data taking.

#### 1021 4.1.5 Calorimeter clusters

1022 The energy and direction of stable neutral particles such as photons and neutral hadron are recon-  
 1023 structed using a cluster algorithm. This algorithm also separates neutral particles from charged  
 1024 hadron energy deposits, and reconstructs and identifies electrons and their bremsstrahlung  
 1025 photons. Furthermore, the cluster algorithm is contributing to the energy measurements of  
 1026 charged hadrons that don't have accurate tracks parameters, e.g. for low quality and high  
 1027 transverse momentum tracks. The clustering is performed separately in each subdetector:  
 1028 ECAL barrel and endcaps, HCAL barrel and endcaps, and the two preshower layers. The HF has  
 1029 no clustering algorithm since the electromagnetic or hadronic components give rise to an HF  
 1030 EM or HF HAD cluster.

1031 The clustering algorithm consist of different steps. First seeds are identified when cells have  
 1032 an energy larger than the seeding threshold and larger than their neighbouring cells. Then  
 1033 topological clusters are made by accumulating cells that share at least a corner with a cell  
 1034 already in the cluster and an energy above a cell threshold set to twice the noise level. The  
 1035 third step is an expectation maximization algorithm that reconstructs the cluster [155] and  
 1036 assumes that the energy deposits are Gaussian distributed. The calorimeter clusters are used  
 1037 for reconstructing photons and neutral hadrons. The clusters that are not in the vicinity of the  
 1038 extrapolated charged tracks identified as neutral hadrons or photons. If the energy deposits are  
 1039 in vicinity of charged tracks, such is the case for charged hadrons, the neutral particle energy  
 1040 deposit is measured as an excess over the charged particle deposit.

## 1041 4.2 Particle flow identification

1042 The several PF elements from the various CMS subdetectors are connected through a link  
 1043 algorithm. This algorithm tests any pair of elements in an event, only considering nearest  
 1044 neighbours in the  $\eta\phi$ -plane. The quality of the link is determined via the distance between the  
 1045 two elements and PF blocks of elements are formed from elements with a direct link or indirect  
 1046 link through common elements. The identification and reconstruction follows a particular order  
 1047 in each PF block. After each identification and reconstruction the corresponding PF elements  
 1048 (tracks and clusters) are removed from the PF block.

1049 The muons are the first to be identified and reconstructed. These are reconstructed if their  
 1050 momenta are compatible with corresponding track only momenta. Then the electron and its  
 1051 corresponding brehmstrahung photons, are identified and reconstructed by using of the GSF  
 1052 tracking. At the same time, the energetic and isolated photons are identified as well. The  
 1053 remaining elements in the PF block are subjected to a cross identification of charged hadrons,  
 1054 neutral hadrons, and photons that arise from parton fragmentation, hadronisation, and decays  
 1055 in jets. The charged hadron candidate is made from the remaining candidates that have a  
 1056 charged particle track associated with them. Then the charged particle energy fraction is  
 1057 subtracted from the calibrated energy of the linked calorimeter clusters and the remaining  
 1058 energy is assigned to the neutral energy. Depending on the excess of neutral energy in the ECAL  
 1059 and HCAL clusters, a photon or a neutral hadron is assigned respectively. The pseudorapidity  
 1060 range of the inner tracker limits the information on the particles charge to  $|\eta| < 2.4$ . Outside  
 1061 this range a simplified identification is done for hadronic and electromagnetic candidates only.

## 1062 4.3 Pileup mitigation and luminosity measurement

For the 8 TeV dataset, an average of about 21 pileup interactions happen per bunch cross section. For the dataset taken at 13 TeV, the number of pileup interactions increases to about 27 interactions per bunch crossing. These interactions are spread around the beam axis around the centre of the CMS coordinate system and follow a normal distribution with a standard deviation of about 5 cm [155]. The number of pileup interactions is estimated from the number of interaction vertices reconstructed from charged particle tracks, or from the instantaneous luminosity of the given bunch crossing with dedicated detectors and the inelastic proton-proton crossing. The luminosity of the CMS interaction point is estimated from measuring certain process rates with luminometers such as the pixel detector, HF calorimeter, and the pixel luminosity telescope [164]. The instantaneous luminosity from recorded process rate  $R$  is then determined as

$$Ldt = \frac{Rdt}{\sigma_{fid}}, \quad (4.1)$$

1063 where  $\sigma_{fid} = \sigma \times A$  corresponds to the fiducial cross section recorded in the luminometer  
 1064 acceptance  $A$  which is determined using van der Meer scans [165]. The overall uncertainty on  
 1065 the luminosity measurement is estimated to be 2.5%.

1066 The luminosity is used to infer to number of pileup interactions in data, which can be used  
 1067 to corrected the predefined pileup interactions in simulation. Then an event weight can be

1068 derived from the ratio of the distributions of pileup interactions in data and simulation. For 13  
 1069 TeV collisions, the inelastic cross section is measured to be  $71.3 \pm 3.5$  mb [166]. However a  
 1070 better agreement in data and simulation for the pileup sensitive variables, such as the number  
 1071 of primary vertices, is found with a lower cross section of 69.2 mb with an uncertainty of 4.6%.

## 1072 4.4 Physics object reconstruction and identification

1073 The particle flow objects are used for building physics objects that are used for analysis. Analyses  
 1074 use jets, muons, electrons, photons, taus and missing transverse momentum  $\vec{p}_T$  with extra,  
 1075 analysis dependent requirements. In the following section, only the physics objects used  
 1076 throughout this thesis are discussed.

### 1077 4.4.1 Muons

1078 The muon candidates used for analysis in this thesis correspond to the tight and loose working  
 1079 point. Detailed reports on the performance can be found in [167].

1080 The tight working point rejects objects wrongly reconstructed as muons from hadron showers  
 1081 that reach the muon system (punch-throughs), by requiring that the global muon fit includes  
 1082 at least one valid hit in the muon chambers for which at least two muon segments in two  
 1083 muon stations are present. Furthermore, the muon tracks should have a global fit yielding a  
 1084 goodness-of-fit of  $\chi^2/\text{ndof} < 10$ . Requiring at least one pixel hit in the muon track suppresses  
 1085 the decay of muons in flight. Also a minimum of five hits in the tracker is required. Cosmic  
 1086 muons and muons originating from pileup interactions are rejected by constricting the distance  
 1087 of the muon with respect to the primary vertex by putting limits on  $d_{x,y} < 2$  mm and  $d_z < 5$   
 1088 mm. Also muons according to the loose muon working point will be used in the thesis. These  
 1089 are either global muons or tracker muons reconstructed from the particle flow muon object. In  
 1090 Table 4.1, the muon requirements for the muons used throughout this thesis are summarised.  
 1091 In Figure 4.2, the muon efficiencies for data and simulation is presented. These efficiencies are  
 1092 estimated from tag-and-probe methods [167]. Overall, the efficiency is about 95-100%, with  
 1093 two drops due to the crack between the wheels of the DT system. The differences between  
 1094 data and simulation are corrected by applying  $p_T$ - and  $\eta$ -dependent scale factors ( $\epsilon_{\text{data}}/\epsilon_{\text{MC}}$ )  
 1095 to simulated events.

In addition to the identification criteria, the muons are required to be spatially isolated from electromagnetic and hadronic activity. The relative lepton isolation is defined as estimating the total transverse energy of the particles emitted around the direction of the lepton by defining a cone of radius  $\Delta R$  in  $\eta\phi$  plane around the lepton direction. Then a summed energy is calculated from the charged hadrons (CH), neutral hadrons (NH), photons ( $\gamma$ ), excluding the lepton itself. This sum is then corrected to remove the energy coming from pileup interactions. The relative isolation for muons  $\mathcal{I}_\mu$  is defined as [155]:

$$\mathcal{I}_\mu = \frac{\sum p_T(\text{CH}) + \max(0., \sum E_T(\text{NH}), \sum E_T(\gamma) - 0.5 \times \sum E_T(\text{CH}))}{p_T(\mu)}, \quad (4.2)$$

1096 where a cone of  $\Delta R = 0.4$  is adopted and the pileup mitigation is based on the  $\Delta\beta$  correction.  
 1097 The  $\Delta\beta$  correction estimates the pileup energy as half of the contribution coming from charged

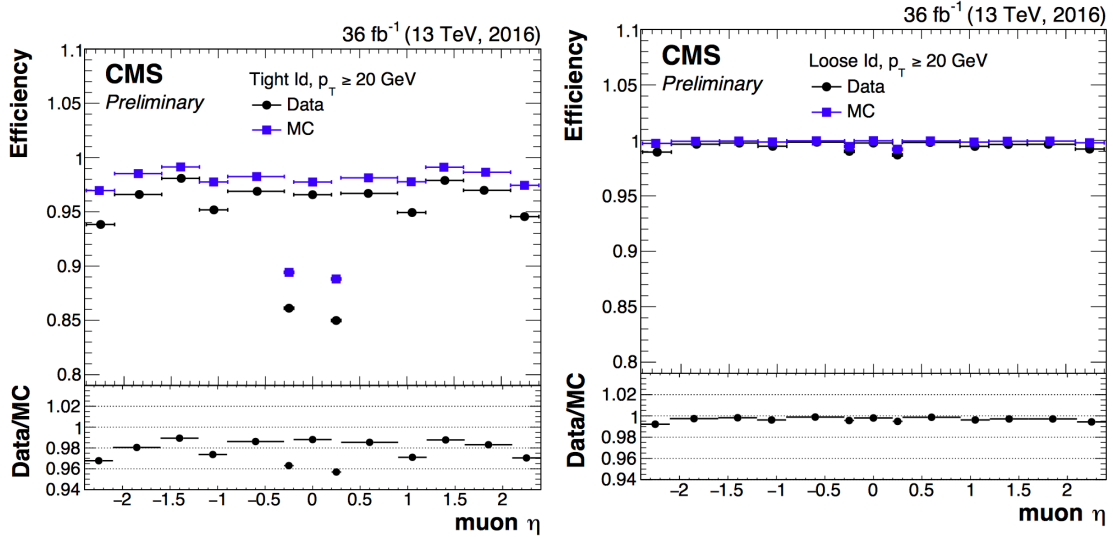


**Figure 4.2:** Comparison of the muon tight ID (left) and loose ID (right) efficiencies in data and simulation as a function of the pseudorapidity of the muon using the full 2016 dataset. Figure taken from [167].

hadrons. For tight ID muons, this relative isolation should  $\mathcal{I}_\mu < 0.15$ , while for loose muons this should be  $\mathcal{I}_\mu < 0.25$ . In Figure 4.3, the isolation efficiencies as a function of the pseudo rapidities using the tag and probe method are shown for the tight muon working point. The efficiencies are 85-100% and have a decline for low- $p_T$  muons. The differences between data and simulation are accounted for by applying  $\eta$ - and  $p_T$ -dependent scale factors on the simulation.

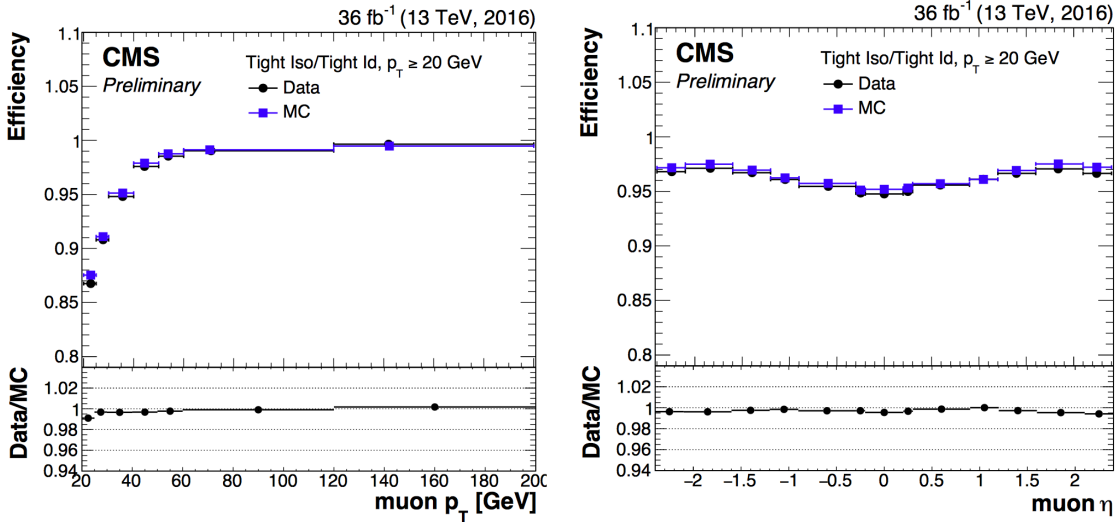


**Figure 4.3:** Comparison of the muon tight isolation requirement with the muon tight ID efficiencies in data and simulation as a function of the transverse momentum (left) or pseudorapidity (right) of the muon using the full 2016 dataset. Figure taken from [167].

**Table 4.1:** Muon requirements for the tight and loose working points, used throughout this thesis.

Property	Loose Muons	Tight Muons
Global muon or Tracker Muon	One or the other	Both
Particle Flow muon	Y	Y
$\chi^2/ndof$ of global muon track fit	N/A	< 10
Nb. of hit muon chambers	N/A	> 0
Nb. of muon stations contained in the segment	N/A	> 1
Size of the transverse impact parameter of the track wrt. to the PV	N/A	$d_{xy} < 2 \text{ mm}$
Longitudinal distance wrt. the PV	N/A	$d_z < 5 \text{ mm}$
Nb. of pixel hits	N/A	> 0
Nb. of tracker layers with hits	N/A	> 5
Relative Isolation	<0.25	<0.15

#### 1103 4.4.2 Electrons

1104 The electrons candidates used correspond to the tight and veto working points. The study of  
 1105 the electron reconstruction and identification performance can be found in [161].

1106 Starting from an electron PF candidate with a GSF track that is outside the barrel-endcap  
 1107 transition region ( $1.4443 < |\eta| < 1.5660$ ), several requirements are set. The electron track  
 1108 should not have more than one (two or three) missing hit in the innermost layer for the tight (veto)  
 1109 working point. This dismisses electrons from photon conversions are dismissed. Additionally, a  
 1110 photon conversion veto is applied by testing if a pair of electron tracks is originating from a  
 1111 common displaced vertex. Furthermore, refined cuts are applied on the shower shape variables  
 1112 such as the difference in  $\eta$  or  $\phi$  between the energy weighted supercluster position in the  
 1113 ECAL and the track direction in at the innermost tracker position ( $\Delta\eta_{\text{in}}$ ,  $\Delta\phi_{\text{in}}$ ), and the ECAL  
 1114 crystal based shower covariance in the  $\eta$  direction ( $\sigma_{\eta\eta}$ ). These cuts also include energy related  
 1115 variables such as the absolute difference between the inverse electron energy measured in the  
 1116 ECAL and the inverse momentum measured in the tracker ( $|1/E - 1/p|$ ), and the ratio of the  
 1117 energy measured in the HCAL and ECAL (H/E). Unlike the muon case, the identification criteria  
 1118 also contain requirements on the isolation of the electrons.

Similar to the muons, the electron relative isolation is determined from the sum of the particles in a cone around the electron itself. The cone radius used for electrons is  $\Delta R = 0.3$  and a  $\rho$  correction for pileup mitigation is applied. For this correction, the expected pileup energy inside the isolation cone is estimated from the median density energy per area of pileup contamination ( $\rho$ ), computed event by event, and the effective area ( $A_{\text{eff.}}$ ) [155]. This effective area is estimated from simulation and denotes the expected amount of neutral energy from

pileup interactions per  $\rho$  within the isolation cone as a function of the pseudo rapidity of the associated ECAL superclusters. Table 4.2 shows the values used for 13 TeV data. The relative electron isolation  $\mathcal{I}_e$  is calculated as

$$\mathcal{I}_e = \frac{\sum p_T(\text{CH}) + \max(0., \sum E_T(\text{NH}), \sum E_T(\gamma) - \rho \times A_{\text{eff}})}{p_T(e)}. \quad (4.3)$$

**Table 4.2:** The effective areas  $A_{\text{eff}}$  used for the electron relative isolation [168].

$\eta$ region	$A_{\text{eff}}$
$0 <  \eta  < 0.1752$	0.1703
$1.0 <  \eta  < 0.1479$	0.1715
$1.479 <  \eta  < 2.0$	0.1213
$2.0 <  \eta  < 2.2$	0.1230
$2.2 <  \eta  < 2.3$	0.1635
$2.3 <  \eta  < 2.4$	0.1937
$2.4 <  \eta  < 2.5$	0.2393

1119

1120 The efficiency of electron identification is estimated from  $Z \rightarrow e^- e^+$  events via the tag-and-  
 1121 probe method and is shown in Figure 4.4 for the tight working point. The efficiencies reach  
 1122 95 – 100%. The difference between data and simulation are corrected by dedicated  $p_T$ - and  $\eta$   
 1123 dependent scale factors as well.

1124 **4.4.3 Jets**

1125 Jets are reconstructed from all reconstructed particles without the charged hadrons associated to  
 1126 pileup vertices. The clustering is done via the anti –  $k_T$  algorithm [169] with a radius parameter  
 1127 for the cone size of the resulting jet of  $R = 0.4$ . More information about the jet algorithm  
 1128 performance can be found in Ref. [170].

1129 The jets used for the analysis discussed in this thesis uses the loose identification working  
 1130 point summarised in Table 4.4. The requirements on the jet constituents are based on the  
 1131 assumption that a proper jet originating from the hadronisation of a quark or gluon consists of  
 1132 multiple PF particles and types. Therefore, the jet should consist of more than one constituent  
 1133 and the neutral hadron fraction and neutral EM energy fractions should be less than 99%. For  
 1134 the jets within the tracker acceptance ( $|\eta| < 2.4$ ), at least one constituent has to be a charged  
 1135 hadron resulting in a charged hadron energy fraction above 0%. Additionally the charged  
 1136 EM energy fraction should be less than 99%. On top of these requirements, objects that are  
 1137 labelled as jets and found in vicinity of any isolated lepton,  $\Delta R < 0.3$ , are removed from the jet  
 1138 collection in that event to avoid duplications of objects.

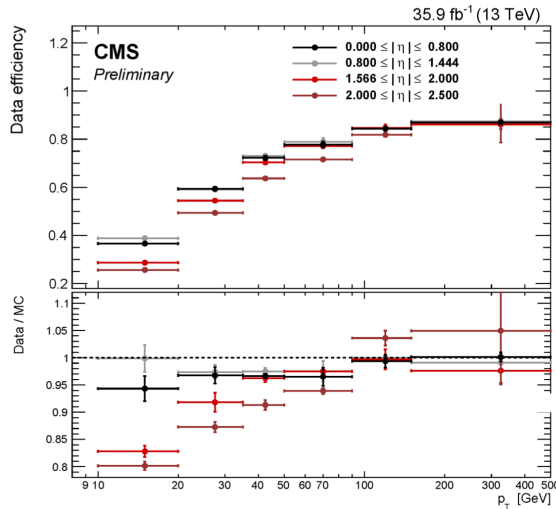


**Figure 4.4:** Electron identification efficiency as function of the electron transverse momentum from the full 2016 dataset. Figure taken from [161].

**Table 4.3:** Electron requirements used in this analysis. The requirements are set in the barrel ( $|\eta_{supercluster}| \leq 1.479$ ) and the endcaps ( $|\eta_{supercluster}| > 1.479$ ).

Properties	$ \eta_{supercluster}  \leq 1.479$		$ \eta_{supercluster}  > 1.479$	
	Veto electron	Tight electron	Veto electron	Tight electron
$\sigma_{\eta\eta}$	< 0.0115	< 0.00998	< 0.037	< 0.0292
$ \Delta\eta_{in} $	< 0.00749	< 0.00308	< 0.00895	< 0.00605
$ \Delta\phi_{in} $	< 0.228	< 0.0816	< 0.213	< 0.0394
H/E	< 0.356	< 0.0414	< 0.211	< 0.0641
relative isolation	< 0.175	< 0.0588	< 0.159	< 0.0571
$ 1/E - 1/p $	$< 0.299 \text{ GeV}^{-1}$	$< 0.0129 \text{ GeV}^{-1}$	$< 0.15 \text{ GeV}^{-1}$	$< 0.0129 \text{ GeV}^{-1}$
expected missing inner hits	$\leq 2$	$\leq 1$	$\leq 3$	$\leq 1$
pass conversion veto	Y	Y	Y	Y

**Table 4.4:** Jet criteria used throughout the thesis. The last three requirements are only for jets within the tracker acceptance.

Properties	Loose Jet ID
Neutral hadron fraction	< 0.99
Neutral EM fraction	< 0.99
Number of constituents	> 1
Charged hadron fraction	> 0
Charged multiplicity	> 0
Charged EM fraction	< 0.99

1139 The energy of the reconstructed jets deviates from the energies of the corresponding jets  
 1140 clustered from the hadronisation products of true partons from simulations due to non linear  
 1141 subdetector response and efficiencies. The jet energy corrections (JEC) calibrate the jets  
 1142 in order to have the correct energy scale and resolution. Jet energy scale corrections (JES)  
 1143 are determined as a function of pseudorapidity and the transverse momentum from data and  
 1144 simulated events by combining several channels and methods. This is extensively described  
 1145 in [171]. These corrections account for the effects of pileup, the uniformity of the detector  
 1146 response, and residual data-simulation jet energy scale differences. Furthermore, the jet energy  
 1147 resolution (JER) is measured in data and simulation as function of pileup, jet size and jet flavour.  
 1148 The performance of the jet energy corrections for the 13 TeV dataset can be found in [172].

1149 The JEC are factorised and subsequently correct for the offset energy due to pileup, the detector  
 1150 response to hadrons, and residual differences between data and simulation as a function of the  
 1151 jet pseudorapidity and transverse momentum. The consecutive steps of JEC are shown in Figure  
 4.5. The off set corrections remove the dependence of the jet energy response of additional pileup

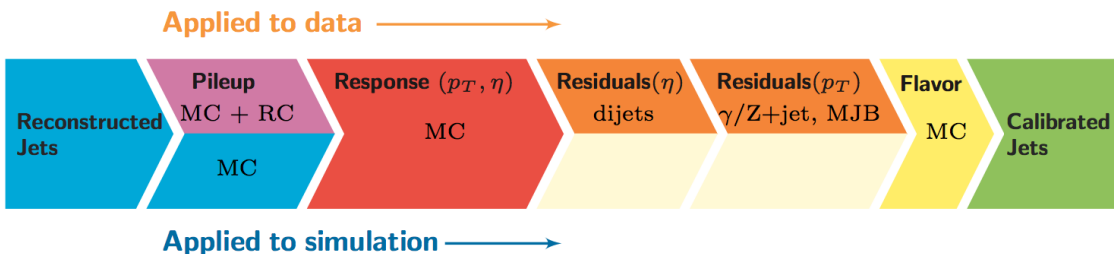


**Figure 4.5:** The sequence of the JEC for data and simulations. The corrections marked with MC are derived from simulation studies, while RC stands for random cone, and MJB for the analysis of multi-jet events. Figure taken from [171].

1152 activity. It is based on the jet area method, which uses the effective area of the jets multiplied  
 1153 by the average density in the event to calculate the offset energy to be subtracted of the  
 1154 jets. The correction factors are derived by comparing the jet response with and without pileup

1156 events overlaid. The residual differences between data and detector simulation are determined  
 1157 using the random cone method (RC). For this method, many jets are reconstructed in each  
 1158 event by clustering particles through placing random cones. This provides a mapping of the  
 1159  $\eta\phi$ -space and the average  $p_T$  of those jets gives the average energy offset due to pileup [171].  
 1160 The next level of corrections have as goal to have an uniform energy response independent  
 1161 of the transverse momentum or pseudorapidity of the jet. These corrections are determined  
 1162 from simulated events by matching the reconstructed to true particle jets and comparing there  
 1163 momenta. The residual corrections between data and simulation are determined by comparing  
 1164 the transverse momentum balance in various types of events (multi-jet, Z + jets, and  $\gamma$  + jets),  
 1165 using a reference jet in the barrel region. The jet flavour corrections are optional and not used  
 1166 for this thesis. More information on the jet flavour corrections can be found in [171]. For jets  
 1167 with a transverse momentum above 30 GeV, the uncertainties from the various corrections are  
 1168 3-5% for the 13 TeV dataset [172].

After applying JEC, the transverse momentum resolution of the jet is extracted from data and simulated events. There are two methods used to rescale the reconstructed four momentum chosen based on whether or not the simulated jet can be matched to a true jet in simulation. The factors are defined as

$$c_{\text{matched}} = 1 + \frac{p_T^{\text{reco.}} - p_T^{\text{true}}}{p_T^{\text{reco.}}} (s_{\text{JER}} - 1), \\ c_{\text{unmatched}} = 1 + N(0, \sigma_{\text{JER}}) \sqrt{\max(s_{\text{JER}}^2 - 1, 0)}, \quad (4.4)$$

1169 where  $N(0, \sigma_{\text{JER}})$  denotes a sample value from a normal distribution centred at zero with  
 1170 as standard deviation the relative resolution in simulation  $\sigma_{\text{JER}}$ , and  $s_{\text{JER}}$  the  $\eta$ -dependent  
 1171 resolution scale factors. These scale factors are derived from data from di-jet or  $\gamma$  + jets events  
 1172 and analysing the  $p_T$  balance. The resolution scale factors (data/simulation) are found to be  
 1173 1.1-1.2 except for the transition regions around  $|\eta| = 3$  and  $|\eta| = 1.4$  [172] and given in Table  
 1174 4.5.

#### 1175 4.4.4 Jets from b fragmentation

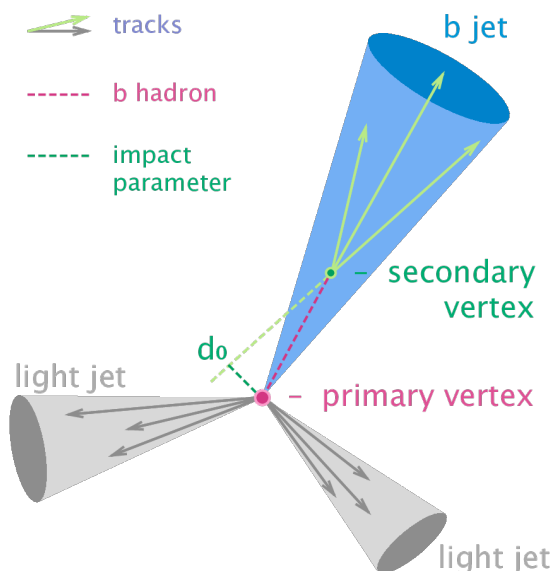
1176 Jets originating from the hadronisation of bottom quarks can be discriminated from jets from  
 1177 gluons and light-flavour quarks as well as charm quark fragmentation through the use of b-  
 1178 tagging. There are several algorithms developed within CMS to perform b-tagging [173, 174]  
 1179 on jets that fall within the pseudorapidity acceptance of the trackers. These algorithms exploit  
 1180 the properties of the b quark to identify the jets formed by its fragmentation. These hadrons  
 1181 have relative large masses, long lifetimes and daughter particles with hard momentum spectra.  
 1182 Additionally, their semi-leptonic decays can be exploited as well. To use b-jet identification  
 1183 in an analysis, one needs to know its efficiency and misidentification probability. In general  
 1184 these are function of the pseudorapidity and transverse momentum of the considered jet. Their  
 1185 performances are directly measured from data by use of b-jet enriched jet samples (multi-jet or  
 1186 top-quark decays).

1187 This thesis uses b-jets identified by the Combined Secondary Vertex version 2 (CSVv2)  
 1188 algorithm [173]. This algorithm combines secondary vertices together with track based lifetime

**Table 4.5:** Jet energy scale factors in bins of  $\eta$  with uncertainty

$ \eta $	SF	Uncertainty ( $\pm$ )
0-0.5	1.109	0.008
0.5-0.8	1.138	0.013
0.8-1.1	1.114	0.013
1.1-1.3	1.123	0.024
1.3-1.7	1.084	0.011
1.7-1.9	1.082	0.035
1.9-2.1	1.140	0.047
2.1-2.3	1.067	0.053
2.3-2.5	1.177	0.041

information by use of a multivariate technique. The secondary vertex is reconstructed from displaced tracks within a jet, as illustrated in [Figure 4.6](#). The final state b quark is encapsulated in a B meson (e.g.  $B^\pm$ ,  $B_0$ ,  $B_S$ ) after the hadronisation. This B meson has relatively long lifetime and can travel a measurable distance from the primary vertex before decaying. After reconstruction, the secondary vertices are required to be in accordance with the B meson hypothesis bases on the amount of shared tracks with the primary vertex, the invariant vertex mass to reject kaon decays, and the direction of the tracks compared to the jet axis.

**Figure 4.6:** Sketch showing the common principle of the identification of b-jets. Figure taken from [175]

1196 The b-tagging algorithm performances are evaluated taking into account two cases: discrim-  
 1197 ination of b-tagged jets originating from charm quarks, and discrimination of b-tagged jets  
 1198 against jets coming from gluons or light (u, d, s) quarks. In Figure 4.7, the misidentification  
 1199 probabilities for different b-tagging algorithms within CMS are shown. Based on the misidentifi-  
 1200 cation probabilities for a certain threshold on the CSVv2 discriminator, different working points  
 1201 are defined. These are shown in Table 4.6. The analysis presented in this thesis uses the loose  
 working point which has an average efficiency of 81% and a misidentification rate of 10%.

**NOTE:** Find reason why I am not using cMVA, omdat CSVv2 op ttbar events is gemeten en cMVA op multijet?

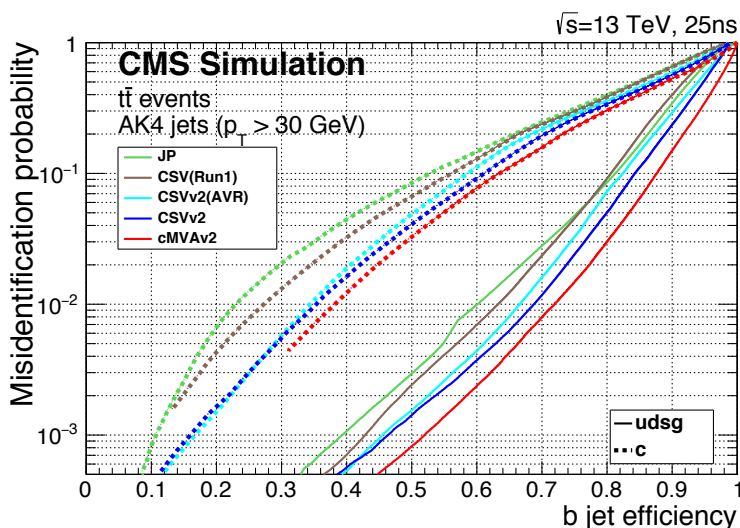


**Figure 4.7:** Misidentification probabilities of various b-tagging algorithm in simulation. Figure taken from [174].

**Table 4.6:** Working points used for tagging jets as coming from b quarks for the CSVv2 discriminant.

WP	CSVv2 discr cut	b-tag eff.	misid. prob.
Loose (L)	> 0.5426	≈ 81%	≈ 10%
Medium (M)	> 0.8484	≈ 66%	≈ 1%
Tight (T)	> 0.9535	≈ 46%	≈ 0.1%

1202

1203 The efficiency of tagging a jet as coming from a bottom quark in simulation typically deviates  
 1204 somewhat from data. Efficiency scale factors  $\epsilon_b^{\text{data}}/\epsilon_b^{\text{MC}}$  are derived from data to account for  
 1205 those differences. These scale factors are  $\eta$ -,  $p_T$ -, and flavour dependent, where the flavour  
 1206 of the jet is determined from matched generated hadrons. For cut based analyses these scale  
 1207 factors are applied to the b-tagging efficiencies and mistag rates according to the chosen working  
 1208 point [174]. For shape based analysis however, such as the one presented in this thesis, the  
 1209 scale factors are applied on the distribution of the b-tagging discriminator. This is the so-called  
 1210 IterativeFit method [176].

1211 The uncertainties related to the IterativeFit method cover possible shape discrepancies between  
 1212 data and simulation. The uncertainty coming from the purity of the sample is subdivided into  
 1213 two uncorrelated uncertainties based on the purity of the light flavoured (lf) and heavy flavoured  
 1214 (hf) jet contributions in the sample. Furthermore, the jet energy scale results in jets migrating  
 1215 from one  $p_T$  bin to an other, having an influence on bin dependent scale factors. The statistical  
 1216 fluctuations of the limited amount of entries in each bin are also accounted for and have an  
 1217 influence on the scale factor uncertainties. These have four uncorrelated sources: two for heavy  
 1218 flavour and two for light flavour jets. Since the uncertainty on the scale factors for the jets  
 1219 originating from a charm quark (cf) is determined from the uncertainty on the b scale factors  
 1220 resulting in two independent uncertainties [176].

#### 1221 4.4.5 Missing transverse energy

The missing transverse momentum  $\vec{p}_T$  and energy  $E_T^{\text{miss}}$  resulting from particles that do not interact with the detector material, are calculated by balancing the vectorial sum of the transverse momenta of all particles:

$$E_T = |\vec{p}_T|, \\ \vec{p}_T = - \sum_{i=1}^{N_{\text{particles}}} \vec{p}_{T,i}. \quad (4.5)$$

1222 The missing transverse energy is influenced by the minimum thresholds in calorimeters, the  
 1223 inefficiencies in the tracker, and the non-linear response of the calorimeter to hadronic particles.  
 1224 The bias is reduced by correcting the transverse momentum of the jets to particle jet  $p_T$  via the  
 1225 JEC and propagating it to the missing transverse momentum. The performance of the missing  
 1226 transverse energy reconstruction can be found in [177].

## 1227 4.5 Summary of corrections

1228 Throughout the chapter several corrections are introduced to improve the agreement between  
 1229 data and simulation. These corrections are sources of systematic uncertainties for the anal-  
 1230 ysis presented in this thesis. Therefore a summary of the corrections and their associated  
 1231 uncertainties is provided.

1232 **Lepton scale factors** The systematic uncertainty on the lepton scale factors consist of three  
 1233 sources: identification, isolation and tracking. The applied scale factors are varied  
 1234 independently within one standard deviation of their measured uncertainties to account  
 1235 for their systematic impact on the measurements.

1236 **Jet energy corrections** The momenta of the reconstructed jets are corrected to match the  
 1237 expected true energy derived from the hadronisation products of partons in simulation.  
 1238 Furthermore, residual corrections and smearing is applied to match the overall energy  
 1239 scale and resolution for simulation and data. These corrections are also propagated to  
 1240 the missing transverse energy. The systematic uncertainties due to these scale factors are  
 1241 estimated by varying them within their uncertainties and repeating the measurements  
 1242 with recalibrated jets and missing transverse energy.

1243 **CSVv2 discriminant shape reweighting** There are three sources of uncertainty contributing  
1244 to the measurement of the scale factors: statistical uncertainties, jet energy scale and  
1245 the purity of the sample. The jet energy scale uncertainty is 100% correlated to the jet  
1246 energy uncertainties and is evaluated simultaneously. The uncertainty coming from the  
1247 purity of the sample is subdivided into two uncorrelated uncertainties based on the purity  
1248 of the light flavoured (lf) and heavy flavoured (hf) jet contributions in the sample. A  
1249 one sigma shift in each of the two purity contributions corresponds to a higher/lower  
1250 contribution in the purity of the considered flavours. The statistical uncertainties has  
1251 four uncorrelated sources, two for heavy flavour and two for light flavour jets. One of  
1252 the uncertainties correspond to the shift consistent with the statistical uncertainties of  
1253 the sample, while the other is propagated in a way that the upper and lower ends of the  
1254 distribution are affected with respect to the centre of the distribution. The uncertainty  
1255 on the charm jet scale factors (cf) is obtained from the uncertainty on the heavy flavour  
1256 scale factors, doubling it in size and constructing two nuisance parameters to control the  
1257 charm flavour scale factors and treating them as independent uncertainties.

1258 **Pileup** Varying the minimum bias cross section, used to calculate the pileup distribution by  
1259  $\pm 4.6\%$ , results in a systematic shift in the pileup distribution. The uncertainty is estimated  
1260 by recalculating the pileup weights to the distributions associated to the minimum bias  
1261 cross sections.

1262 **Luminosity** The luminosity is measured with a global uncertainty of 2.5%, affecting the ex-  
1263 pected number of events.